รายงานวิจัยฉบับสมบูรณ์

โครงการ

ห้องปฏิบัติการระบบของไหลจุลภาคบนชิปที่มีวัสดุนาโนประกอบรวมสำหรับการวิเคราะห์ทางเคมีอย่างรวดเร็ว

อดิสร เตือนตรานนท์ และคณะ

ศูนย์เทคโนโลยีอิเล็กทรอนิกส์และคอมพิวเตอร์แห่งชาติ

กันยายน 2556

สัญญาเลขที่ **RSA5380005**

รายงานวิจัยฉบับสมบูรณ์

โครงการ
ห้องปฏิบัติการระบบของไหลจุลภาคบนชิปที่มีวัสดุนาโน
ประกอบรวมสำหรับการวิเคราะห์ทางเคมีอย่างรวดเร็ว

อดิสร เตือนตรานนท์ และคณะ **ศูนย์เทคโนโลยีอิเล็กทรอนิกส์และคอมพิวเตอร์แห่งชาติ**

สนับสนุนโดยสำนักงานกองทุนสนับสนุนการวิจัย

และศูนย์เทคโนโลยีอิเล็กทรอนิกส์และคอมพิวเตอร์แห่งชาติ สวทช

1) บทคัดย่อ

ห้องปฏิบัติการบนชิป หรือ Lab-on-a-Chip เป็นเทคโนโลยีที่ใช้ในการตรวจวิเคราะห์ทางเคมีที่มีประสิทธิภาพสูง ตรวจวัดได้รวดเร็ว มีความแม่นยำสูง มีความน่าเชื่อถือสูง ขนาดเล็กสามารถพกพาไปออกตรวจนอกสถานที่ได้ โดยอาศัยเทคโนโลยีไมโครอิเล็กทรอนิกส์เพื่อสร้างโครงสร้างขนาดเล็กของท่อขนาดไมโครเมตร (Microchannel) บนแผ่นชิปที่ทำมาจากวัสดุประเภทแก้วหรือพลาสติก เรียกเทคโนโลยีนี้ว่า Microfluidics ทำให้เราสามารถย่อส่วนการตรวจทั้งหมดหรือบางส่วนลงบนแผ่นชิปนี้ ห้องปฏิบัติการบนชิปถูกนำไปใช้ในการตรวจวัดได้หลากหลายงาน เช่น การรวจวัดทางสิ่งแวดล้อม การตรวจวัดสารพิษในอาหาร หรือการตรวจวัดทางการแพทย์ เป็นต้น ปัญหาในปัจจุบันของเทคโนโลยีนี้คือ เนื่องจากการตรวจในปริมาตรของสารเคมีและสิ่งตรวจวัดขนาดน้อยๆ เป็นระดับนาโนลิตรบนชิป ทำให้การตรวจวัดบนชิปนี้จำเป็นต้องมีความไวสูงกว่าปกติ ในงานวิจัยนี้จึงมุ่งเน้นการใช้วัสดุโครงสร้างระดับนาโน ได้แก่ ท่อคาร์บอนนาโน ลวดนาโน และอนุภาคนาโน มาช่วยเพิ่มประสิทธิภาพการตรวจวัดของเซ็นเซอร์บนชิป โดยเฉพาะอย่างยิ่งเซ็นเซอร์ที่ใช้หลักการทางเคมีไฟฟ้าบนชิป โครงสร้างนาโนเหล่านี้จะช่วยเพิ่มพื้นที่ผิวของการเกิดปฏิกิริยา และช่วยให้การแลกเปลี่ยนอิเล็กตรอนระหว่างอิเล็กโตรดและสารดีขึ้น นอกจากนี้ท่อคาร์บอนนาโนยังนำอิเล็กตรอนได้ดีอีกด้วย ที่ผ่านมา มีงานวิจัยที่พยายามใช้วัสดุนาโนเหล่านี้ติดลงบนอิเล็กโตรดของเซ็นเซอร์ทางเคมีไฟฟ้า แต่ยังมีปัญหาการหลุดร่อนเมื่อใช้ไปเป็นระยะเวลาหนึ่ง ดังนั้นเพื่อแก้ปัญหานี้ ในการวิจัยนี้ ทีมวิจัยมุ่งเน้นการสร้างโครงสร้างนาโน เช่น ท่อคาร์บอนนาโนลงบนพื้นผิวอิเล็กโตรดโดยตรง โดยอาศัยการปลูกด้วยเทคนิคไอระเหยทางเคมี (Chemical Vapor Deposition หรือ CVD) โดยตรงลงบนพื้นผิวของอิเล็กโตรด ซึ่งจะทำให้ท่อคาร์บอนนาโนสามารถยึดเกาะติดบนผิวอิเล็กโตรดได้ดีขึ้นมาก โดยเฉพาะอย่างยิ่งผิวอิเล็กโตรดที่ทำจากทองและเงิน นอกจากนี้ทีมวิจัยยังสามารถกำหนดบริเวณพื้นที่ที่ทำการปลูกให้เป็นไปตามที่กำหนดได้ เพื่อเพิ่มพื้นที่ผิวของการเกิดปฏิกิริยาได้รอบท่อที่ตั้งขึ้นเป็นบริเวณคล้ายโดม ด้วยวิธีนี้ทำให้การตรวจวัดทางเคมีไฟฟ้าบนชิปมีความไวสูงขึ้น สามารถวัดสารปริมาณน้อยๆ ได้ดีขึ้น มีอายุการใช้งานยาวนานยิ่งขึ้น และมีความแม่นยำมากขึ้น นอกจากนี้ยังมีการวิจัยเทคนิคใหม่ๆ ในการติดวัสดุโครงสร้างนาโนด้วยเทคนิคการพิมพ์แบบอิงค์เจ็ต (Inkjet Printing) เพื่อความสะดวกและลดต้นทุนในการสร้างชิป และยังมีการวิจัยวัสดุใหม่ๆ ที่ช่วยเพิ่มประสิทธิภาพของการตรวจวัด ได้แก่ วัสดุกรา

ฟีน (Graphene) ซึ่งเป็นวัสดุคาร์บอน 2 มิติ ที่มีพื้นที่ผิวมากกว่าท่อคาร์บอนนาโนถึงสองเท่า และมีการถ่ายเทอิเล็กตรอนที่ดี ซึ่งช่วยเพิ่มประสิทธิภาพการตรวจวัดได้เพิ่มมากขึ้นหลายเท่าตัว

2) Abstract

Lab-on-a-chip (LOC) is a potential tool for chemical processing and analysis, which is essential for environmental monitoring, food safety and biomedical analysis. Lab-on-a-chip for chemical analysis with high performance including fast and sensitive detection, high reliability, long life-time and point-of-care (POC) portability is thus of great interest. Nanostructures such as nanotube, nanowire and nanoparticle have been widely used to enhance the performance of conventional electrochemical detection. Carbon Nanotube (CNT) is one of the potential nanostructures to significantly improve the performance of conventional electrochemical detection. Recently, CNTs composite modified Au electrodes on microfludic chips based on chemical coating and polymerization has been reported. The reports demonstrated fast and sensitive detection capability. However, reliability and life time of such electrodes in microfluidic system is still ongoing problems because the CNTs composite electrode can slowly be removed under continuous flow of analyte and buffer solution. Therefore, direct growth of CNTs on microfluidic chip platform should be the solution to the problem because the direct growth of CNTs can give the strongest adherence of CNTs on Au electrode on glass substrate. To date there have been no reports on patterned and aligned CNTs growth directly on glass substrate for microfluidic chip platform. In addition, higher density of CNTs prepared by direct growth will give superior electrochemical performance. Moreover, aligned and patterned CNTs can be formed to further improve reliability and enhance electrochemical efficiency via hemispherical solute diffusional effect. In this work, nanostructure such as CNTs will be directly integrated within microfluidic lab-on-a-chip. Patterned and aligned CNTs based electrochemical sensors will be integrated on the chip by direct growth of CNTs on glass substrate based on chemical vapor deposition (CVD) process. The successful development of this technology will lead to microfluidic chip for chemical analysis with significant

advancement in terms of sensitivity, detection limit, reliability and life time. Moreover, the patterned and aligned carbon nanotube in microfluidic platform can be an important basis for further development of automated microfluidic chip with micro/nanosensor array for advance applications including multiple analytes detection and electronic tongues.

3) Keyword: Lab-on-a-Chip, Microfluidic, Nanomaterial, Carbon Nanotube, Sensors

4) บทสรุปผู้บริหาร (Executive Summary)

โครงการระบบปฏิบัติการของไหลจุลภาคบนชิปที่มีวัสดุนาโนประกอบรวมสำหรับการวิเคราะห์ทางเคมีอย่างรวดเร็ว ได้ดำเนินการวิจัยเป็นไปตามแผนวิจัยที่วางไว้เป็นอย่างดี และเสร็จสิ้นสมบูรณ์แล้ว ทางคณะวิจัยฯ ประสบความสำเร็จในการปลูกท่อคาร์บอนนาโนให้มีการจัดวาง (pattern) และจัดเรียง (Align) ได้บนขั้วอิเล็กโทรดซึ่งเป็นขั้ว working electrode ในระบบเซ็นเซอร์แบบเคมีไฟฟ้าที่เป็นระบบ 3 ขั้ว ด้วยการใช้พอลิเมอร์ไวแสงและกระบวนการฉายแสง (Photolithography) และการใช้ Anodized Alumina Oxide (AAO) เป็นหน้ากาก (Template) สำหรับการกำหนดบริเวณที่จะเป็น seed layer เพื่อปลูกท่อคาร์บอนนาโนในภายหลังด้วยเทคนิคไอระเหยทางเคมี (Chemical Vapor Deposition) บนขั้วอิเล็กโทรด การใช้ท่อคาร์บอนนาโนในระบบเซ็นเซอร์ทางเคมีไฟฟ้า พบว่า จะช่วยเพิ่มความไวของเซ็นเซอร์ (Sensitivity) และทำให้ limit of detection ต่ำลง นอกจากนี้ยังพบว่าเซ็นเซอร์ที่สร้างขึ้นมีช่วงการทำงานแบบเป็นเส้นตรง (linearity) ซึ่งเป็นคุณสมบัติพึงประสงค์ของเซ็นเซอร์ที่ดี ทางทีมวิจัยฯ ได้นำเทคนิคใหม่ดังกล่าวไปสร้างเป็นเซ็นเซอร์ทางเคมีไฟฟ้าที่ประกอบรวม (integration) เข้ากับระบบของไหลจุลภาค เป็นระบบห้องปฏิบัติการบนชิป (Lab on a Chip) ที่สามารถทำการตรวจวัดทางเคมีไฟฟ้าได้รวดเร็วมากขึ้น (high throughput) และใช้สารเคมีน้อยลง ได้แก่ ชิปสำหรับการตรวจสอบสารเร่งเนื้อแดง (Salbutamol) ด้วยเทคนิคเคมีไฟฟ้า ชิปสำหรับตรวจปริมาณคลอเรสเตอรอลด้วยระบบของไหลจุลภาคบนชิป ชิปสำหรับตรวจวัดไอโอดีนด้วยเซ็นเซอร์ทางเคมีไฟฟ้าขั้วท่อคาร์บอนนาโนที่ใช้ AAO เป็นหน้ากาก ชิปสำหรับตรวจเชื้อ Vibrio cholera O1ด้วยระบบการตรวจวัดด้วยเทคนิคคานกลไฟฟ้า (Microcantilever Sensor) เพื่อตรวจหาเชื้อก่อโรคในอาหาร ชิปสำหรับการตรวจวัดทางเคมีไฟฟ้าแบบหยด (droplet) ด้วยเทคนิค Electro Wetting on Dielectrics (EWOD) นอกจากนี้ยังพัฒนาเครื่องมือสำหรับเพิ่มประสิทธิภาพการ hybridization ของ DNA บนไมโครอาร์เรย์ด้วย Piezoelectric Actuators และทดสอบกับการตรวจหาเชื้อมาลาเรียด้วยไมโครอาร์เรย์ และได้ตีพิมพ์

บทความทบทวน (Review) เกี่ยวกับระบบตรวจวัดที่ใช้หลักการ Quartz Crystal Microbalance Array บนชิปเดี่ยว ที่เรียกว่า Monolithic Quartz Crystal Microbalance ผลงานวิจัยที่ได้ทำทั้งหมดในปีที่ 1 ได้รับผลสำเร็จเป็นอย่างดีจนสามารถส่งมอบผลงานเป็นบทความตีพิมพ์ในวารสารวิชาการระดับนานาชาติ เป็นจำนวนทั้งสิ้น10 บทความ โดยทั้งหมดเป็นบทความที่ตีพิมพ์ในวารสารที่มี Impact Factor สูง (จากมากไปน้อยตั้งแต่ 6.26, 5.362, 5.362, 5.099, 4.31, 3.722, 3.722,3.368, 0.602 ตามลำดับ (หมายเหตุ ISI Impact Factor 2010)

ส่วนในปีที่ 2 ทางทีมวิจัยฯ ได้ศึกษาวิธีการสร้างและปรับปรุงเครื่องมือเพื่อเพิ่มประสิทธิภาพการ Hybridization ของ DNA บนแผ่น Microarray ทางคณะวิจัยฯ ได้ตีพิมพ์บทความในวารสาร Lab Chip ซึ่งเป็นวารสารวิชาการระดับนานาชาติที่มี Impact Factor สูง (Impact factor 2011 =6.306) เกี่ยวกับทำการสร้างอุปกรณ์เพื่อช่วยการทำ DNA hybridization โดยใช้แผ่นเพียโซอิเล็กทริก 3 แผ่นในการสร้าง acoustic streaming แล้วพบว่าได้ประสิทธิภาพดีกว่าทำด้วยวิธีดั้งเดิมนั้น ในการวิจัยนี้เราได้ปรับแต่งระบบการสร้าง acoustic streaming โดยการออกแบบลักษณะการวางแผ่นเพียโซอิเล็กทริกใหม่เพื่อให้ได้ประสิทธิภาพการทำ DNA hybridization ที่ดีขึ้น

นอกจากนี้ทางทีมวิจัยสนใจศึกษาเกี่ยวกับการสร้างเซ็นเซอร์ทางเคมีด้วยเทคนิตการพิมพ์ (Printing Technology) โดยพิมพ์ขั้วนำไฟฟ้าอิเล็กโทรดด้วยหมึกนำไฟฟ้าชนิดใหม่ที่คิดค้นโดยทีมวิจัยฯ ที่ประกอบด้วยวัสดุนาโนที่เรียกว่า กราฟีน (Graphene) ซึ่งเป็นโครงสร้างคาร์บอนอะตอมที่เรียงตัวเป็นแผ่นหนาเพียงหนึ่งชั้นของอะตอมคาร์บอนเท่านั้น วัสดุกราฟีนมีคุณสมบัติทางไฟฟ้าที่ดีเหมาะสำหรับนำมาทำเป็นขั้วไฟฟ้าอิเล็กโทรดในเซ็นเซอร์แบบเคมีไฟฟ้า เนื่องจาก มีการนำไฟฟ้าที่ดีที่สุดเมื่อเทียบกับวัสดุที่มนุษย์ค้นพบและดีกว่าท่อคาร์บอนนาโน และมีการแลกเปลี่ยนอิเล็กตรอนได้อย่างมีประสิทธิภาพ นอกจากนี้กราฟีนยังมีพื้นที่ผิวซึ่งสามารถเกิดปฏิกิริยาทางเคมีไฟฟ้ามากกว่าท่อคาร์บอนนาดนถึง 2 เท่าตัว ดังนั้นทางทีมวิจัยฯ จึงสังเคราะห์กราฟีนด้วยเทคนิคทางเคมีไฟฟ้าและนำมาผสมกับพอลิเมอร์นำไฟฟ้าที่ชื่อว่า poly(3,4-ethylenedioxythiophene) หรือ PEDOT เกิดเป็นสารประกอบคอมพอสิต (Composite) ที่เรียกว่า graphene-poly(3,4 ethylenedioxythiophene):poly(styrene-sulfonate) หรือ GP-PEDOT:PSS ทางทีมวิจัยฯ ได้ทดสอบพิมพ์คอมพอสิตดังกล่าวด้วยวิธีการพิมพ์แบบอิงค์เจ็ต (Inkjet Printing) ลงบนขั้วไฟฟ้าที่เป็นวัสดุคาร์บอนซึ่งพิมพ์ด้วยวิธีการ Screen Printing มาก่อน เกิดเป็นการพิมพ์แบบไฮบริด (Hybrid Printing) และได้ทดสอบกับการตรวจวัดสารเร่งเนื้อแดง (salbutamol) พบว่า

ประสิทธิภาพของเซ็นเซอร์โดยดูจากพีค (Peek) ของการออกซิเดชั่นสูงกว่าขั้วไฟฟ้าคาร์บอนที่ไม่มีกราฟีนพิมพ์ลงไป ถึง 30-150 เท่า และมีช่วงการวัดที่กว้างขึ้นมาก และมี limit of detection (3S/N) ประมาณ 1.25 M และได้ทำการทดสอบการสอดแทรกกับสารอื่นๆ ปรากฏว่าน้อยมาก ดังนั้นเซ็นเซอร์ที่วิจัยได้จึงเหมาะสำหรับการใช้งานเป็นเซ็นเซอร์ทางเคมีที่มีต้นทุนการผลิตที่ถูก สามารถใช้แล้วทิ้งได้ ผลงานนี้ได้รับการตีพิมพ์ในวารสารวิชาการด้านเซ็นเซอร์ Sensors and Actuator B: Chemical ซึ่งมี ISI Impact Factor สูง (ISI Impact factor 2011 =3.898)

นอกจากนี้ทางคณะวิจัยฯ ได้ตีพิมพ์บทความงานวิจัยเรื่อง Facile preparation of graphene–metal phthalocyanine hybrid material by electrolytic exfoliation ในวารสาร J. Mater. Chem ซึ่งเป็นวารสารวิชาการระดับนานาชาติที่มี Impact Factor สูง (Impact factor 2011=5.968) เกี่ยวกับการเตรียม graphene–metal phthalocyanine ด้วยวิธีการลอกชั้นของกราไฟส์ด้วยไฟฟ้าใน TSCuPc ได้กราฟีน1-2 ชั้น ที่ประกอบด้วยโมเลกุลของ phthalocyanine มีการกระจายตัวที่เสถียรใน electrolyte เมื่อนำไปตรวจคุณลักษณะด้วยเครื่อง SEM พบว่ามีความหนา 2-6 มิลลิเมตร ตรวจสอบคุณลักษณะเพิ่มเติมด้วยเครื่อง Raman/FTIR/UV-Vis spectra และ X-ray diffraction พบว่า TSCuPc–graphene สร้างพันธะโดยไม่ใช้โควาเลนต์ (Non-covalent Bonding) แต่มีปฏิกิริยา **ΠΠ-ΠΠ** ระหว่างชั้นของกราฟีน และ phthalocyanine และบ่งบอกว่า กราฟีนที่ผสมอยู่มีคุณภาพสูง

ส่วนในปีที่ 3 ทางคณะวิจัยได้สร้างเซ็นเซอร์ชีวภาพที่ใช้เอนไซม์ (Enzyme-based biosensor) ที่มีความไวสูง โดยการใช้ graphene–poly(3,4-ethylenedioxythiophene):polystyrene sulfonic acid หรือเรียกย่อว่า GP-PEDOT:PSS ไปปรับปรุงอิเล็กโทรดแบบเดิมที่ทำด้วยวัสดุคาร์บอน ที่เรียกว่า screen printed carbon electrode (SPCE) และทดสอบการใช้งานจริงด้วยการวัดน้ำตาลกลูโคส (glucose)

นอกจากนี้ได้วิจัยการเตรียมวัสดุ metal porphyrins และ phthalocyanines ฝังอยู่ในฟิล์มโปร่งแสงแบบ sol-gel (transparent sol–gel films) ด้วยการพิมพ์แบบอิงค์เจ็ตแบบ piezoelectric และตรวจสอบคุณสมบัติและนำไปใช้งานเพื่อเป็นเซ็นเซอร์เพื่อตรวจวัดก๊าซ (Gas sensor)

และล่าสุดเป็นครั้งแรกที่มีการศึกษาความเป็นพิษต่อเซลล์ (cytoxicity) โดยใช้เซลล์มะเร็งเต้านมชนิด MDA-MB-231 ซึ่งเป็น MDA cells ที่เลี้ยงบนฟิล์มที่เป็นวัสดุคาร์บอนเพส (carbon

paste และฟิล์มที่เป็นวัสดุผสมของกราฟีนและคาร์บอนเพส (graphene - carbon paste) ซึ่งเตรียมโดยการผสมผงกราฟีนที่สังเคราะห์ได้ลงในหมึกคาร์บอนในปริมาณที่แตกต่างกันและขึ้นรูปเป็นฟิลืมด้วยการพิมพ์แบบอิงค์เจ็ต ความเป็นพิษถูกประเมินจากการอยู่รอดของเซลล์ (cell viability), การยึดเกาะของเซลล์ (cell adhesion), ปริมาณอ็อกซิเจน reactive oxygen species (ROS) ที่เซลล์ผลิตขึ้น และการย้อมสีเซลล์ด้วยสารเรืองแสง (fluorescence staining) สรุปได้ว่าการที่ฟิล์มมีกราฟีนผสมอยู่เล็กน้อยจะช่วยลดการเป็นพิษต่อเซลล์ และเพิ่มความเข้ากันได้ทางชีวภาพ

ผลงานทั้งหมดได้รับการตีพิมพ์ในวารสารวิชาการระดับนานาชาติที่มี Impact factor สูง ทั้งสิ้น 13 บทความ และยังมีผลงานเป็น Book Editor 1 เล่มและ Book chapter ทั้งสิ้น 3 บท

5) วัตถุประสงค์ของโครงการ

1. เพื่อพัฒนาเทคนิคใหม่ในการจัดวาง (pattern) และจัดเรียง (align) ท่อคาร์บอนนาโน (carbon nanotube) ลงบนเซ็นเซอร์แบบเคมีไฟฟ้าในอยู่ในระบบปฏิบัติการของไหลจุลภาค (Microfluidics)
2. ศึกษาวิธีการต่างๆ เพื่อใช้ประกอบรวม (integration) ท่อคาร์บอนนาโนที่จัดวางและจัดเรียงแล้วลงในระบบห้องปฏิบัติการบนชิป รวมถึงการประกอบรวมโดยตรง (direct integration)
3. ศึกษาผลของพารามิเตอร์ในกระบวนการสร้างท่อคาร์บอนนาโนที่ประกอบรวมในระบบห้องปฏิบัติการบนชิปและผลต่อการทำงานของเซ็นเซอร์ทางเคมีไฟฟ้า
4. พัฒนาระบบห้องปฏิบัติการบนชิปดังกล่าวเพื่อการตรวจวัดทางเคมีไฟฟ้าอย่างรวดเร็ว ตัวอย่างเช่น การตรวจวัดกรด Ascorbic การตรวจวัดสารเร่งเนื้อแดง (salbutamol) เป็นต้น
5. พัฒนาวิธีการใหม่ๆ ที่สามารถติดหรือเคลือบวัสดุโครงสร้างนาโนลงบนผิวอิเล็กโตรด

6. วิจัยเพื่อหาวัสดุนาโนแบบใหม่ เพื่อเพิ่มประสิทธิภาพของเซ็นเซอร์แบบเคมีไฟฟ้าบนชิป

6) กิจกรรมที่ทำได้จริงและผลงานวิจัยที่ได้รับ

ได้ออกแบบและสร้างห้องปฏิบัติการบนชิป (Lab-on-a-chip) ด้วยเทคโนโลยีระบบของไหลจุลภาค (Microfluidics) โดยใช้วัสดุนาโน ได้แก่ ท่อคาร์บอนนาโน (Carbon Nanotube) เป็นวัสดุประกอบบนอิเล็กโตรด (Electrode) ของระบบตรวจวัดแบบเคมีไฟฟ้า (Electrochemical detection) และทำการทดสอบชิปที่สร้างขึ้น และวิเคราะห์ผล นอกจากนี้ยังพัฒนาวิธีการใหม่ๆ ที่สามารถติดหรือเคลือบวัสดุโครงสร้างนาโนลงบนผิวอิเล็กโตรดด้วยเทคนิคการพิมพ์แบบอิงค์เจ็ต และวิจัยเพื่อหาวัสดุนาโนแบบใหม่ เพื่อเพิ่มประสิทธิภาพของเซ็นเซอร์แบบเคมีไฟฟ้าบนชิป โดยสรุปสามารถอธิบายผลงานของทั้งโครงการได้ดังนี้

6.1 เซ็นเซอร์ทางเคมีไฟฟ้าสำหรับตรวจวัดปริมาณสารเร่งเนื้อแดง (Salbutamol) ด้วยขั้วไฟฟ้าอิเล็กโทรดที่สร้างจากท่อคาร์บอนนาโนที่เรียงตัวและตั้งตรง (Vertically aligned carbon nanotube)

ทางทีมวิจัยฯ ได้สังเคราะห์ท่อคาร์บอนให้ตั้งตรงและเรียงตัวกันอย่างเป็นระเบียบบนขั้วไฟฟ้าที่ทำจากทองคำด้วยเทคนิคการเคลือบแบบไอระเหย (Chemical Vapor Deposition) โดยนำมาใช้เป็นขั้ว working Electrode ในเซลไฟฟ้าเคมี (Electrochemical Cell) ทำให้สามารถวัดความเข้มข้นของสารเร่งเนื้อแดงได้ตั้งแต่ 10-7 ถึง 10-4 mol/l และมีค่าความเป็นเส้นตรง โดยมีค่าความไวสูงถึง 0.13 ไมโครแอมป์/M/l สามารถทำงานได้ดีตั้งแต่ช่วง 0.5-100 ไมโครโมลาร์ ผลงานนี้ได้รับการตีพิมพ์ในวารสารวิชาการ Sensor Letters ดังรายละเอียดในเอกสารแนบ

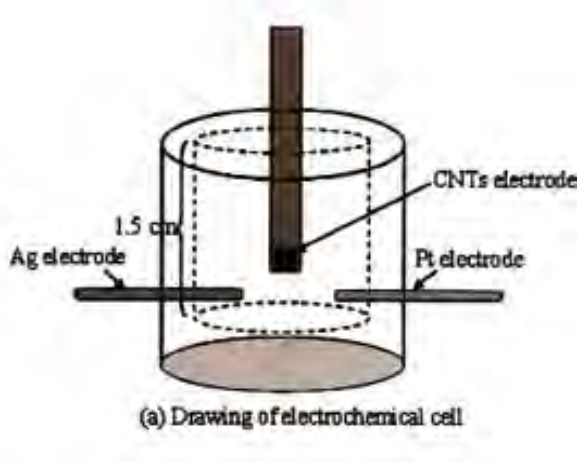

ภาพแสดงเซลเคมีไฟฟ้าสำหรับตรวจวัดปริมาณสารเร่งเนื้อแดง (Salbutamol) ด้วยขั้วไฟฟ้าอิเล็กโทรดที่สร้างจากท่อคาร์บอนนาโนที่เรียงตัวและตั้งตรง

6.2 ชิปสำหรับตรวจเชื้อ Vibrio cholera O1ด้วยระบบการตรวจวัดด้วยเทคนิคคานกลไฟฟ้า (Microcantilever Sensor) เพื่อตรวจหาเชื้อก่อโรคในอาหาร

ทางคณะวิจัยได้ทำการสร้างชิปสำหรับตรวจหาเชื้อก่อโรคในอาหาร โดยมุ่งทดสอบกับเชื้อ Vibrio cholera O1 ซึ่งเป็นเชื้อก่อโรคอหิวาตกโรค โดยใช้เทคนิคการตรวจวัดด้วยคานกลไฟฟ้า (Microcantilever Sensor) โดยที่คานกลขนาด 250 x 50 ไมโครเมตรถูกสร้างด้วยเทคโนโลยีระบบเครื่องกลไฟฟ้าจุลภาค (Microelectromechanical Systemหรือ MEMS)เซ็นเซอร์ที่สร้างขึ้นสามารถตรวจวัดเชื้อ Vibrio cholera O1ได้โดยมีความไว (Sensitivity) ระหว่าง 1,000 ถึง 1,000,000 CFU/ml โดยที่ limit of detection อยู่ที่ 1,000 CFU/ml และความไวต่อมวล (mass sensitivity) อยู่ที่ 146.5 pg/Hz ผลงานนี้ได้รับการตีพิมพ์ในวารสาร Biosensor and Bioelectronics ซึ่งมี Impact Factor สูง (ISI Impact factor 2010 =5.361)

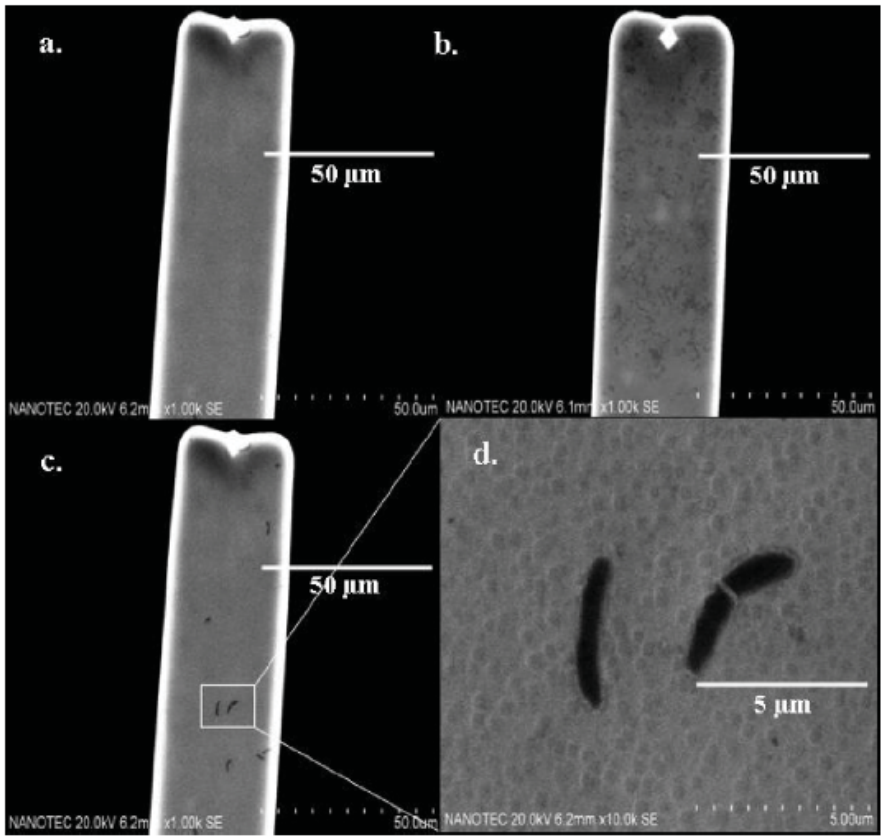

ภาพแสดงคานกลไฟฟ้า(Microcantilever Sensor) สำหรับตรวจเชื้อ Vibrio cholera O1 เพื่อตรวจหาเชื้อก่อโรคในอาหาร

6.3 ชิปสำหรับตรวจปริมาณคลอเรสเตอรอลด้วยระบบของไหลจุลภาคบนชิป

ทางคณะวิจัยฯ ได้ทำการสร้างระบบตรวจวัดทางเคมีไฟฟ้าประกอบรวมบนชิปห้องปฏิบัติการของไหลจุลภาค โดยมีท่อคาร์บอนนาโนถูกปลูกโดยตรงลงบนขั้วอิเล็กโทรดหนึ่งของเซ็นเซอร์เคมีไฟฟ้า ท่อคาร์บอนนาโนที่ได้มีการจัดเรียงตัวแบบตั้งตรงและตั้งฉากกับพื้นผิวของขั้วไฟฟ้า หลังจากนั้นผิวของท่อคาร์บอนนาโนจึงถูกปรับปรุงด้วยเอนไซม์ Cholesteroloxidaseให้สามารถจับกับคลอเรสเตอรอลในสารตัวอย่าง การใช้ท่อคาร์บอนนนาโนช่วยเพิ่มพื้นที่ผิวของการเกิดปฏิกิริยาทางเคมี และเพิ่มอัตราการแลกเปลี่ยนอิเล็กตรอน นอกจากนี้การใช้ห้องปฏิบัติการบนชิปทำให้สามารถเพิ่มความเร็วในการตรวจวัด (60 ตัวอย่างต่อชั่วโมง) และลดปริมาณสารตัวอย่าง (15 ไมโครลิตรต่อตัวอย่าง) ชิปดังกล่าวสามารถให้ผลการวัดที่เป็น linear range ระหว่าง 50-400 ml/dl

ซึ่งเป็นช่วงปริมาณคลอเรสเตอรอลในเลือดมนุษย์ และมีการรบกวนจากสาร glucose, ascorbicacid, acetaminophenanduricacid น้อยมาก

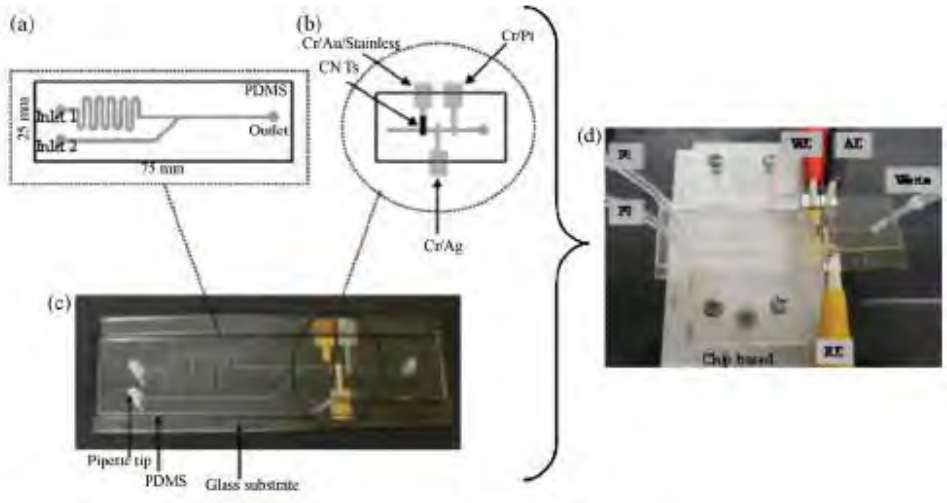

ภาพแสดงชิปสำหรับตรวจปริมาณคลอเรสเตอรอลด้วยระบบของไหลจุลภาคบนชิป

6.4 ระบบสำหรับเพิ่มประสิทธิภาพการ hybridization ของ DNA บนไมโครอาร์เรย์ด้วย Piezoelectric Actuators

ทางคณะวิจัยฯ ได้ทำการสร้างเครื่องมือสำหรับการเพิ่มประสิทธิภาพการHybridization ของ DNA บน Microarray โดยใช้หลักการสร้างคลื่นเสียง (Acoustic Stream) ด้วย Piezoelectric Actuator จำนวน 2 ตัว ทำงานสลับกันเพื่อเขย่าสารตัวอย่างบน microarray ให้แพร่กระจายอย่างสม่ำเสมออย่างรวดเร็วบน microarray ด้วยหลักการดังกล่าว ทดสอบกับการตรวจจับเชื้อมาลาเรีย Plasmodium falciparum พบว่าสามารถลดเวลาการทำงานจาก 16 ชั่วโมงลงเหลือเพียง 4 ชั่วโมงเท่านั้น นอกจากนี้เมื่อเปรียบเทียบเมื่อเวลาเท่ากัน พบว่าเครื่องมือดังกล่าวสามารถเพิ่มประสิทธิภาพจากการจับคู่ของ DNA โดยดูจากความเข้มของสัญญาณ Fluorescence จากเดิม 24-33% ผลงานดังกล่าวได้รับการตีพิมพ์ในวารสาร Lab on a Chip (หรือ Lab Chip) ซึ่งเป็นวารสารวิชาการด้านเทคโนโลยี Lab-on-a-chip อันดับหนึ่ง ซึ่งมี Impact Factor สูงถึง 6.309 (Impact factor 2011 =6.306)

ภาพแสดงระบบสำหรับเพิ่มประสิทธิภาพการ hybridization ของ DNA บนไมโครอาร์เรย์ด้วย Piezoelectric Actuators

6.5 ได้ตีพิมพ์บทความ Review เกี่ยวกับระบบตรวจวัดที่ใช้หลักการ Quartz Crystal Microbalance Array บนชิปเดี่ยว

ทางคณะวิจัยฯ ได้ตีพิมพ์บทความในวารสาร Analytica Chimica Acta ซึ่งเป็นวารสารวิชาการระดับนานาชาติที่มี Impact Factor สูง (IF 2010 = 4.310) เกี่ยวกับเทคนิคในการตรวจวัดความถี่ของแผ่น Quartz Crystal Microbalance (QCM) ที่เปลี่ยนไปตามการเปลี่ยนแปลงของมวลที่เปลี่ยนไปจากการจับระหว่างตัวตรวจวัดและตัวอย่าง บทความนี้ได้ทบทวนเกี่ยวกับการออกแบบการจำลองด้วยคอมพิวเตอร์ และคุณสมบัติของอาร์เรย์ของ QCM ที่สร้างบนชิปเดี่ยว (Monolithic QCMหรือ MQCM) และเน้นเรื่องของการรบกวนและแทรกสอดของสัญญาณเมื่อมีโครงสร้างเป็นอาร์เรย์ การพัฒนา MQCM array จะมีประโยชน์อย่างมากในการประดิษฐ์เซ็นเซอร์ต่างๆ ไม่ว่า ก๊าซเซ็นเซอร์ เซ็นเซอร์ทางชีวภาพ รวมถึงจมูกอิเล็กทรอนิกส์ (Electronic Nose) และลิ้นอิเล็กทรอนิกส์ (Electronic Tongue)

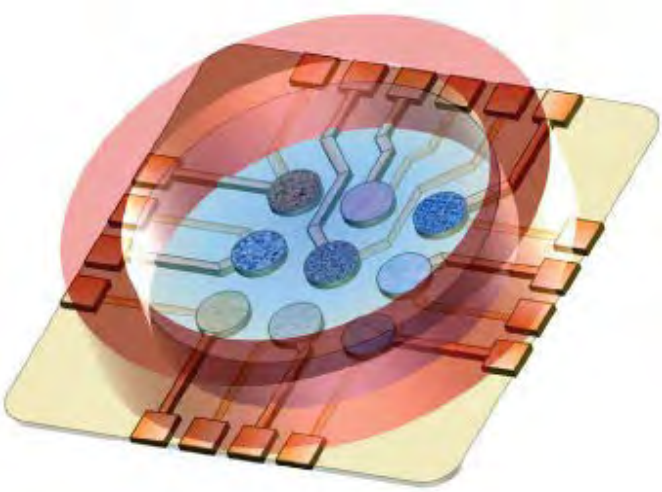

ภาพแสดง concept ของ Quartz Crystal Microbalance Array บนชิปเดี่ยว

6.6 ชิปสำหรับการตรวจวัดทางเคมีไฟฟ้าแบบหยด (droplet) ด้วยเทคนิค Electro Wetting on Dielectrics (EWOD)

ระบบตรวจวัดทางเคมีไฟฟ้าแบบ 3 อิเล็กโทรดถูกสร้างขึ้นบนชิปแก้ว ที่ประกอบด้วยขั้วไฟฟ้าที่เป็นวัสดุเงิน สร้างโดยเทคนิค Sputtering (ขนาด 1000 ไมโครเมตร x 1000 ไมโครเมตร) โดยมีช่องว่างระหว่างขั้ว 50 ไมโครเมตร เรียงตัวเป็นรูปตัว T เพื่อใช้สำหรับการขับเคลื่อนสารละลาย Buffer และ สารตัวอย่าง แบบเป็นหยดเม็ด (droplet) ให้เคลื่อนมาผสมกัน ก่อนเคลื่อนไปทำการตรวจวัดทางเคมีไฟฟ้า ความต่างศักย์ถูกใส่ไปในขั้วไฟฟ้าที่อยู่ถัดกันเพื่อสร้างสนามไฟฟ้าไปรบกวนแรงตึงผิวของหยดน้ำ ทำให้หยดน้ำเคลื่อนกลิ้งไปด้านข้าง เรียกหลักการดังกล่าวว่า Electro Wetting on Dielectric (EWOD) เนื่องจากบนขั้วไฟฟ้าจะเคลือบด้วยสารไดอิเล็กทริก เพื่อทำหน้าที่เป็นชนวนไฟฟ้า ซึ่งจะมีข้อดีคือ ทำให้ได้ระบบของไหลจุลภาค (Microfluidics) ที่ใช้สารเคมีและตัวอย่างน้อยลงกว่าเดิมมาก เพราะสารตรวจวัดเป็นหยดขนาดนาโนลิตร ถึง พิโคลิตร ชิป EWOD ดังกล่าวถูกออกแบบเพื่อทำการทดสอบไอโอดีน โดยสามารถบังคับให้หยดของ Tris buffer และสารละลายไอโอดีนมาทำการผสมกันด้วยอัตราส่วนต่างกันและบังคับหยดสารละลายไปยังขั้วไฟฟ้าเคมีที่ทำด้วยเส้นลวดเพื่อทำการวัดด้วยหลักการ Cyclic Voltamogram ได้ผลเป็นที่น่าพอใจ

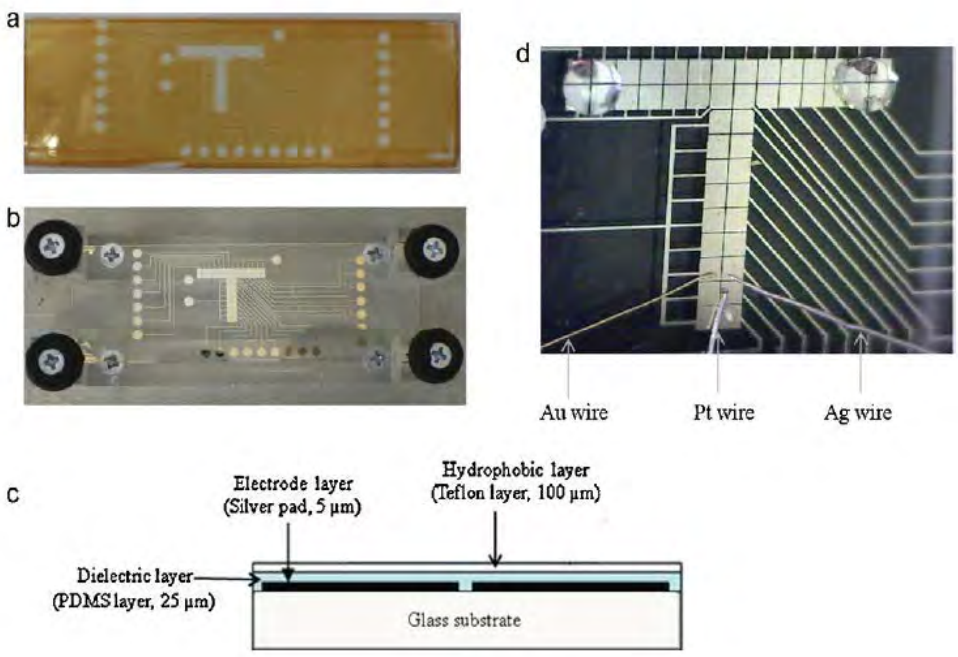

ภาพแสดงชิปสำหรับการตรวจวัดทางเคมีไฟฟ้าแบบหยด (droplet) ด้วยเทคนิค Electro Wetting on Dielectrics (EWOD)

6.7 ชิปสำหรับตรวจวัดไอโอดีนด้วยเซ็นเซอร์ทางเคมีไฟฟ้าขั้วท่อคาร์บอนนาโนที่ใช้ AAO เป็นหน้ากาก

คณะวิจัยฯ ได้ทำการสร้างอาร์เรย์ขนาดนาโนเมตรของท่อคาร์บอนนาโนลงบนอิเล็กโทรดของเซ็นเซอร์ทางเคมีไฟฟ้าที่ประกอบรวมอยู่บนระบบห้องปฏิบัติการบนชิป (Lab-on-a-chip) ด้วยการใช้ Anodized Alumina Oxide ซึ่งมีเป็นโครงสร้างรูขนาดนาโน (nano pore) เรียงตัวแบบเป็นระเบียบทำหน้าที่เป็นหน้ากากสำหรับการเคลือบชั้นของ Seed layer เพื่อการปลูกท่อคาร์บานนาโนในขั้นตอนภายหลัง โดยที่ชั้น aluminum ถูกเคลือบบนอิเล็กโทรดเงินด้วยเทคนิค Sputtering และทำการ Anodization แบบสองขั้นตอนเพื่อทำให้เกิดรูพรุนที่ทะลุจากชั้นบนจนถึงด้านล่าง เกิดเป็นรูพรุนที่เป็นระเบียบบนอิเล็กโทรดโดยตรง จึงทำให้สามารถเป็น template ท่อคาร์บอนนาโนถูกปลูกบนอิเล็กโทรดโดยตรงด้วยเทคนิคไอระเหยทางเคมี เซ็นเซอร์ทางเคมีไฟฟ้าถูกสร้างโดยมีขั้วอิเล็กโทรดหนึ่งเป็นอาร์เรย์ขนาดนาโนของท่อคาร์บอนนาโนดังกล่าว ระบบตรวจวัดทางเคมีไฟฟ้าประกอบรวมในระบบห้องปฏิบัติการบนชิปและเป็นระบบของไหลจุลภาค สามารถใช้ทดสอบกับการวัดไอโอดีน

ด้วยหลักการ Amperometry ปรากฏว่า นาโนอาร์เรย์ของท่อคาร์บอนนาโนช่วยเพิ่ม Sensitivity และขยาย Dynamic Range เมื่อเทียบกับที่ไม่ได้เป็นนาโนอาร์เรย์ชิปสำหรับการตรวจสอบสารเร่งเนื้อแดง ด้วยเทคนิคทางเคมีไฟฟ้าที่ใช้ท่อคาร์บอนนาโนแบบตั้งตรงทางคณะวิจัยฯ ได้สร้างชิปสำหรับการตรวจวัดสารเร่งเนื้อแดง (Salbutamol) โดยใช้เทคนิคการตรวจวัดทางเคมีไฟฟ้า (Electrochemical Sensing) โดยที่ขั้วไฟฟ้าอิเล็กโทรดแบบ 3 ขั้วประกอบด้วยขั้ว Reference ทำจากลวด Ag ขั้ว Auxiliary ทำจากวัสดุลวด Platinum และขั้ว Working ทำด้วยกระบวนการปลูกท่อคาร์บอนนาโนแบบตั้งตรงและตั้งฉากกับพื้นผิวอิเล็กโทรดเงิน เรียกว่า Vertical CNT เซ็นเซอร์ที่ได้มีประสิทธิภาพความไวในการตรวจวัดสาร Salbutamol ระหว่าง 10^{-4} ถึง 10^{-7} mol/l มี linear response และมีความไว (Sensitivity) เท่ากับ 0.13 ไมโครโอห์มต่อโมลต่อลิตร

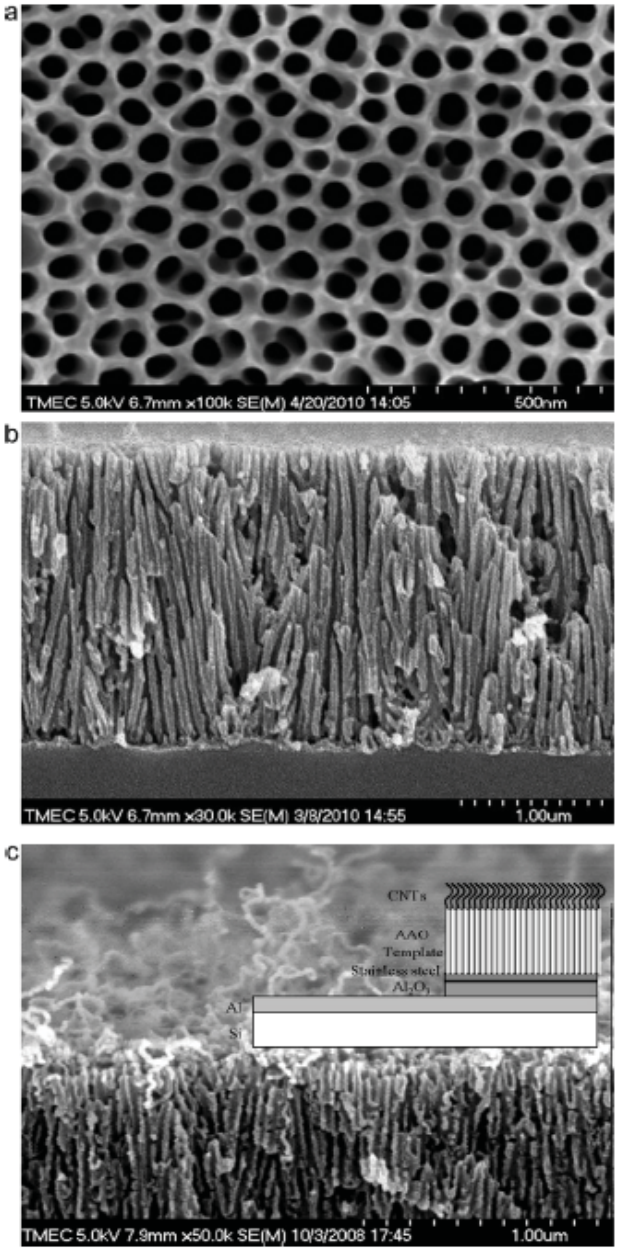

ภาพแสดง Anodized Alumina Oxide ซึ่งมีเป็นโครงสร้างรูขนาดนาโน (nano pore) เรียงตัวแบบเป็นระเบียบทำหน้าที่เป็นหน้ากากสำหรับการเคลือบชั้นของ Seed layer และท่อคาร์บอนนาโนที่ปลูกได้บนขั้วไฟฟ้าอิเล็กโทรด

6.8 งานวิจัยเกี่ยวกับการสร้างเซนเซอร์ทางเคมีด้วยเทคนิคการพิมพ์ (Printing Technology) โดยพิมพ์ขั้วนำไฟฟ้าอิเล็กโทรดด้วยหมึกนำไฟฟ้าชนิดใหม่ที่คิดค้น

โดยทีมวิจัยฯ ที่ประกอบด้วยวัสดุนาโนที่เรียกว่า กราฟีน (Graphene) ซึ่งเป็นโครงสร้างคาร์บอนอะตอมที่เรียงตัวเป็นแผ่นหนาเพียงหนึ่งชั้นของอะตอมคาร์บอนเท่านั้น วัสดุกราฟีนมีคุณสมบัติทางไฟฟ้าที่ดีเหมาะสำหรับนำมาทำเป็นขั้วไฟฟ้าอิเล็กโทรดในเซนเซอร์แบบเคมีไฟฟ้า เนื่องจาก มีการนำไฟฟ้าที่ดีที่สุดเมื่อเทียบกับวัสดุที่มนุษย์ค้นพบและดีกว่าท่อคาร์บอนนาโน และมีการแลกเปลี่ยนอิเล็กครอนได้อย่างมีประสิทธิภาพ นอกจากนี้กราฟีนยังมีพื้นที่ผิวซึ่งสามารถเกิดปฏิกิริยาทางเคมีไฟฟ้ามากกว่าท่อคาร์บอนนาดนถึง 2 เท่าตัว ดังนั้นทางทีมวิจัยฯ จึงสังเคราะห์กราฟีนด้วยเทคนิคทางเคมีไฟฟ้าและนำมาผสมกับพอลิเมอร์นำไฟฟ้าที่ชื่อว่า poly(3,4-ethylenedioxythiophene) หรือ PEDOT เกิดเป็นสารประกอบคอมพอสิตgraphene-poly(3,4-ethylenedioxythiophene):poly(styrene-sulfonate) หรือ GP-PEDOT:PSS ทางทีมวิจัยฯ ได้ทดสอบพิมพ์คอมพอสิตดังกล่าวด้วยวิธีการพิมพ์แบบอิงค์เจ็ต (Inkjet Printing) ลงบนขั้วไฟฟ้าที่เป็นวัสดุคาร์บอนซึ่งพิมพ์ด้วยวิธีการ Screen Printing มาก่อน เกิดเป็นการพิมพ์แบบไฮบริด (Hybrid Printing) และได้ทดสอบกับการตรวจวัดสารเร่งเนื้อแดง (salbutamol) พบว่าประสิทธิภาพของเซนเซอร์โดยดูจากพีคของการออกซิเดชั่นสูงกว่าขั้วไฟฟ้าคาร์บอนที่ไม่มีกราฟีนพิมพ์ลงไป ถึง 30-150 เท่า และมีช่วงการวัดที่กว้างขึ้นมาก และมี detection limit (3S/N) ประมาณ 1.25 M และได้ทำการทดสอบการสอดแทรกกับสารอื่นๆ ปรากฏว่าน้อยมาก ดังนั้นเซนเซอร์ที่วิจัยได้จึงเหมาะสำหรับการใช้ง่รเป็นเซนเซอร์ทางเคมีที่มีต้นทุนการผลิตที่ถูก สามารถใช้แล้วทิ้งได้ ผลงานนี้ได้รับการตีพิมพ์ในวารสารวิชาการด้านเซนเซอร์ Sensors and Actuator B: Chemical ซึ่งมี ISI Impact Factor สูง (ISI Impact factor 2011 =3.898)

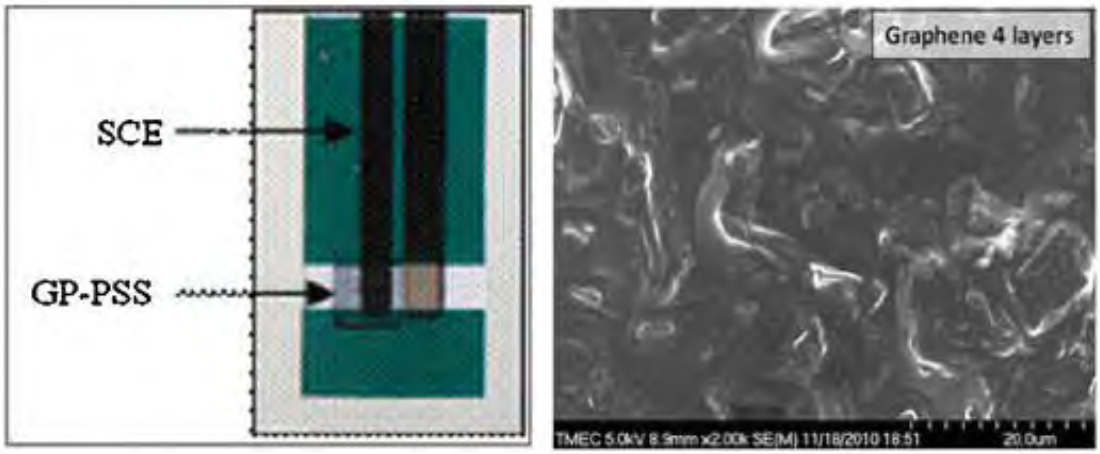

ภาพแสดงเซนเซอร์ทางเคมีด้วยเทคนิคการพิมพ์แบบไฮบริด (Hybrid Printing Technology) โดยพิมพ์ขั้วนำไฟฟ้าอิเล็กโทรดด้วยหมึกนำไฟฟ้ากราฟีน

6.9 การสร้างอุปกรณ์เพื่อช่วยการทำ DNA hybridization โดยใช้แผ่นเพียโซอิเล็กทริก 3 แผ่น

ทางคณะวิจัยฯ ได้ตีพิมพ์บทความในวารสาร Lab Chip ซึ่งเป็นวารสารวิชาการระดับนานาชาติที่มี Impact Factor สูง (Impact factor 2011 =6.306) เกี่ยวกับทำการสร้างอุปกรณ์เพื่อช่วยการทำ DNA hybridization โดยใช้แผ่นเพียโซอิเล็กทริก 3 แผ่นในการสร้าง acoustic streaming แล้วพบว่าได้ประสิทธิภาพดีกว่าทำด้วยวิธีดั้งเดิมนั้น ในการวิจัยนี้เราได้ปรับแต่งระบบการสร้าง acoustic streaming โดยการออกแบบลักษณะการวางแผ่ นเพียโซอิเล็กทริกใหม่เพื่อให้ได้ประสิทธิภาพการทำ DNA hybridization ที่ดีขึ้น โดยการออกแบบระบบนั้นได้ใช้โปรแกรม Comsol® Multiphysics ในการออกแบบและคำนวณสนามของความเร็วที่เกิดจากการสั่นของแผ่นเพียโซอิเล็กทริก โดยพบว่าเวกเตอร์ความเร็วจะมีทิศเป็นเกลียวหมุนวนไปตามสนามของการไหลและทิศทางโดยเฉลี่ยจะมีทิศออกจากจุดกึ่งกลางของของแผ่นเพียโซอิเล็กทริก ลักษณะการหมุนวนของเวกเตอร์ความเร็วแบบนี้เมื่อพิจารณาระบบที่มีแผ่น เพียโซอิเล็กทริก 2 แผ่น จะทำให้ได้ความเข้มของการเรืองแสงจากการ hybridization มีค่าน้อย ในขณะที่ในระบบ 3 แผ่น เพียโซอิเล็กทริกไม่พบปัญหานี้ ลักษณะสัญญาณที่เหมาะสมที่ให้กับแผ่น เพียโซอิเล็กทริกจะหาโดยใช้การทดลองกับเคลื่อนที่ของเม็ดสีเมื่อให้สัญญาณแก่แผ่นเพียโซอิเล็กทริก โดยจากการทดลองพบว่าการให้สัญญาณระหว่างแผ่นกลางและแผ่นริมทั้งสอง 1 วินาที และหยุด 3 วินาทีสลับกัน จะได้ผลดีที่สุด จากนั้นได้ทดสอบการทำ DNA

hybridization กับmicroarray ของเชื้อมาลาเรีย Plasmodium falciparum พบว่าได้ค่าการเรืองแสงเพิ่มขึ้นเป็น 3 เท่า ของค่าที่ได้จากวิธีดั้งเดิม นอกจากนี้ยังพบว่าจำนวนจุดที่เรืองแสงที่ได้จากอุปกรณ์ช่วยทำ DNA hybridization มีจำนวนมากขึ้น ซึ่งจะช่วยเพิ่มประสิทธิภาพในการวิเคราะห์ผล DNA hybridization ให้ดีขึ้น

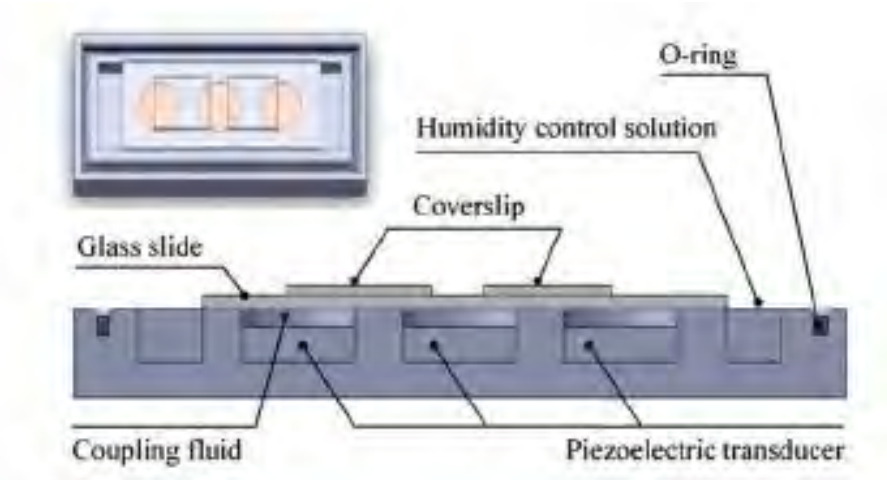

ภาพแสดงอุปกรณ์เพื่อช่วยการทำ DNA hybridization โดยใช้แผ่นเพียโซอิเล็กทริก 3 แผ่น

6.10 งานวิจัยเรื่องการเตรียมวัสดุไฮบริด graphene–metal phthalocyanine อย่างง่าย ด้วยเทคนิค electrolytic exfoliation

ทางคณะวิจัยฯ ได้ตีพิมพ์บทความดังกล่าวในวารสาร J. Mater. Chem ซึ่งเป็นวารสารวิชาการระดับนานาชาติที่มี Impact Factor สูง (Impact factor 2011=5.968) เกี่ยวกับการเตรียม graphene–metal phthalocyanine ด้วยวิธีการลอกชั้นของกราไฟส์ด้วยไฟฟ้าใน TSCuPc ได้กราฟีน 1-2 ชั้น ที่ประกอบด้วยโมเลกุลของ phthalocyanine มีการกระจายตัวที่เสถียรใน electrolyte เมื่อนำไปตรวจคุณลักษณะด้วยเครื่อง SEM พบว่ามีความหนา 2-6 มิลลิเมตร ตรวจสอบคุณลักษณะเพิ่มเติมด้วยเครื่อง Raman/FTIR/UV-Vis spectra และ X-ray diffraction พบว่า TSCuPc–graphene สร้างพันธะโดยไม่ใช้โควาเลนต์ (Non-covalent Bonding) แต่มีปฏิกิริยา **Π-Π** ระหว่างชั้นของกราฟีน และ phthalocyanine และบ่งบอกว่า กราฟีนที่ผสมอยู่มีคุณภาพสูง

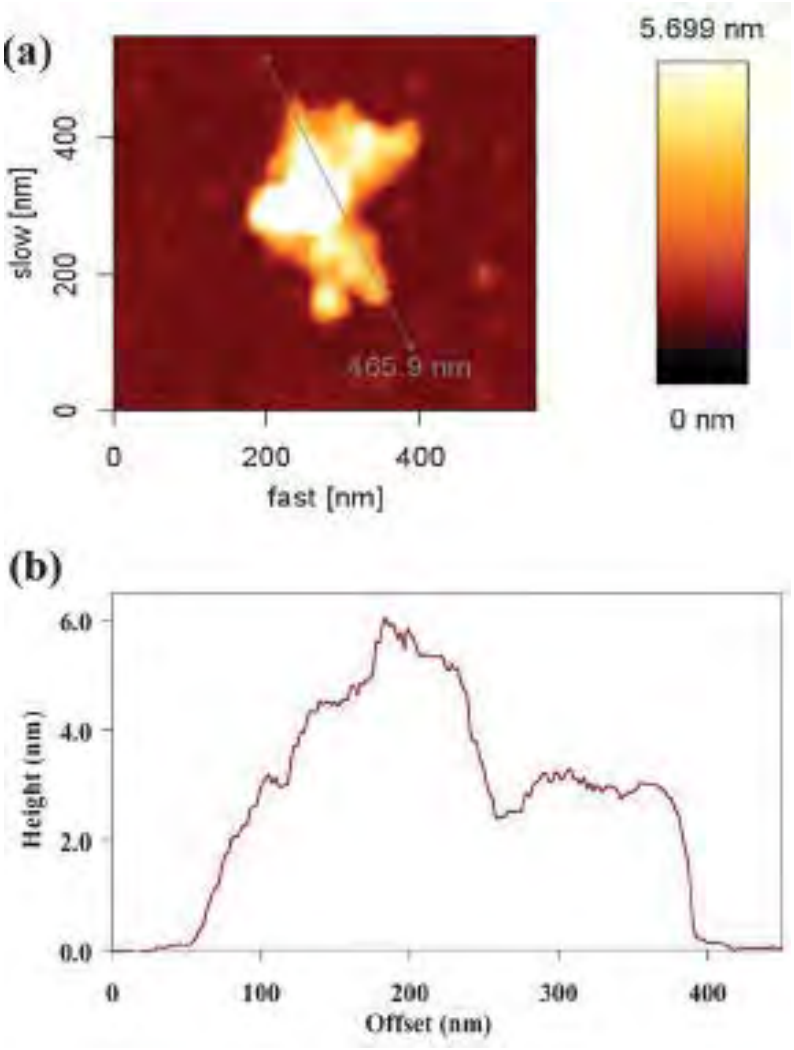

ภาพแสดง graphene–metal phthalocyanine hybrid material และภาพการวัดด้วย Atomic Force Microscopy

6.11 งานวิจัยเรื่อง Graphene–PEDOT:PSS on screen printed carbon electrode for enzymatic biosensing

ในงานวิจัยนี้ ทางคณะวิจัย ประสบความสำเร็จในการสร้างเซ็นเซอร์ชีวภาพที่ใช้เอนไซม์ (Enzyme-based biosensor) ที่มีความไวสูง โดยการใช้ graphene–poly(3,4-ethylenedioxythiophene):polystyrene sulfonic acid หรือเรียกย่อว่า GP-PEDOT:PSS ไปปรับปรุงอิเล็กโทรดแบบเดิมที่ทำด้วยวัสดุคาร์บอน ที่เรียกว่า screen printed carbon electrode (SPCE) และทดสอบการใช้งานจริงด้วยการวัดน้ำตาลกลูโคส (glucose)

วัสดุผสมนาโนหรือนาโนคอมพอสิต GP-PEDOT:PSS สังเคราะห์ด้วยกระบวนการลอกด้วยเทคนิคเคมีไฟฟ้าแบบขั้นตอนเดียว (one-step electrolytic exfoliation) แล้วหยดลงบนขั้วไฟฟ้าแบบคาร์บอนที่สร้างด้วยเทคนิคการพิมพ์แบบสกรีน หรือ SPCE หลักจากนั้น จึงตรึงเอ็นไซม์ glucose oxidase (GOD) บนผิวขั้วไฟฟ้าที่มีวัสดุคอมพอสิต GP-PEDOT:PSS เคลือบอยู่ด้วยหลักการ glutaraldehyde cross linking ขั้วไฟฟ้าที่เตรียมได้ถูกนำไปตรวจสอบด้วย Electron microscope พบว่า บนผิวของขั้วไฟฟ้าปรากฏชั้นของกราฟีนแบบหลายชั้น (multi-layer graphene sheets) และโครงสร้างแบบแถบระดับไมโครเมตร (microstripe structure) ของเอ็นไซม์ GOD บนผิวของขั้วไฟฟ้าอิเล็กโทรดที่สร้างขึ้นได้ เซ็นเซอร์ที่สร้างขึ้นถูกทดสอบโดยหลักการ Direct electrochemistry ของ GOD บนผิวอิเล็กโทรด GP/PEDOT:PSS โดยใช้ cyclic voltammetry ปรากฏว่า กราฟีนมีส่วนสำคัญในกระบวนการ quasi-reversible redox process ขั้วไฟฟ้าอิเล็กโทรด GOD/GP-PEDOT:PSS สามารถตรวจวัดด้วยความไวสูงถึง 7.23 microAmp/mM ซึ่งมีค่าเป็น 13 เท่าเมื่อเทียบกับขั้วไฟฟ้า GOD/PEDOT:PSS ที่ไม่มีกราฟีน แต่มีช่วงการวัดที่ค่อนข้างแคบ (linear dynamic range) เท่ากับ 20–900 micro molar แต่ขั้วไฟฟ้าอิเล็กโทรดแบบ GOD/GP-PEDOT:PSS สามารถเพิ่มประสิทธิภาพการตรวจวัดโดยให้ค่าต่ำที่สุดที่ตรวจวัดได้ หรือ detection limits (3S/N) เท่ากับ 0.3 microM ซึ่งดีกว่าหรือเทียบเท่ากับงานวิจัยทางด้านเซ็นเซอร์ชีวภาพเพื่อตรวจวัดน้ำตาลกลูโคสที่เคยมีรายงานมา นอกจากนี้ทางคณะวิจัยยังทำการวัดอายุการใช้งานของเซ็นเซอร์ที่สร้างขึ้น ปรากฏว่าเซ็นเซอร์สามารถใช้งานได้ยาวนาน โดยมีความเสถียรที่ดี โดยปฏิกิริยาของเอนไซม์ลดลงเพียงร้อยละ 30 เมื่อเวลาผ่านไป 30 วัน

งานวิจัยนี้ได้รับการตีพิมพ์ในวารสาร Journal of Electroanalytical Chemistry ในรายละเอียดดังนี้ A. Wisitsoraat, S. Pakapongpan, C. Sriprachuabwong, D. Phokharatkul, P. Sritongkham, T. Lomas, A. Tuantranont, “Graphene–PEDOT:PSS on screen printed carbon electrode for enzymatic biosensing”, Journal of Electroanalytical Chemistry, Vol .70 ,2013, p.208–213, (ISI Impact factor 2012 = 2.672)

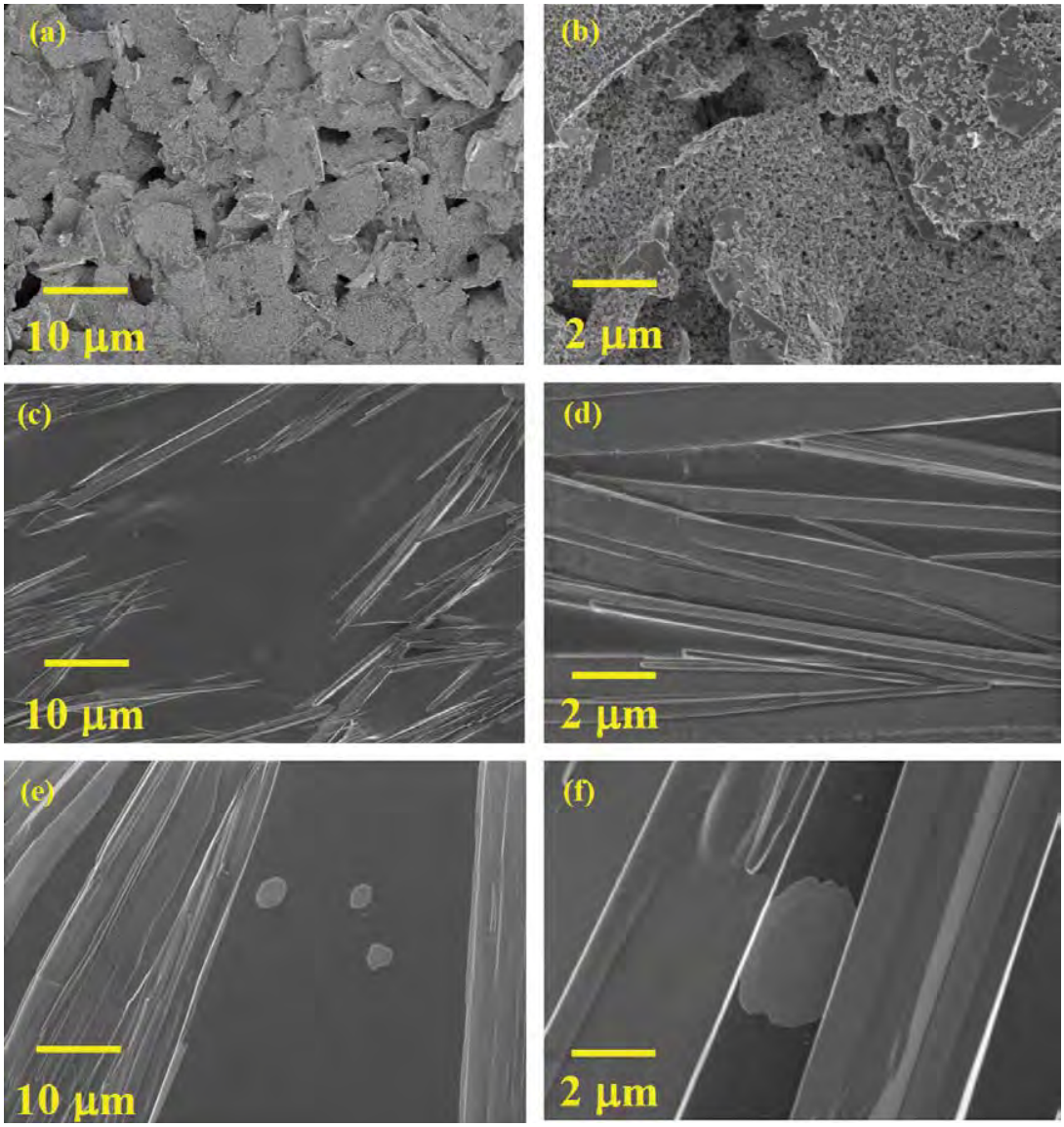

รูปแสดงสภาพพื้นผิวอิเล็กโตรดที่ถ่ายโดยกล้อง Electron Microscope

รูป a และ b เป็นผิว SPCE รูป c และ d เป็นผิว GOD/PEDOT:PSS ที่ไม่มีกราฟีน

รูป e และ f เป็นผิว GOD/GP-PEDOT:PSS ที่มีกราฟีน

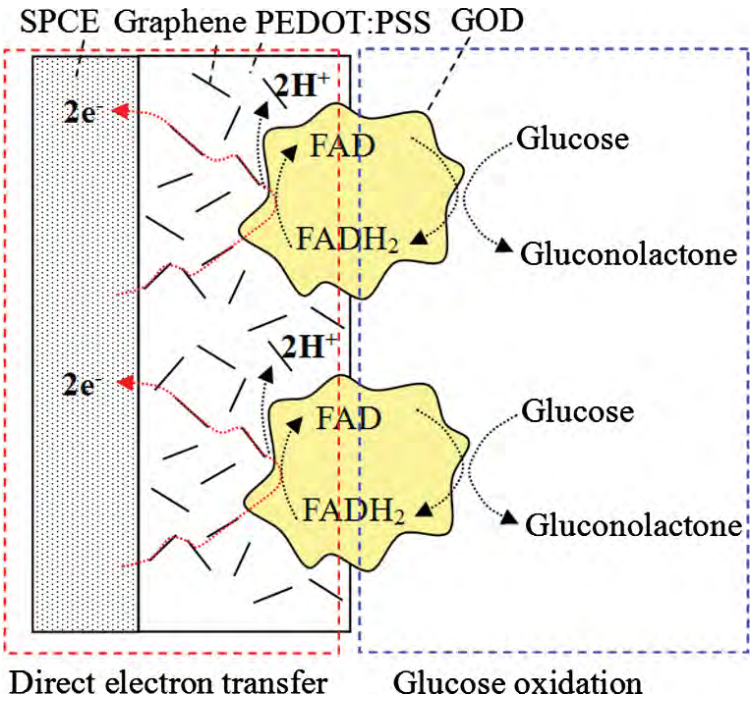

รูปแสดงกลไก Direct Electron Transfer ระหว่าง GOD และ SPCE โดยมี กราฟีน และคอมพอสิต (GOD/GP-PEDOT:PSS)

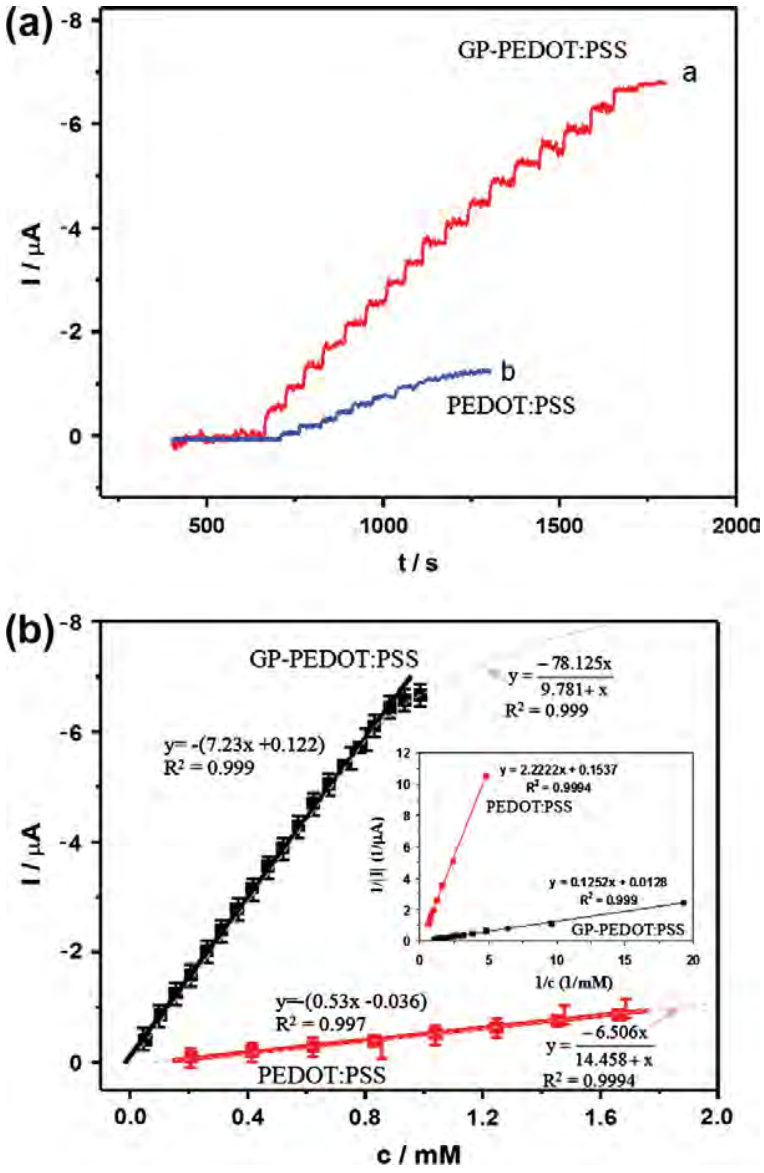

รูปแสดง Calibration Curve ของเซ็นเซอร์ที่สร้างขึ้นเทียบระหว่างขั้วไฟฟ้าแบบมีและไม่มีกราฟีน

6.12 งานวิจัยเรื่องการเตรียมฟิล์ม sol-gel ของ metal phthalocyanines/porphyrins ด้วยวิธีการพิมพ์แบบอิงค์เจ็ต (Inkjet-printed sol–gel films containing metal phthalocyanines/porphyrins for opto-electronic nose applications)

ในงานวิจัยนี้ ทางคณะวิจัยได้วิจัยการเตรียมวัสดุ metal porphyrins และ phthalocyanines ฝังอยู่ในฟิล์มโปร่งแสงแบบ sol-gel (transparent sol–gel films) ด้วยการพิมพ์แบบอิงค์เจ็ตแบบ piezoelectric และตรวจสอบคุณสมบัติและนำไปใช้งานเพื่อเป็นเซ็นเซอร์เพื่อตรวจวัดก๊าซ (Gas sensor)

สารที่สังเคราะห์ขึ้นประกอบด้วย magnesium/manganese(III) chloride/zinc 5,10,15,20-tetraphenyl-21H,23H-porphyrin, magnesium 2,3,7,8,12,13,17,18-octaethyl-21H,23H-porphine, และ zinc 2,9,16,23-tetratertbutyl-29H,31Hphthalocyanine. Porphyrin/Phthalocyanine และถูกผสมด้วยสารละลาย sol–gel เพื่อทำเป็นหมึก ซึ่งจะถูกพิมพ์ลงบนแผ่นแก้วซึ่งทำหน้าที่แผ่นฐานรอง (Substrate) ฟิล์มที่ได้จากการพิมพ์ทำหน้าที่เป็นชั้นตรวจวัด (sensing layers) เพื่อแยกแยะสารไอระเหย (volatile organic compounds หรือ VOCs) ฟิลืมที่ได้จากการพิมพ์ถูกตรวจสอบคุณสมบัติด้วยเทคนิค UV/vis spectroscopy, FTIR spectroscopy, และ scanning electron microscopy จากผลการทดลองพบว่า สารประกอบที่พิมพ์เป็นฟิล์มสามารถงานเป็นก๊าซเซ็นเซอร์ ที่ใช้หลักการเชิงแสง (optical gas sensors) เนื่องจากฟิล์มที่สร้างขึ้นมีการเปลี่ยนช่วงความยาวคลื่นของแสง (spectral alterations) เมื่อฟิล์มสัมผัสกับก๊าซ รวมถึงไอระเหย (VOCs) การเปลี่ยนสีถูกวัดด้วยเทคนิค UV/vis spectroscopy และสามารถใช้เพื่อแยกแยะสารไอระเหยได้สำเร็จ ตัวอย่างเช่นสามารถแยกแยะไอระเหยของ methanol, ethanol, acetone และ isopropanol ข้อมูลถูกวิเคราะห์ด้วยเทคนิค principal component analysis (PCA) และ cluster analysis (CA) ผลปรากฏว่าเราสามารถแยกแยะผลการวัดเป็นลักษณะกลุ่มหรือ isolated clusters ในกราฟที่แสดงแบบ 2 แกนและ 3 แกน ผลการวัดที่ดีที่สุดได้จากฟิล์มที่ประกอบด้วย ZnTPP และ MgTPP ซึ่งถูกโด๊ปด้วย Mn(III)ClTPP

ผลงานวิจัยเรื่องนี้ได้รับการตีพิมพ์ในวารสาร Sensors and Actuators B ที่มี ISI Impact factor 2012 =3.535 โดยมีรายละเอียดดังนี้ Johannes Ph. Mensing, Anurat Wisitsoraat, Adisorn Tuantranont, Teerakiat Kerdcharoen, “Inkjet-printed sol–gel films containing metal phthalocyanines/porphyrins for opto-electronic nose applications” Sensors and Actuators B Vol.176 ,2013, p.428– 436

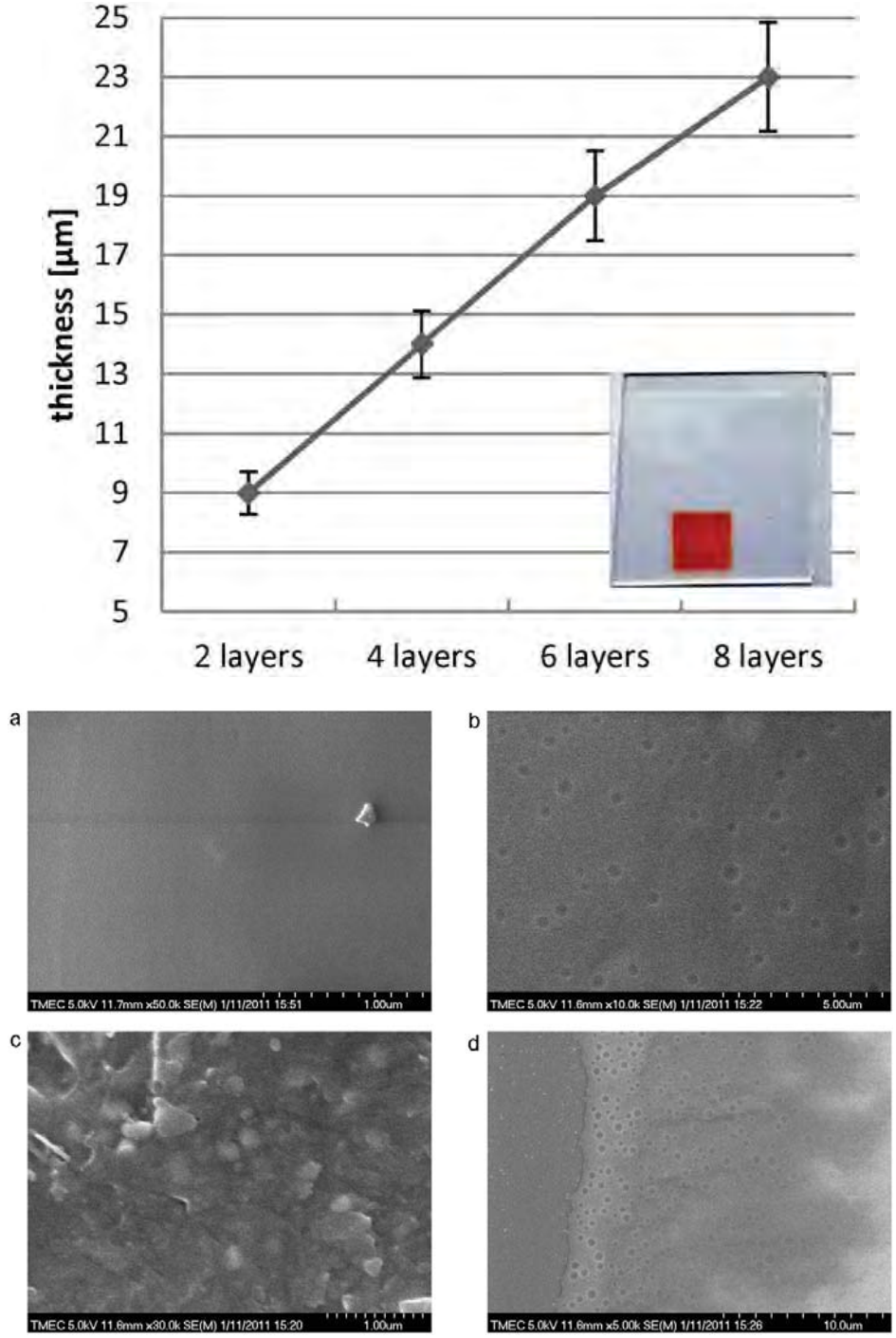

รูปแสดงความหนาของฟิล์มที่ได้จากการพิมพ์แบบอิงค์เจ็ต (Inkjet Printing) ตามจำนวนชั้นที่พิมพ์ และรูปแสดงลักษณะของฟิล์มคอมพอสิตที่ได้จากการพิมพ์

6.13 งานวิจัยเรื่องการทดสอบความเป็นพิษของหมึกกราฟีนผสมคาร์บอนต่อเซลล์มะเร็งเต้านม MDA-MB-231 (Cytotoxicity assessment of MDA-MB-231 breast cancer cells on screen-printed graphene - carbon paste substrate)

กราฟีน (Graphene) เป็นวัสดุคาร์บอนที่ถูกศึกษาอย่างกว้างขวางเพื่อนำมาใช้ในการตรวจวัดด้วยเทคนิคเคมีไฟฟ้า เนื่องจากมันมีความนำไฟฟ้าสูงและมีคุณสมบัติ electrocatalytic ที่ดีเยี่ยม อย่างไรก็ตามในการนำกราฟีนมาใช้งานทางด้านชีวภาพยังคงถูกจำกัด เนื่องจากยังขาดความรู้และความเข้าใจเกี่ยวกับความเข้ากันได้ทางชีวภาพ (Bio-compatibility) ดังนั้นในงานวิจัยนี้จึงเป็นครั้งแรกที่มีการศึกษาความเป็นพิษต่อเซลล์ (cytoxicity) โดยใช้เซลล์มะเร็งเต้านมชนิด MDA-MB-231 ซึ่งเป็น MDA cells ที่เลี้ยงบนฟิล์มที่เป็นวัสดุคาร์บอนเพส (carbon paste และฟิล์มที่เป็นวัสดุผสมของกราฟีนและคาร์บอนเพส (graphene - carbon paste) ซึ่งเตรียมโดยการผสมผงกราฟีนที่สังเคราะห์ได้ลงในหมึกคาร์บอนในปริมาณที่แตกต่างกันและขึ้นรูปเป็นฟิลืมด้วยการพิมพ์แบบอิงค์เจ็ต ความเป็นพิษถูกประเมินจากการอยู่รอดของเซลล์ (cell viability), การยึดเกาะของเซลล์ (cell adhesion), ปริมาณอ็อกซิเจน reactive oxygen species (ROS) ที่เซลล์ผลิตขึ้น และการย้อมสีเซลล์ด้วยสารเรืองแสง (fluorescence staining) ผลการทดลองพบว่า เซลล์ที่เลี้ยงบนฟิล์มคาร์บอนผสมกราฟีนมีชีวิตรอดเพิ่มมากขึ้น เมื่อส่วนผสมของกราฟีนเพิ่มขึ้นจาก 0 to 2.5 wt% แต่จะลดลงเมื่อปริมาณกราฟีนเพิ่มขึ้นมากกว่านี้ และเมื่อเวลาผ่านไปการอยู้รอดของเซลล์ก็จะเหลือน้อยลง ในทำนองเดียวกัน ปริมาณกราฟีนที่ผสมในหมึกคาร์บอนเพสก็จะมีผลต่อการยึดเกาะของเซลล์ในแบบเดียวกับการอยู่รอดของเซลล์ คือจะยึดเกาะดีขึ้นเมื่อมีกราฟีนผสมในปริมาณน้อยๆ แต่จะยึดเกาะได้แย่ลงเมื่อมีกราฟีนผสมอยู่มากขึ้น เช่นเดียวกันกับค่า reactive oxygen species (ROS) ซึ่งจะลดลงเมื่อมีกราฟีนผสมอยู่ ดังนั้นจึงสรุปได้ว่าการที่ฟิล์มมีกราฟีนผสมอยู่เล็กน้อยจะช่วยลดการเป็นพิษต่อเซลล์ นอกจากนี้เรายังทำการย้อมสีของเซลล์ด้วยสารเรืองแสงโดยใช้ Hoechst 33342 ปรากฏว่าการมีกราฟีนผสมอยู่เล็กน้อย เซลล์จะมีชีวิตอยู่รอดได้ดีในจานเลี้ยง ดังนั้นจึงทำให้มีความเข้ากันได้ทางชีวภาพดีขึ้น จากองค์ความรู้นี้ทำให้เราสามารถนำไปต่อยอดเพื่อสร้างเป็นเซ็นเซอร์ทางเคมีไฟฟ้าที่ใช้เซลล์เป็นตัวตรวจวัด (Cell-based Electrochemical Sensor) ผลงานวิจัยนี้ได้รับการตีพิมพ์ในวารสาร Colloids and Surfaces B: Biointerfaces ซึ่งมี ISI Impact Factor 2012 = 3.554 โดยรายละเอียดดังนี้ U. Waiwijit, W. Kandhavivorn, B. Oonkhanond, T. Lomas, D. Phokaratkul, A. Wisitsoraat, A. Tuantranont, “Cytotoxicity

assessment of MDA-MB-231 breast cancer cells on screen-printed graphene - carbon paste substrate", Colloids and Surfaces B: Biointerfaces, Available online 11 September 2013

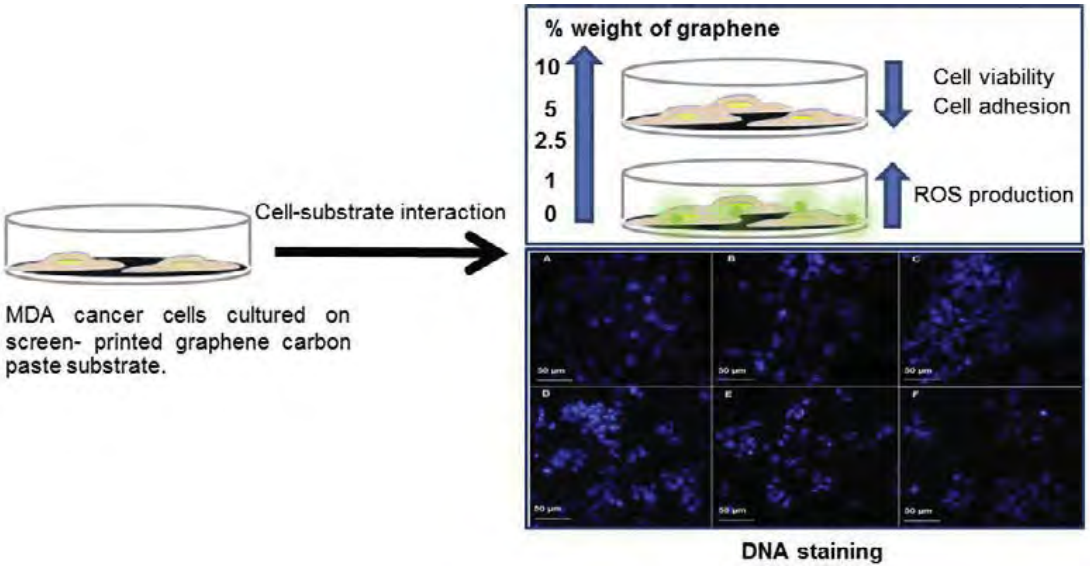

รูปแสดงผลการทดลองการเข้ากันได้และความเป็นพิษต่อเซลล์ของหมึกคาร์บอนผสมกราฟีน

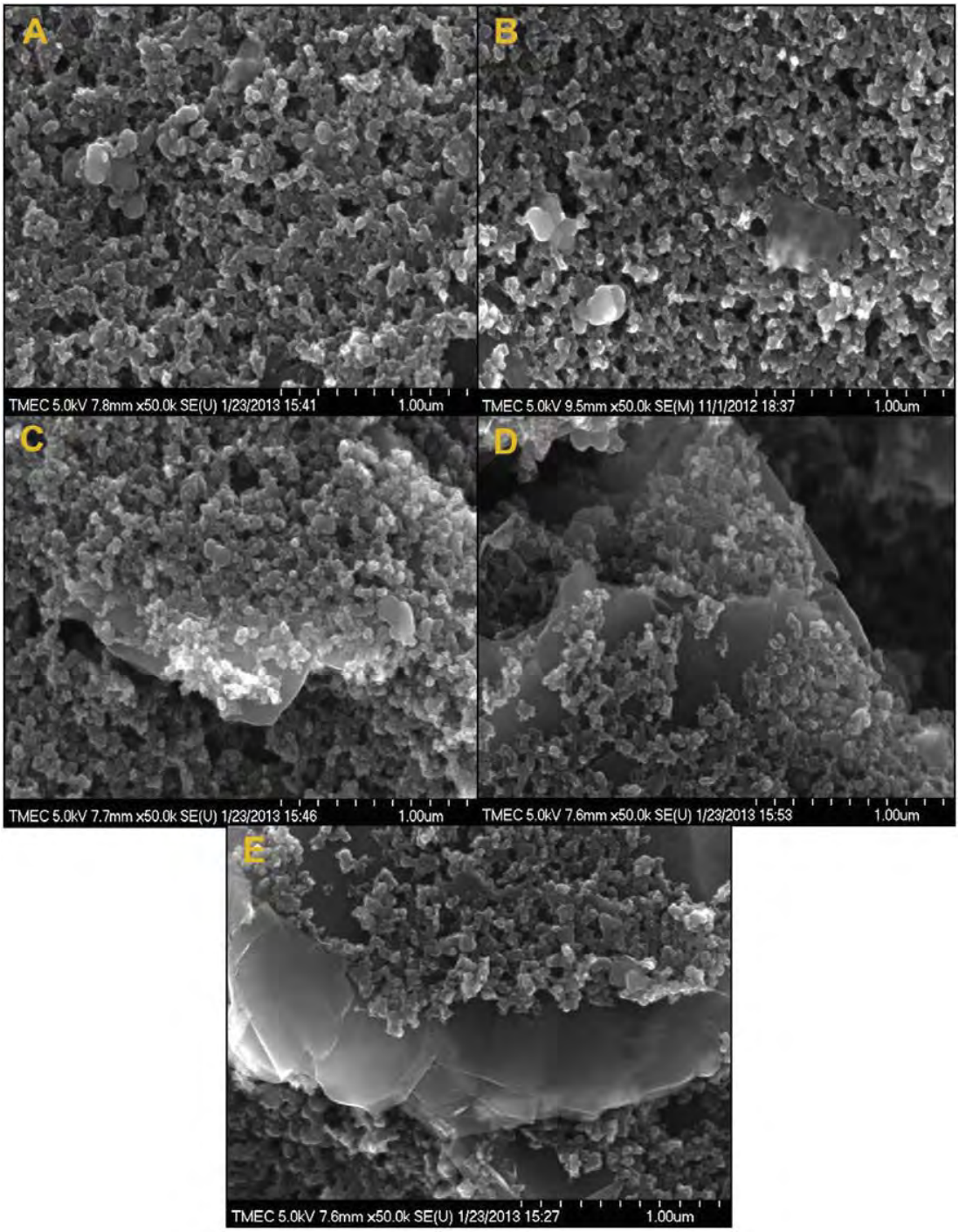

รูปแสดงลักษณะผิวของฟิล์มที่ใช้ทดสอบการเป็นพิษต่อเซลล์มะเร็ง โดยมีปริมาณส่วนผสมของกราฟีนที่เพิ่มมากขึ้นจาก 0%, 1%, 2.5%, 5% และ 10% ตามลำดับจากรูป A-E

ผลงานที่ได้รับ (Output)

การดำเนินการวิจัยเป็นไปเกินแผนที่วางไว้ ได้ตีพิมพ์ผลงานในวารสารวิชาการที่มี ISI ตั้งแต่เริ่มโครงการ จนถึงปัจจุบัน (3 ปี) เรียงตามลำดับวันที่ตีพิมพ์ จากเริ่มต้นโครงการจนถึงปัจจุบัน ได้ดังนี้

1) C. Karuwan, A. Wisitsoraat, A. Sappat, K. Jaruwongrungsee, V. Patthanasettakul, and **A. Tuantranont***,"Vertically Aligned Carbon Nanotube Based Electrochemical Sensor for Salbutamol Detection,", ***Sensor Letters***, pp.645-650, August 2010.(2010 ISI IF= 0.602)

2) U. Sungkanak, A. Sappat, A. Wisitsoraat, C. Promptmas, **A. Tuantranont***, “Ultrasensitive detection of *Vibrio cholerae* O1 using microcantilever-based biosensor with dynamic force microscopy” , ***Biosensors and Bioelectronics***, Volume 26, Issue 2, 15 October 2010, Pages 784-789(ISI Impact factor 2010 =5.361)

3) A. Wisitsoraat, P.Sritongkham, C.Karuwan, D.Phokharatkul, T.Maturos, **A.Tuantranont***,**"**Fast cholesterol detection using flow injection microfluidic device with functionalized carbon nanotubes based electrochemical sensor,"***Biosensors and Bioelectronics***, Volume 26, Issue 4, 15 December 2010, Pages 1514-1520 (ISI Impact factor 2010 =5.361)

4) K. Rodaree, T. Maturos, S. Chaotheing, T. Pogfay, N. Suwanakitti, C. Wongsombat, K. Jaruwongrungsee, A. Wisitsoraat, S. Kamchonwongpaisan, T. Lomas, **A. Tuantranont***, “DNA hybridization enhancement using piezoelectric microagitation through a liquid coupling medium, “ ***Lab on a Chip***, vol. 11, pp. 1059, 2011. (ISI Impact factor 2010 =6.26)

5) **A.Tuantranont*** , A. Wisitsora-at, P. Sritongkham, K. Jaruwongrungsee , “A review of monolithic multichannel quartz crystal microbalance: A review ,” ***Analytica Chimica***

Acta, Volume 687, Issue 2, 21 February 2011, Pages 114-128 (ISI Impact factor 2010 =4.310)

6) C. Karuwan, K. Sukthang, A. wisitsoraat, D. Phokharatkul, V. Patthanasettakul, W. Wechsatol, **A. Tuantranont***, “Electrochemical detection on electrowetting-on-dielectric digital microfluidic chip,” ***Talanta*** 84(5), pp. 1384-1389, June 2011.(ISI Impact factor 2010 =3.722)

7) D. Phokharatkul, C. Karuwan, T. Lomas, D. Nacapricha, A. Wisitsoraat, **A. Tuantranont***, “AAO–CNTs electrode on microfluidic flow injection system for rapid iodide sensing,” ***Talanta*** 84(5), pp. 1390-1395, June 2011.(ISI Impact factor 2010 =3.722)

8) T. Maturos, T. Pogfay,. K. Rodaree,S.Chaotheing, A.Jomphoak,A.Wisitsoraat, N.Suwanakitti, C.Wongsombat, K.Jaruwongrungsee,P. Shaw,.S.Kamchonwongpaisanb and **A.Tuantranont***, "Enhancement of DNA hybridization under acoustic streaming with three-piezoelectric-transducer system", ***Lab Chip*** Vol.12, 2012, p.133. (ISI Impact factor 2011 =6.306)

9) C. Karuwan, C. Sriprachuabwong, A.Wisitsoraat, D. Phokharatkul,P. Sritongkham and **A. Tuantranont***, "Inkjet-printed graphene-poly(3 ,4 -ethylenedioxythiophene):poly(styrene-sulfonate) modified on screen printed carbon electrode for electrochemical sensing of salbutamol", ***Sensors and Actuators B*** Vol.161, 2012 p. 549– 555, November 2011(ISI Impact factor 2011 =3.898)

10) J. Ph. Mensing, T. Kerdcharoen, C. Sriprachuabwong, A. Wisitsoraat, D. Phokharatkul, T. Lomas and **A. Tuantranont***, “Facile preparation of graphene–metal phthalocyanine hybrid material by electrolytic exfoliation”, ***J. Mater. Chem.,*** 2012, 22, (ISI Impact factor 2011 = 5.968)

11) A. Wisitsoraat, S. Pakapongpan, C. Sriprachuabwong, D. Phokharatkul, P. Sritongkham, T. Lomas, **A. Tuantranont*,** “Graphene–PEDOT:PSS on screen printed carbon electrode for enzymatic biosensing”, **Journal of Electroanalytical Chemistry** Vol .70 ,2013, p.208–213, (ISI Impact factor 2012 = 2.672)

12) J. Ph. Mensing, A. Wisitsoraat, **A. Tuantranont,** T. Kerdcharoen, “Inkjet-printed sol–gel films containing metal phthalocyanines/porphyrins for opto-electronic nose applications” **Sensors and Actuators B** Vol.176 ,2013, p.428– 436 (ISI Impact factor 2012 =3.535)

13) U. Waiwijit, W. Kandhavivorn, B. Oonkhanond, T. Lomas, D. Phokaratkul, A. Wisitsoraat, **A. Tuantranont***, “Cytotoxicity assessment of MDA-MB-231 breast cancer cells on screen-printed graphene - carbon paste substrate”, Colloids and Surfaces B: Biointerfaces, Available online 11 September 2013

ผลงานหนังสือ

Adisorn Tuantranont (Editor) หนังสือ Applications of Nanomaterials in Sensors and Diagnostics (Springer Series on Chemical Sensors and Biosensors) ปี 2013

Book chapters

Adisorn Tuantranont, “Nanomaterials for Sensing Applications: Introduction and Perspective,” Springer Publishing, Springer Series on Chemical Sensors and Biosensors, 2013

Anurat Wisitsoraat, Adisorn Tuantranont, “Graphene-Based Chemical and Biosensors,” Springer Series on Chemical Sensors and Biosensors, 2013

Pornpimol Sritongkham, Anurat Wisitsoraat, Adisorn Tuantranont, Mithran Somasundrum, “Integration of CNT-Based Chemical Sensors and Biosensors in Microfluidic Systems,” Springer Series on Chemical Sensors and Biosensors, 2013

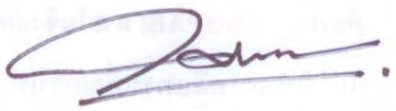

ลงนาม .....

(หัวหน้าโครงการวิจัยผู้รับทุน)

ภาคผนวก

SENSOR LETTERS
Vol. 8, 645–650, 2010

RESEARCH ARTICLE

Vertically Aligned Carbon Nanotube Based Electrochemcial Sensor for Salbutamol Detection

Chanpen Karuwan, Anurat Wisitsoraat, Assawapong Sappat, Kata Jaruwongrungsee, Viyapol Patthanasettakul, and Adisorn Tuantranont*

Nanoelectronics and MEMS Laboratory, National Electronics and Computer Technology Center, 112 Thailand Science Park, Pahol Yothin Rd., Klong Luang, Pathumthani 12120, Thailand

(Received: 13 January 2010. Accepted: 4 April 2010)

This paper reports electrochemical sensing of salbutamol, a prohibited drug in sports, with a new working electrode based on vertically aligned carbon nanotubes (V-CNT). V-CNTs were synthesized by chemical vapor deposition using acetylene and argon gases at 700 °C on gold coated silicon substrates. A simple electrochemical cell including V-CNTs, silver wire (Ag) and platinum (Pt) wire was designed. Electrochemical characterization by cyclic voltammetry (CV) was carried out with different salbutamol concentrations ranging from 10^{-7} to 10^{-4} mol·l^{-1}. CV curves exhibited irreversible oxidation peak at ~0.7 V. The current response was linear with sensitivity of 0.13 μA/mol·l^{-1} and a minimum detection of 3×10^{-7} mol·l^{-1}. In addition, its pharmaceutical applications were demonstrated. The direct analysis of salbutamol in pharmaceutical products yielded a good analytical feature with wide dynamic working range (0.5 to 100 μM) and matrices' interference was found to be negligible. Thus, V-CNTs electrode is a potential candidate for the electrochemical detection of salbutamol.

Keywords: Vertically Aligned Carbon Nanotube, Electrochemical Sensor, Salbutamol, Cyclic Voltammetry.

1. INTRODUCTION

Carbon nanotubes (CNTs) have been recently studied by analytical chemists as sensors because of its excellent properties including unique electronic band structure, extreme strength, very high thermal conductivity and superconductivity. CNTs have been widely used as electrochemical electrodes in various applications of electroanalysis[1–7] due to their high reaction area and excellent electron transfer rate.[8] CNTs can be grown by chemical vapor deposition (CVD).[5–7,9] CVD is one of the most suitable methods for CNTs growth because of its low cost and low deposition temperature.[10]

Salbutamol or 4-[2-(tert-butylamino)-1-hydroxyethyl]-2(hydroxymethyl) phenol is the most widely used β_2 adrenergic receptor agonists, which induces bronchodilation, making the drug highly useful for curing bronchial asthma and other allergic diseases associated with respiratory pathway.[11–13] However, high dose of salbutamol is prohibited in sports because of its abuse as a stimulant and anabolic agent. Hence, the use of salbutamol is only permitted for athletes having asthma. World Anti-Doping Agency (WADA) has prohibited the oral use of salbutamol and a concentration greater than 1000 ng/ml (3 μM) in urine is considered as an indication of doping.[14,15]

Due to the necessity to detect and monitor β-agonists, several devices and methods have been developed for determination of these compounds, including gas chromatography with mass spectrometric detection (GC-MS)[16,17] and high performance liquid chromatographic (HPLC) method with UV-detection. These methods have normally been utilized for gold-standard determination of salbutamol in athletes.[18–20] Recently, quick detection methods are reported based on electrochemical[21] and MS[22–23] detections or capillary electrophoresis (CE) with MS[24] and amperometric[25] detections.

Among all techniques, electrochemical sensing is a promising alternative for β-agonists sensing due to its fast detection and high sensitivity. Recently, electrochemical detection of β-agonists by various electrodes including glassy carbon, carbon paste, carbon disk, boron doped diamond and fullerene electrodes have been reported.[21,25–30] In this work, CNTs are used as electrodes for salbutamol sensing. A simple electrochemical cell including CNTs as

*Corresponding author; E-mail: adisorn.tuantranont@nectec.or.th

1546-198X/2010/8/645/006 doi:10.1166/sl.2010.1324

working electrode, silver wire as reference electrode and platinum wire as auxiliary electrode is designed for cyclic voltammetric measurement.

2. EXPERIMENTAL DETAILS

2.1. Apparatus

A potentiostat, μ-autolab Type III (Metrohm, Switzerland) was used for all cyclic voltammetric (CV) studies. A single-compartment three electrode system comprised a CNTs working electrode, a platinum wire counter electrode and a silver wire reference electrode. The CNTs electrode was fabricated by CVD technique. The 0.5-mm Pt and 1.0-mm Ag wires were purchased from Aldrich (USA).

2.2. Chemicals and Reagents

All chemicals used in this work were analytical grade reagents. Salbutamol was purchased from Sigma (USA). 0.1 mM citric acid (pH 4) was prepared by mixing 10 ml of 2 M citric acid (Merck, Germany) and 4 ml of 2 M sodium hydroxide (Merck, Germany). 0.1 mM Citric acid (pH 6) was made by mixing 10 ml of 2 M citric acid (Merck, Germany) and 6 ml of 2 M sodium hydroxide (Merck, Germany). A 0.1 mM phosphate buffer (pH 7) was prepared by mixing 19.5 ml of 0.2 M sodium phosphate monobasic monohydrate (Merck, Germany) and 30.5 ml of 0.2 M sodium phosphate dibasic (Merck, Germany). A 0.1 M tris buffer (pH 8) was made by mixing 50 ml of 0.2 M tris(hexahydroxy)aminomethane (Merck, Germany) and 29.2 ml of 0.1 M hydrochloric acid (HCl) (Lab Scan, Ireland). 0.1 M Tris buffer (pH 10) was prepared similarly by pH adjustment using 0.1 M hydrochloric acid solutions. The stock solution (0.01 mol l^{-1}) of salbutamol was prepared by dissolving ~30 mg of salbutamol in deionized-distilled water. Finally, salbutamol solutions with different concentrations were prepared by adding the stock solution in these buffers solutions.

2.3. Electrode Fabrication

The structure of CNTs electrode is shown in Figure 1. The working electrode was fabricated on ⟨100⟩ Si substrate. First, SiO_2 (400 nm), Ti (50 nm) and Au (500 nm) were successively sputtered on the substrate. Next, titanium dioxide (300 nm) was sputtered on the gold layer over a defined electrode region, which excludes active sensing (1 mm^2) and electrical contact area. Next, aluminum oxide (10 nm) and stainless steel (SS) catalyst (5 nm) were successively sputtered over the active area through shadow masking for CNT synthesis. The titanium dioxide and aluminum oxide layer were deposited by reactive sputtering at a pressure of 3×10^{-3} mbar with 1:5 Ar:O_2 gas mixture while other metallic layers were deposited by pure Ar gas at the same pressure.

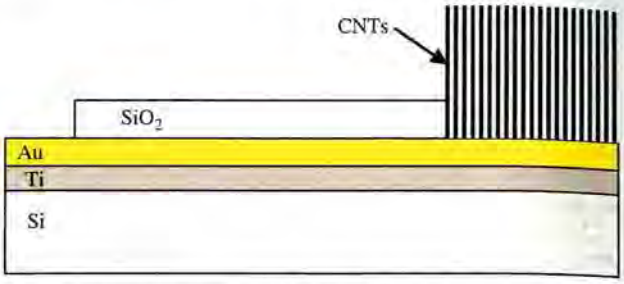

Fig. 1. Schematic diagram of V-CNTs electrode structure.

2.4. V-CNT Synthesis

V-CNTs were then grown by thermal chemical vapor deposition (CVD) with gravity effect and water-assisted etching.[31–32] The catalyst layers on substrates were placed upside down along gravitational field on an alumina carrier in a horizontal furnace thermal CVD system. CNTs synthesis was conducted at atmospheric pressure and growth temperature of 700 °C. During CNTs growth, acetylene was flowed for 1.5 minute and hydrogen to acetylene flow ratio was 4:3:1. In the course of CNT growth, *in-situ* water-assisted etching was employed to remove undesired amorphous carbon formation from random acetylene decomposition. In water etching process, 300 ppm of water vapor was introduced by water bubbling through Ar gas for 3 minutes while acetylene gas was turned off. CNTs growth and water-assisted etching were repeatedly performed for two cycles.

2.5. Electrochemial Cell and Electrochemical Set Up

Cyclic voltammetry is a basic technique, which is widely used for characterization behavior of an analyte. A home made electrochemical cell with three electrode system consisted of a Pt wire auxiliary electrode, an Ag wire reference electrode and a CNTs working electrode. The volume of cell was 1.0 ml.

3. RESULTS AND DISCUSSION

3.1. CNTs Electrode

The surface morphology of the sensing area of CNTs based electrode was examined using scanning electron microscopy (SEM) as shown in Figure 2. It can be seen that the fabricated CNTs are vertically aligned with a height of ~30 μm. Figure 3 shows a 1.0-ml home made electrochemical cell with three electrode system consisted of a Pt wire auxiliary electrode, an Ag wire reference electrode and a CNTs working electrode.

3.2. Performance of GC and CNTs Electrodes

In order to assess the sensitivity of CNTs electrode, the electrochemical characteristics of CNTs electrode in 1 mM

Fig. 2. Photograph of fabricated electrode and SEM micrograph of V-CNTs electrochemical electrode.

salbutamol in citric buffer (pH 6.0) was compare to that of commercial glassy carbon (GC) electrodes as shown in Figure 4. It can be seen that the CNTs electrode exhibits much higher irreversible oxidation peak at ~0.75 V than GC electrode does. Thus, CNTs significantly enhance the electrochemical activity with salbutamol due to its high reaction area and excellent electron transfer rate. The CV curves at 5 mM salbutamol concentration of electrode with no CNTs and with CNTs have been reported by Karuwan et al.[33] Similarly, CNTs electrode exhibits much higher irreversible oxidation peak than gold electrode does. The oxidation peak of salbutamol at ~0.7 V can be explained by oxidative reaction of phenolic hydroxyl group.[34] The mechanism of salbutamol oxidation has been proposed based on the pathway of phenol.[29] The oxidative reaction of salbutamol can be illustrated in Figure 5.[13, 28, 35] In the reaction, sabutamol molecule (A) is oxidized by electrochemical potential and becomes salbutamol free radical (B) giving one electron and one proton. The free radicals are unstable so they will react with each other to form dimers (C).

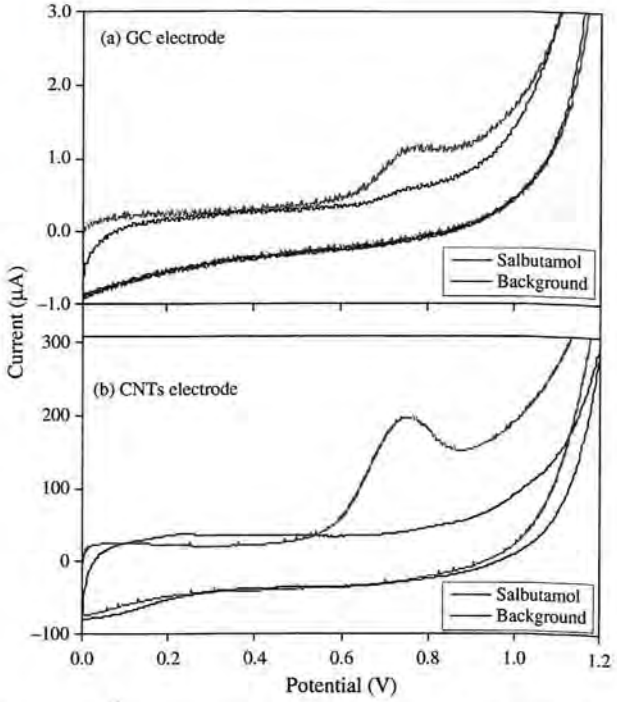

Fig. 4. Cyclic voltammogram of 1 mM salbutamol using GC (a) and CNTs (b) electrode. Scan rate was 100 mVs^{-1}. Buffer solution is citric acid/sodium hydroxide pH 6.0.

3.3. Selection of Electrolyte

In general, solubility and dissociation of an analyte are affected to some extent by pH of its buffer. The electrochemical characteristics of salbutamol were thus studied in buffer solutions with different pHs ranging from 4 to 10.

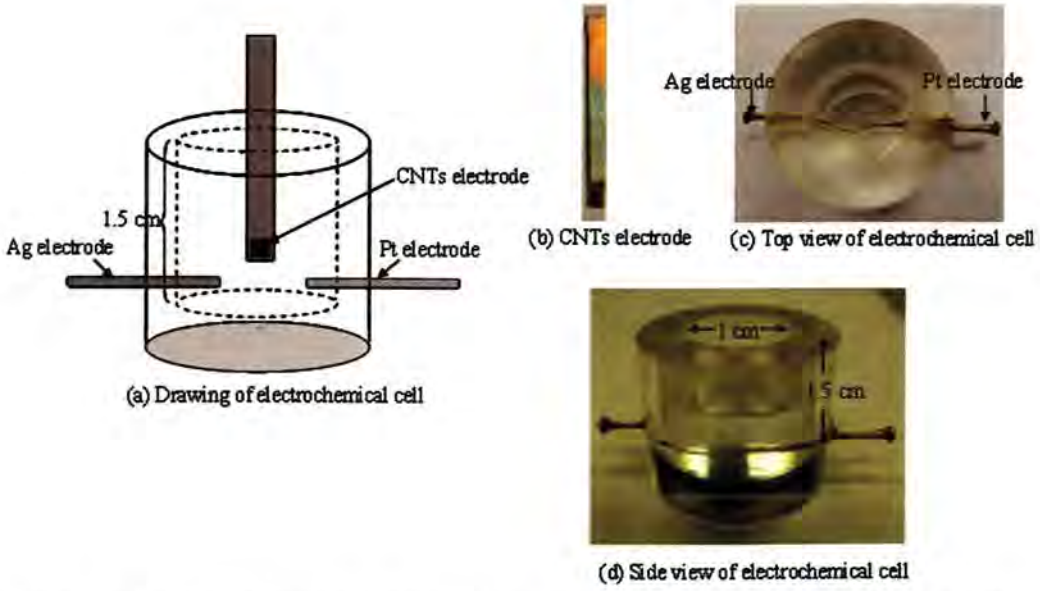

Fig. 3. Home-made electrochemical cell with three electrode system consisted of platinum wire auxialary electrode, Ag wire reference electrode and CNTs working electrode. The electrochemical cell was made from acrylic piece with 1.0 cm diameter and 1.5 cm height. The voltage window used for CV experiments is from 0 to +1.0 V.

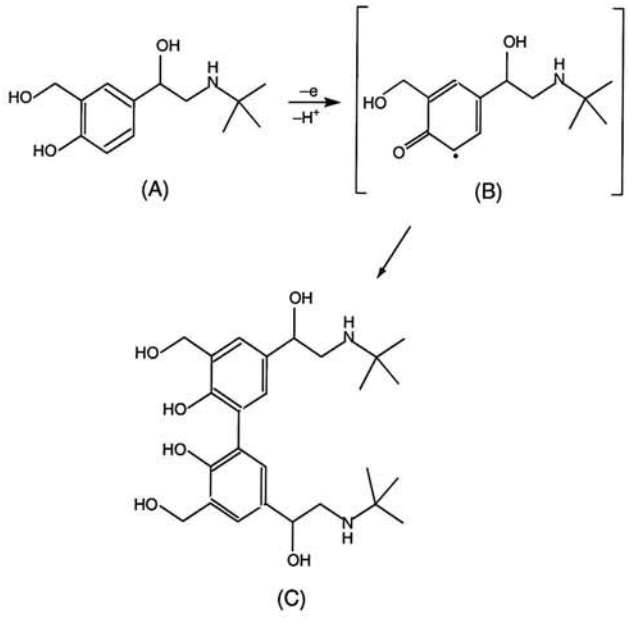

Fig. 5. Oxidation reaction of salbutamol on V-CNTs electrode.

It was found that the salbutamol current response was weakly depending on pH and pH value of 6 was a locally optimal condition that gave high electrochemical response. Thus, this buffer was selected for further studies.

3.4. Scan Rate Dependence Study

CV responses were then taken with different scan rates as illustrated in Figure 6. The oxidation peak amplitude is found to increase linearly with the square root of scan rate, indicating that the current is limited by semi-infinite diffusion of salbutamol on CNTs electrode. It should be noted that the effect of scan rate on the background is not shown for clarity. However, the inset in Figure 6 has been properly plotted with background subtraction at different scan rates.

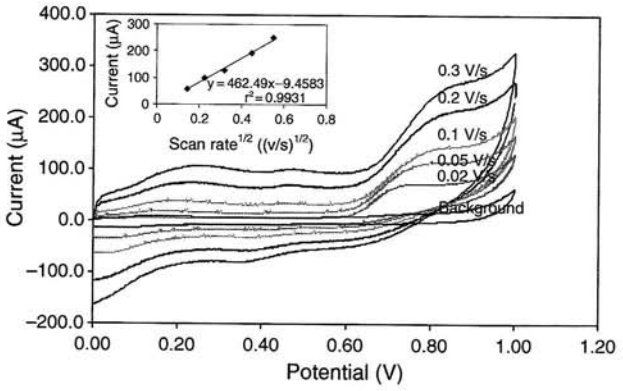

Fig. 6. Cyclic voltammograms obtained at various potential scan rates of 1 mM standard solutions of salbutamol in citric acid/sodium hydroxide pH 6.0. The inset picture shows the relationship between square root of the scan rate and current response. (Working electrode: V-CNTs, Reference electrode: silver wire, Auxiliary electrode: Pt.)

3.5. Concentration Study

The CV measurements were made with different concentrations as illustrated in Figure 7(a). The amperometric response of oxidation peak as a function of concentration is shown in the inset of Figure 7(b). It is observed that peak current of salbutamol varies linearly with concentration in the range 0.5–100 μM. At low concentration (less than 0.5 μM), peak current of salbutamol also varies linearly but with a higher slope value. On the other hand, the response current begins to level off at higher salbutamol concentrations (200–400 μM).

3.6. Stability of CNTs Electrode

The stability of CNTs electrode was checked by recording successive cyclic voltammograms. After 20 cycles, no change was observed in the voltammetric profiles of CNTs electrode. Even in the presence of salbutamol, the electrode remained stable after 20 successive cycles with relative standard deviation (RSD) of 8.9%. Furthermore, no significant change in the response was observed for more than two months after the electrode was stored at room temperature. Moreover, reproducibility of CNTs electrode was determined from seven sensors fabricated in the same batch and RSD of 14.7% was obtained. Therefore, CNTs electrodes have satisfactory repeatability and reproducibility.

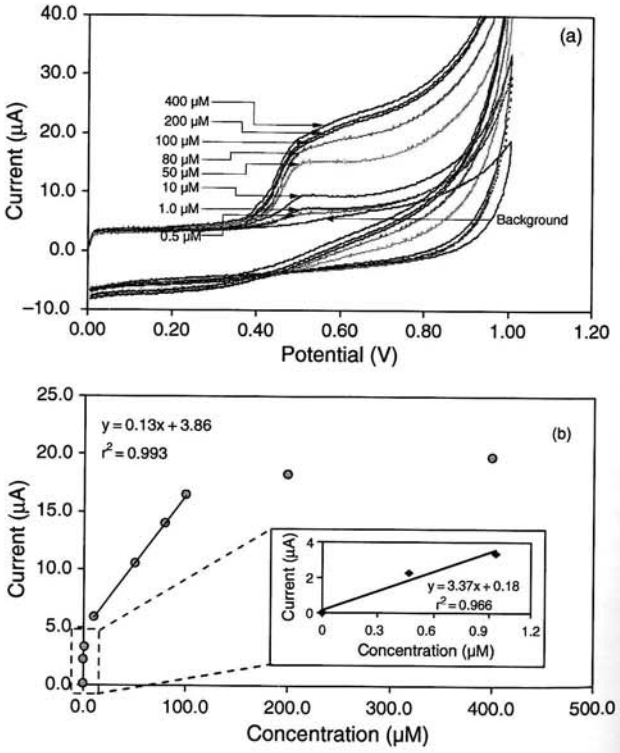

Fig. 7. Cyclic voltammograms of salbutamol solutions with different concentrations in citric acid/sodium hydroxide (pH 6.0) (a). Calibration curve of oxidation peak as a function of concentration (b). (Working electrode: V-CNTs, Reference electrode: silver wire, Auxiliary electrode: Pt.)

Table I. Comparison of analytical performance of CNTs electrode and other data reported in literature.

References	Methods	Linear dynamic range (μM)	Correlation coefficient (r^2)	Detection limit (μM)
Our work	V-CNTs electrode with cyclic voltametry	0.5 and 100	0.993	0.3
Yilmaz et al. [34]	PT electrode with cyclic voltametry	100–1000	0.9996	80
Yilmaz et al. [34]	GC electrode with cyclic voltametry	20–1000	0.9997	10
Karuwan et al. [28]	BDD electrode with amperometric detection	0.5–100	0.999	0.1
Zhou et al. [25]	Carbon-disk electrode with CE-amperometric detection	0.3 to 50	0.998	0.2
Quintino et al. [26]	GC electrode with batch injection analysis	0.8 to 200	0.9995	0.25
Goyal et al. [13]	Au nanoparticles on ITO electrode with differential pulse voltametry	0.2 to 8.4	—	0.3

Pt electrode: Platinum electrode; GC electrode: Glassy carbon electrode; BDD electrode: Boron doped diamond electrode; CE: Capillary electrophoresis; Au: Gold electrode; ITO: Indium thin oxide.

It should be noted that repeatability and reproducibility were measured at 100 μM sabutamol concentration.

3.7. Analytical Features

The analytical performance of CNTs electrode for salbutamol detection is summarized in Table I. Linear concentration dependence or dynamic range is observed between 0.5 and 100 μM. The regression equation is given by $y = 0.13x + 3.86$ ($r^2 = 0.993$), where y and x are the height of peak current (μA) and salbutamol concentration (μM), respectively. The slope of the equation is corresponding to linear sensitivity of 0.13 μA/μM. It should be noted that the calibration line does not go to zero due to nonlinearity of the sensor in the low concentration region. The detection limit (3S/N) is as low as 0.3 μM. The noise value (N) is measured by taken peak–peak amplitude of sinusoidal noise in the base line region of CV curve.

The analytical performance of CNTs electrode with cyclic voltametry is compared to other reports in literature as listed in Table I. It is evident that CNTs electrode is significantly better than GC and Pt electrodes based on cyclic voltametry detection.[34] Moreover, the result is comparable to electrochemical detection of salbutamol by boron-doped diamond (BDD) electrode using amperometric detection,[28] carbon-disk electrode with CE-amperometric detection,[25] GC electrode with batch injection analysis[26] and gold nanoparticles modified indium tin oxide electrode using Osteryoung square wave voltammetry.[13] For a given electrode, it is well known that amperometric detection, batch injection analysis and Osteryoung square wave voltammetry generally yield lower detection limit than cyclic voltammetry. This implies that the CNTs based electrode should offer better salbutamol detection due to its larger surface area compared to gold nanoparticles, BDD, and GC. In addition, the CNTs based electrode exhibits wider dynamic range than the reported gold nanoparticle based sensors, which is only between 0.2 and 6 μM.

Table II. Comparison of the labeled values of salbutamol in pharmaceutical products and the analyzed results by HPLC-UV and CV using V-CNTs electrode.

Sample name	Content of salbutamol (mg/L)		
	Label	HPLC-UV	V-CNTs
1. Ventolin syrup	400	401 ± 3	406 ± 5
2. Asmasal syrup	400	403 ± 2	413 ± 3

3.8. Performance for Pharmaceutical Applications

Salbutamol content in syrup samples were analyzed by the developed electrochemical system. The measured results were compared to the labeled values from their manufacturer and results from high performance liquid chromatography with ultraviolet detection (HPLC-UV) as shown in Table II. HPLC-UV measurement was conducted by the manufacturer (IDS Manufacturing Ltd., Thailand). According to pair t-test,[36] the results for Ventolin and Asmasal are not significantly different at 95% confidence ($t_{stat} = 3.0$, $t_{critical} = 12.70$). It is clear that our results are in good agreement with those from HPLC-UV. Moreover, recovery studies made for the samples show that the matrices have small influence on electrochemical oxidation of salbutamol (115–121% recovery). Thus, the samples can be directly analyzed by our method with low matrices' interference. However, it was found that interference occurred in other pharmaceutical products such as Ventolin tablets. Thus, the electrode doesn't possess general anti-interference capability. Sample pretreatment including separation is needed to overcome the interference problem in general cases especially urine samples, which contain very complex matrices.

4. CONCLUSIONS

This work presents the utilization of vertically align carbon nanotube (V-CNT) for electrochemical detection of salbutamol. Cyclic votammetry (CV) gives a well-defined irreversible oxidation peak of this compound. The method provides good analytical features with wide dynamic working range (0.5 to 100 μM) compared to another report on gold nanoparticle based sensor. In addition, the detection limit (3S/N) is as low as 0.3 μM. Furthermore, this method is suitable for direct analysis of salbutamol in pharmaceutical product with low matrices' interference.

Acknowledgments: Adisorn Tuantranont would like to express his gratitude for Researcher Career Development Grant from Thailand Research Fund (TRF).

References and Notes

1. S. Roy, H. Vedala, and W. Choi, *Nanotechnol.* 17, S14 (**2006**).
2. J.-E. Huang, X. Hong, and H.-L. Li, *Carbon* 41, 2731 (**2003**).
3. Y. Yun, Z. Dong, and M. Schulz, *J. Nano. Today* 2, 30 (**2007**).
4. A. Wisitsoraat, A. Tuantranont, E. Comini, G. Sberveglieri, and W. Wlodarski, *Proceeding IEEE* 550 (**2007**).
5. A. Wisitsoraat, A. Tuantranont, C. Thanachayanont, and P. Singjai, *Proc. 1st IEEE International Conference on Nano Micro Engineered and Molecular Systems*, January (**2006**), p. 1487.
6. Y. Wanna, N. Srisukhumbowornchai, A. Tuantranont, A. Wisitsoraat, N. Thavaungkul, and P. Singjai, *J. Nanosci. Nanotechnol.* 6, 3893 (**2006**).
7. A. Wisitsoraat, A. Tuantranont, C. Thanachayanont, V. Patthanasettakul, and P. Singjai, *J. of Electroceram.* 17, 45 (**2006**).
8. S. Shahrokhian and H. R. Zare-Mehrjardi, *Electrochim. Acta* 52, 6310 (**2007**).
9. S. Chaisitsak, J. Nukeaw, and A. Tuantranont, *Diamond Relat. Mater.* 16, 958 (**2007**).
10. M. S. Dresselhaus, G. Dresselhaus, and P. Avouris, Carbon Nanotubes: Synthesis, Structure, Properties, and Applications, Springer, Berlin, New York (**2001**).
11. J. E. F. Reynolds (ed.), Martindale: The Extra Pharmacopoeia, Elsevier, London (**1993**).
12. M.-H. Spyridaki, P. Kiousi, A. Vonaparti, P. Valavani, V. Zonaras, M. E. Zahariou, G. Tsoupras, and C. Georgakopoulos, *Anal. Chim. Acta* 573, 242 (**2006**).
13. R. N. Goyal, M. Oyama, and S. P. Singh, *J. Electroanal. Chem.* 611, 140 (**2007**).
14. A. Pichon, N. Venisse, E. Krupka, M.-C. Perault-Pochat, and A. Denjean, *Int. J. Sports Med.* 27, 187 (**2006**).
15. World Antidoping Agency, Avilable: http://www.wada-ama.org/.
16. M. C. Dumasia and E. Houghton, *J. Chromatogr.* 564, 503 (**1991**).
17. M. P. Montrade, B. L. Bizec, F. Monteau, B. Siliart, and F. Andre, *Anal. Chim. Acta* 275, 253 (**1993**).
18. N. El-Enany, F. Belal, and M. Rizk, *Anal. Chem.* 49, 587 (**2004**).
19. I. H. I. Habib, M. E. M. Hassouna, and G. A. Zaki, *Farmaco.* 60, 249 (**2005**).
20. C. Gabiola, M. A. Garcia-Calonge, M. P. Portillo, J. A. Martinez, and A. S. de. Barrio, *J. Microcol. Sep.* 8, 361 (**1996**).
21. L. A. Lin, R. S. Tomlinson, and R. D. Stazger, *J. Chromatogr. A* 762, 275 (**1997**).
22. L. Debrauwer, G. Delous, and G. Bories, *Chromatographia* 36, 218 (**1993**).
23. L. Debrauwer and G. Bories, *Anal. Chim. Acta* 275, 231 (**1993**).
24. M. H. Lamoree, N. J. Reinhoud, U. R. Tjaden, W. M. Niessen, and A. van der Greef, *J. Biol. Mass Spectrom.* 23, 339 (**1994**).
25. T. Zhou, Q. Hu, H. Yu, and Y. Fang, *Anal. Chim. Acta* 441, 23 (**2001**).
26. M. S. M. Quintino and L. Angnes, *Talanta* 62, 231 (**2004**).
27. S. Moane and B. Jose-Ramon, *J. Pharm. Biomed. Anal.* 14, 57 (**1995**).
28. C. Karuwan, T. Mantim, P. Chaisuwan, P. Wilairat, K. Grudpan, P. Jittangprasert, Y. Einaga, O. Chailapakul, L. Suntornsuk, O. Anurukvorakun, and D. Nacapricha, *Sensors* 6, 1837 (**2006**).
29. Z. J. Fang, W. H. Bin, T. Nakashima, T. N. Rao, and A. Fujishima, *J. Phys. Chem. B* 107, 13389 (**2003**).
30. R. N. Goyal, D. Kaur, S. P. Singh, and A. K. Pandy, *Talanta* 75, 63 (**2008**).
31. L. Zhu, J. Xu, Y. H. Xiu, Y. Y. Sun, D. W. Hess, and C. P. Wong, *Carbon* 44, 253 (**2006**).
32. L. Zhu, J. Xu, F. Xiao, and C. P. Wong, *Carbon* 45, 344 (**2007**).
33. C. Karuwan, A. Wisitsoraat, T. Maturos, D. Phokharatkul, A. Sappat, K. Jaruwongrungsee, T. Lomas, and A. Tuantranont, *Talanta* 79, 995 (**2009**).
34. N. Yilmaz, S. A. Ozkan, B. U. Z. Senturk, and I. Biryol, *J. Chem.* 22, 175 (**1998**).
35. S. Griese, D. K. Kampouris, R. O. Kadara, and C. E. Banks, *Electrochim. Acta* 53, 5885 (**2008**).
36. J. H. Miller and J. C. Miller, Statistics and Chemometrics for Analytical Chemistry, Fourth edn., Pearson Education Ltd., Essex (**2000**), pp. 48–50.

Biosensors and Bioelectronics 26 (2010) 784–789

Contents lists available at ScienceDirect

Biosensors and Bioelectronics

journal homepage: www.elsevier.com/locate/bios

Ultrasensitive detection of *Vibrio cholerae* O1 using microcantilever-based biosensor with dynamic force microscopy

Usa Sungkanak[a], Assawapong Sappat[b], Anurat Wisitsoraat[b], Chamras Promptmas[a], Adisorn Tuantranont[b,*]

[a] *Department of Clinical Chemistry, Faculty of Medical Technology, Mahidol University, Nakhon Pathom 73170, Thailand*
[b] *Nanoelectronics and MEMS Laboratory, National Electronics and Computer Technology Center, 112 Paholyothin Rd., Klong Luang, Pathumthani 12120, Thailand*

ARTICLE INFO

Article history:
Received 1 February 2010
Received in revised form 25 May 2010
Accepted 20 June 2010
Available online 1 July 2010

Keywords:
Microcantilever
Vibrio cholerae O1
Biosensor
Dynamic force microscopy

ABSTRACT

This work presents the first demonstration of a cantilever based *cholerae* sensor. Dynamic force microscopy within atomic force microscope (AFM) is applied to measure the cantilever's resonance frequency shift due to mass of cell bound on microcantilever surface. The *Vibrio cholerae* O1, a food and waterborne pathogen that caused cholera disease in human, is a target bacterium cell of interest. Commercial gold-coated AFM microcantilevers are immobilized with monoclonal antibody (anti-*V. cholerae* O1) by self-assembled monolayer method. *V. cholerae* O1 detection experiment is then conducted in concentrations ranging from 1×10^3 to 1×10^7 CFU/ml. The microcantilever-based sensor has a detection limit of $\sim 1 \times 10^3$ CFU/ml and a mass sensitivity, $\Delta m/\Delta F$, of ~146.5 pg/Hz, which is at least two orders of magnitude lower than other reported techniques and sufficient for *V. cholerae* detection in food products without pre-enrichment steps. In addition, *V. cholerae* O1 antigen–antibody binding on microcanilever is confirmed by scanning electron microscopy. The results demonstrate that the new biosensor is promising for high sensitivity, uncomplicated and rapid detection of *V. cholerae* O1.

1. Introduction

Vibrio cholerae is a causative agent of cholera and belongs to a group of organisms whose natural inhabitant is in an aquatic environment. Even though the endemic areas of cholera are reported only in Africa, Asia and Latin America, there are many imported cases reported in many countries worldwide (WHO). Until now, *V. cholerae* has been classified into 155 serogroups based on somatic antigen (O antigen), but only O1 and O139 are found to associate with cholera outbreaks (Louis et al., 2003; Gubala, 2006). *V. cholerae* O1 is gram-negative curved-rod bacterium and oxidase-positive (Jyoung et al., 2006), which is identified as a food and waterborne pathogen that causes cholera or severe diarrhea disease (Bhowmick et al., 2009). One of common sources of *V. cholerae* O1 is contaminated food, especially, seafood products.

The conventional method for detection and identification of bacterial pathogens relies on microscopic examination and biochemical identification. Although these techniques are inexpensive and give both quality and quantitative information, they are time consuming and cannot detect VNC (viable but non-cultureable) form (Baker et al., 1983; Colwell, 2000). Various monitoring techniques have been developed to detect the toxigenic *V. cholerae* including enzyme-linked immunoassorbent assay (ELISA), polymerase chain reaction (PCR) (Koch et al., 1993; Lyon, 2001; Martinez et al., 2001), real time PCR (Blackstonea et al., 2007), multiplex PCR (Rivera et al., 2003) and DNA probe hybridization technique (Yoh et al., 1993; Wright et al., 1992). These techniques provide high sensitivity for toxigenic *V. cholerae* detection but they require pre-enrichment, molecule labeling, high skill operator and multiple detection steps.

Therefore, an easy-to-use *cholerae* biosensor with sufficiently high sensitivity is needed. Various *bacterial* sensors based on surface plasmon resonance (SPR) (Jyoung et al., 2006; Koubova et al., 2001), quartz crystal microbalance (QCM) (Mao et al., 2006), waveguide-based immunosensors (Horvath et al., 2003) and amperometric immunosensors (Rao et al., 2006) have been demonstrated. However, these techniques have several disadvantages including limited assay life-time, complicated detection steps and insufficient sensitivity for detection of *V. cholerae* O1 in food products.

Microcantilever is a relatively new sensing platform, which offers excellent sensitivity and very low detection limit (Thundat et al., 1995). By combining the microcantilever and dynamic force microscopy (DFM) in atomic force microscope (AFM), adsorbed molecules can be detected from the information of resonance frequency shift. In DFM, a microcantilever is driven to its resonance

* Corresponding author. Tel.: +66 2564 6900; fax: +66 2564 6756.
E-mail address: adisorn.tuantranont@nectec.or.th (A. Tuantranont).

0956-5663/$ – see front matter © 2010 Elsevier B.V. All rights reserved.
doi:10.1016/j.bios.2010.06.024

frequency by piezoelectric actuator. If target molecules adsorbed onto microcantilever, its resonance frequency will decrease due to mass loading (Lang et al., 2002). Thus, the variation of mass on the cantilever causes a resonance frequency shift and the shift is proportional to the amount of adsorbed molecules (Lang et al., 2005; Nugaeva et al., 2007). In addition, this sensing system offers high sensitivity by the aid of optical detection in AFM. Recently, numerous microcantilever-based biosensors have been reported (Hwang et al., 2009). These include microcantilevers for the detection of prostate specific antigen (PSA) (Lee et al., 2003), DNA (Su et al., 2003; Illic et al., 2005), vaccinia virus particle (Gunter et al., 2003; Gupta et al., 2004a,b, 2006) and microorganisms such as *Escherichia coli* O157:H7 (Campbell and Mutharasan, 2005; Ilic et al., 2000). However, there has been no report of microcantilever-based biosensor for *V. cholerae* O1 detection.

This work presents the first demonstration of a cantilever based *cholerae* sensor. In this system, antibody of *V. cholerae* O1 is immobilized on gold-coated microcantilever surface by self-assembled monolayers (SAMs) method and the resonance frequency shift of microcantilever due bacteria binding is measured by DFM as a function of *V. cholerae* concentration. In addition, the sensing structure is examined by scanning electron microscope (SEM). This sensing device will be useful in clinical microbiology laboratories for prevention and control endemic of cholera.

2. Materials and methods

2.1. The principle of dynamic force microscopy

The principle of dynamic force microscopy is illustrated in Fig. 1a. Cantilever is vibrated over a sample surface at its resonance frequency with a fixed resonance amplitude, *A*. This resonance frequency differs from eigen frequency f_0 of free standing cantilever because interaction force between tip at the end of cantilever and sample. The average distance between tip and sample surface is called *d* and the nearest distance between tip at the oscillation peak and sample surface is assigned as *D*. The resonance amplitude *A* is a function of *d*, which can be changed by adjusting the cantilever position relative to sample surface.

Characteristics of frequency shift (Δ_f) of cantilever can be illustrated by considering interaction potentials as shown in Fig. 1b. When the cantilever is far away from sample surface, cantilever is vibrated under harmonic oscillation in parabolic potential (dotted line). In this case, tip motion is sinusoidal and the resonance frequency is eigen frequency of cantilever, f_0. As distance between tip and sample surface is reduced, tip–sample interaction potential (dashed line) would interact with parabolic oscillation potential (dotted line), resulting in effective potential (solid line). Effective potential is asymmetric and oscillation of tip becomes inharmonic. Thus, the oscillation amplitude, *A*, and resonance frequency, *f*, is decreased when *d* is reduced. As a result, the frequency shift (Δ_f) is controlled by two parameters including *d* and *A* (Holscher et al., 1999).

2.2. Bacteria and culture method

V. cholerae O1 and *Vibrio parahemolyticus* were obtained from Faculty of Medical Technology, Mahidol University, Thailand. These bacteria were grown in Luria–Bertani (LB) plate overnight at 37 °C. The pure colony of each bacterium was picked up into PBS buffer solution and the bacterial concentration was adjusted to of 1×10^8 CFU/ml using spectrophotometer. The bacterial suspensions were boiled in 80 °C water bath for 20 min to kill undesired bacteria and then serially diluted with PBS buffer solution (pH 7.4) to concentrations ranging from 10^2 to 10^7 CFU/ml. One milliliter of

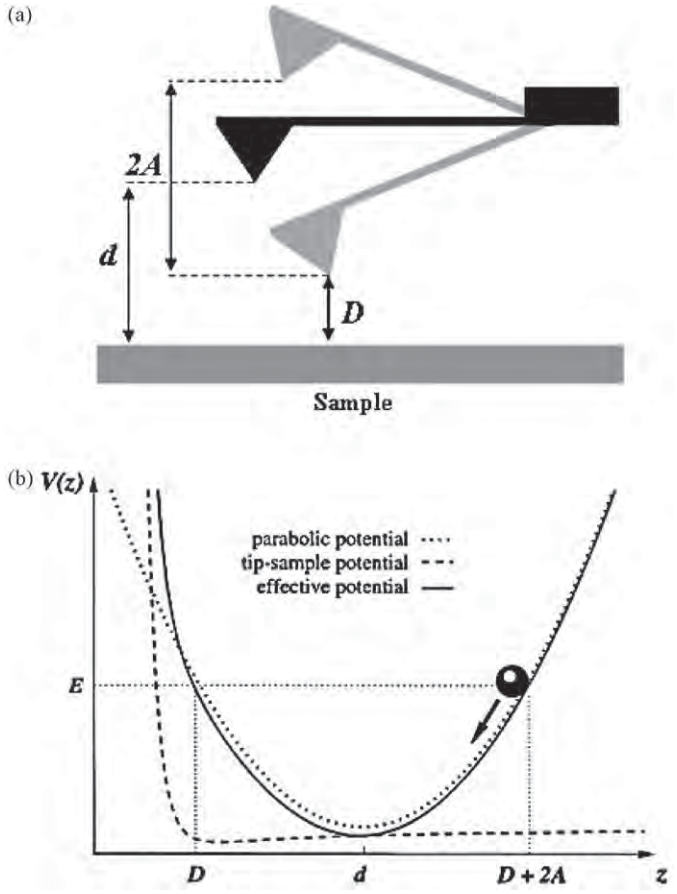

Fig. 1. (a) Scheme of the principle of dynamic force microscopy. (b) Potentials concerning cantilever oscillation in dynamic force microscopy.

bacterial suspension was aliquoted into 1 ml sample container and kept at −20 °C before use.

2.3. Antibody immobilization by self-assembled monolayers

The 250 μm long, 35 μm wide and 1 μm thick gold-coated microcantilever was purchased from NT-MDT Co., Ltd. (NSG10, NT-MDT Co., Ltd., RUSSIA). Before usage, the microcantilever was thoroughly cleaned with piranha solution (conc. H_2SO_4 in 30% H_2O_2; 1:1, v/v) for 5 min to remove organic substance on the surface and subsequently rinsed with deionized water. The freshly cleaned microcantilever surface was modified by simply dipping into the ethanol solution containing 10 mM 3-mercaptoproprionic acid (MPA) for about 3 h at room temperature to form a self-assembled monolayer and then washed with ethanol and deionized water, respectively. In this step, MPA reacted with Au surface leaving free carboxylic groups for further reaction.

The microcantilever was then immersed in the mixture of 200 mM 1-ethyl-3-(3-dimethylaminopropyl)carbodiimide hydrochloride (EDC, Sigma–Aldrich, USA) and 50 mM sulfo-N-hydroxysuccinimide (NHS, Sigma–Aldrich, USA) for 30 min at room temperature to activate the carboxylic groups so that they can form peptide bond with primary amine of antibody. The solution must be prepared immediately before use to avoid loss of activity. After washing with deionized water, 0.5 mg/ml monoclonal antibody (anti-*V. cholerae* O1) in PBS (pH 7.4) was spread over the microcantilever surface. This step was carried out for 1 h at room temperature and excess antibody solution was then washed

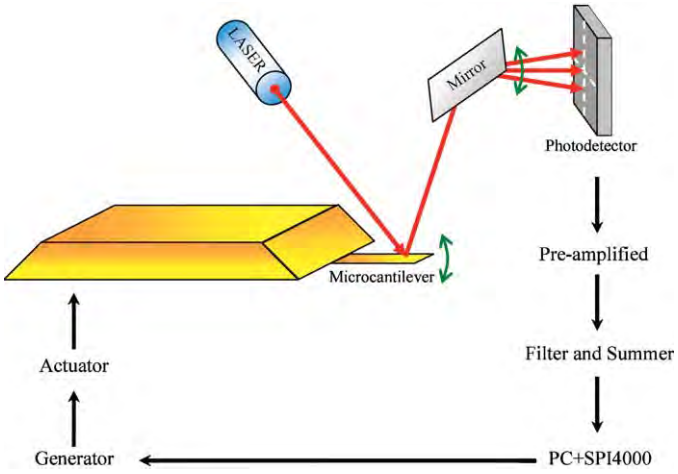

Fig. 2. Schematic drawing of the resonance frequency measurement by optical leverage method of atomic force microscope (AFM).

with PBS buffer solution (pH 7.4). Finally, 3 mg/ml bovine serum albumin (BSA, Sigma–Aldrich, USA) in PBS buffer solution (pH 7.4) was added onto the antibody-immobilized microcantilever surface to prevent unspecific binding on the empty surface in the sensing system.

2.4. Bacteria binding measurement

Antibody-immobilized microcantilevers were immersed in diluted *V. cholerae* O1 suspensions to assess the sensitivity of the sensor and shaking was required for this antigen–antibody reaction. The PBS buffer solution was used as negative control. The immersion time was 5 min to allow forming of antigen–antibody complex. Cross-reactivity experiment was conducted against *V. parahemolyticus* bacteria. The antibody-immobilized microcantilever was dipped into *V. parahemolyticus* suspension with a concentration of 1×10^8 CFU/ml for 5 min under the same experimental conditions as *V. cholerae* O1 detection.

The measurements were performed using atomic force microscope (AFM, SPA400, Seiko, Japan), operated in DFM (dynamic force microscopy) mode. The resonance frequency was measured before (noted as F_0; baseline resonance frequency signal) and after antigen–antibody binding (noted as F_1; test resonance frequency signal). Before measurement, the microcantilever was mounted on microcantilever holder, having electronic interface to the cantilever chip. The cantilever was then driven by mechanical-acoustic excitation using a piezoelectric actuator in close proximity to the cantilever holder. Fig. 2 shows schematic of the resonance frequency measurement.

The cantilever oscillation was measured by the optical beam deflection method, in which an incident beam from laser diode focused on the back end of cantilever. The reflected light from the cantilever surface was detected by a four quadrant photosensitive detector. The cantilever deflection gave the signal which was proportional to the difference in the photocurrents generated in the upper and lower segments. The photocurrents of the upper and lower segments were pre-amplified by an amplifier. The signal was connected to a data acquisition program (SPI 4000, NT-MDT Co., Ltd., Russia) for processing and analysis. The resonance frequency shift was the difference value between F_0 and F_1.

3. Results and discussion

3.1. V. cholerae O1 detection

3.1.1. Antibody immobilization by physical adsorption

The microcantilever coated with monoclonal antibody by physical adsorption was tested with suspension of *V. cholerae* O1 at different concentrations. From experimental results, the shift of resonance frequency from base line (before antigen–antibody binding) tended to be negative (data not shown). The negative shift occurred due to loss of some protein molecules (protein A, antibody and BSA) that were physically adsorbed on the microcantilever. The loss of the molecules on the microcantilever reduced the mass, leading to the increase of resonance frequency. Thus, physical adsorption of antibody is not a good method for antibody immobilization.

3.1.2. Antibody immobilization by chemical adsorption

The microcantilever that was immobilized with monoclonal antibody by self-assembled monolayers (SAMs) was tested with different known concentrations of *V. cholerae* O1 suspension to determine assay sensitivity of the sensor. From experimental results, the resonance frequency of microcantilever decreased as the concentration of *V. cholerae* O1 suspension increased. Fig. 3a shows the resonance frequency shift of the antibody-immobilized microcantilever with different *V. cholerae* O1 concentrations including 1×10^3, 1×10^4, 1×10^5, 1×10^6 and 1×10^7 CFU/ml. The PBS buffer solution was used as negative control (no cell). The results indicated that immuno-complex of antigen and antibody was successfully formed by antigen–antibody reaction, resulting in mass addition on the microcantilever surface.

The calibration curve for *V. cholerae* O1 detection is shown in Fig. 3b. The curve shows relationship of the resonance frequency shift versus the concentration of *V. cholerae* O1 suspension in log scale. It can be seen that the resonance frequency shift is linearly proportional to the log of *V. cholerae* O1 suspension in concentration ranging from 1×10^3 to 1×10^6 CFU/ml. From the experiment, the detection limit of the sensor for *V. cholerae* O1 detection was found to be $\sim 1 \times 10^3$ CFU/ml. This is at least two orders of magnitude lower than that of standard ELISA method (1×10^5 CFU/ml) (Rao et al., 2000) and another reported amperometric immunosensor (1×10^5 CFU/ml) (Rao et al., 2000).

The antibody-immobilized microcantilever was also tested with PBS buffer solution (pH 7.4) in the negative control experiment, in which bacterial cells were not present. The result showed no significant resonance frequency shift (~14 Hz). The additional mass, Δm due to antigen–antibody binding can be straightforwardly related to the shift of resonance frequency of microcantilever according to

$$\frac{1}{f_1^2} - \frac{1}{f_0^2} = \frac{\Delta m}{(4n\pi^2 k)} \quad (1)$$

where k is the spring constant of the cantilever, f_0 is the initial resonance frequency prior to the mass loading, f_1 is the resonance frequency after mass addition (mass of bacteria bound on the microcantilever surface) and n is a geometry-dependent correction factor ($n = 0.24$) if the additional mass is uniformly distributed over a rectangular shaped microcantilever (Gupta and Akin, 2004). Thus, the additional mass of the bacteria cells bound on the microcantilever surface is estimated from Eq. (1) and the results are listed in Table 1. The detection mass sensitivity of the sensor defined by $\Delta m/\Delta F$ is determined to be ~146.5 pg/Hz. High sensitivity and very low detection limit of the sensor have thus been achieved. These can be attributed to very high mass sensitivity of microcantilever sensor and effective antibody immobilization on the cantilever structure by SAMs method.

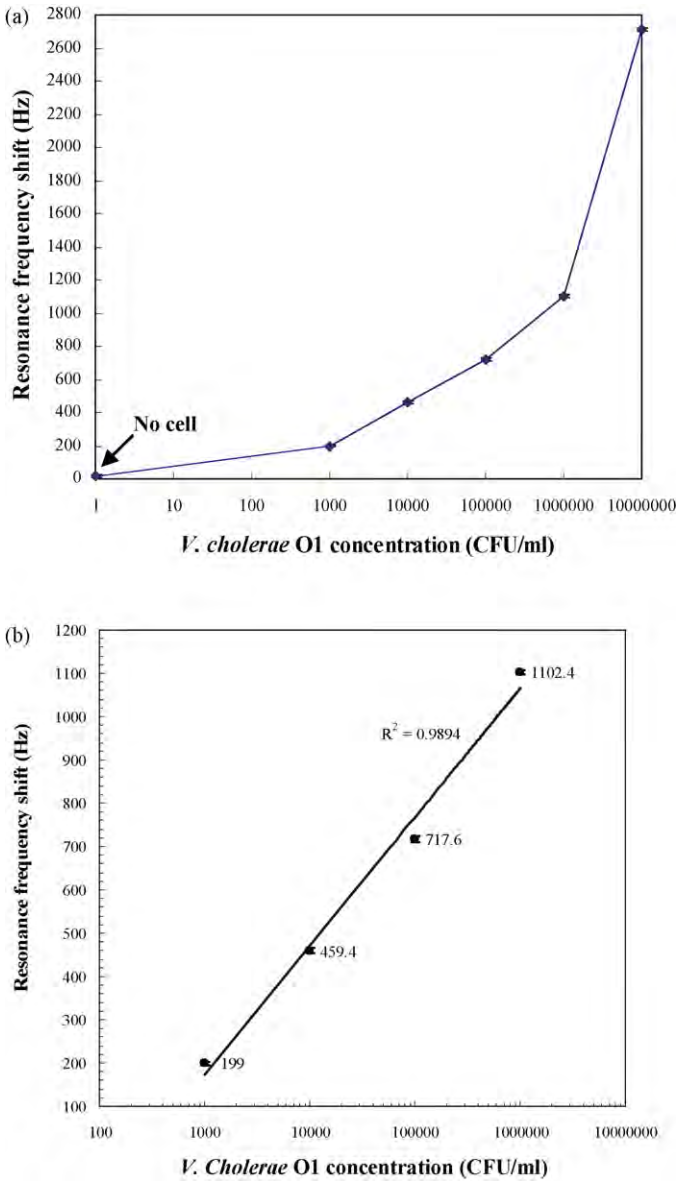

Fig. 3. (a) Relationship of resonance frequency shift versus *V. cholerae* O1 concentration. The control experiment (no cell) was an antibody-immobilized microcantilever tested in PBS buffer solution. Note that 0 is substituted by 1 since it cannot be plotted in log scale. (b) Calibration curve of the resonance frequency shift versus *V. cholerae* O1 concentration. The result shows linearity of *V. cholerae* O1 detection in the range of 10^3–10^6 CFU/ml.

The mass sensitivity and detection limit of the sensor is comparable to those of reported microcantilever sensors for detection of *E. coli* O157:H7 (Campbell and Mutharasan, 2005; Detzel et al., 2006), *Samonella typhimurium* (Zhu et al., 2007) and *Aspergillus niger* (Nugaeva et al., 2007). These reports demonstrate the mass sensitivity of ~50 pg/Hz and the detection limit

Table 1
Estimation of mass change on microcantilever surface.

	Resonance frequency (kHz)			
Concentration (CFU/ml)	1×10^3	1×10^4	1×10^5	1×10^6
ΔF (Hz)	199	459.4	717.6	1100.9
Δm (ng)	30.4	82.6	104.4	121.5
$\Delta m/\Delta F$ (pg/Hz)	152	179	145	110
Average			146.5 pg/Hz	

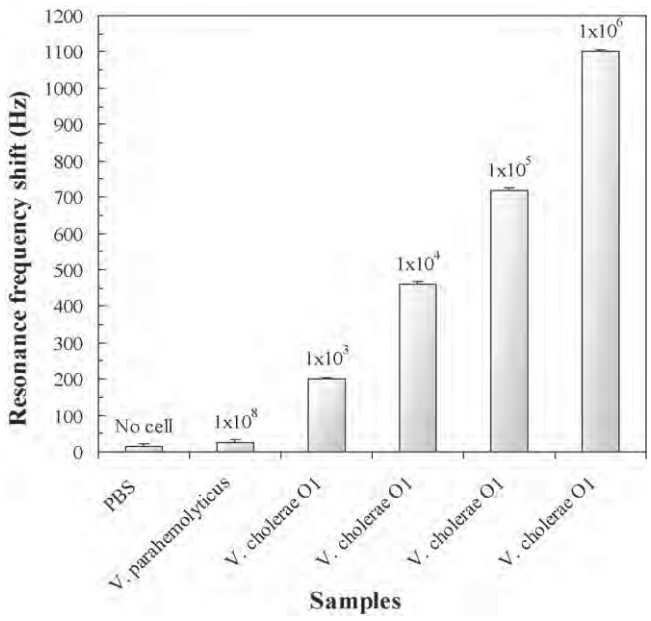

Fig. 4. Cross-reactivity of the sensor: comparison of resonance frequency shift response when the antibody-immobilized microcantilevers were tested with suspension of *V. parahemolyticus*, *V. cholerae* O1, and PBS buffer solution.

of ~1×10^3 CFU/ml. Nevertheless, the mass sensitivity is still several orders lower than those of microcantilevers for detection of *Bacillus anthracis* spores (9.2 fg/Hz) (Davila et al., 2007) and vaccinia virus (6.3 attogram (ag)/Hz) (Gupta et al., 2004a,b). These ultrasensitive microcantilever sensors are specially designed with sophisticated sensing layer and nanometer scale cantilever thickness. It is thus possible to further reduce detection limit of microcantilever sensor for *V. cholerae* O1 detection by employing a specially designed microcantilever. However, detection limit of ~1×10^3 CFU/ml by the commercial microcantilever presented in this work is already satisfactory for use in general microbiological laboratories.

3.2. Cross-reactivity test

V. parahemolyticus bacteria were used to verify the cross-reactivity performance of the sensor. The test was done under the same condition used for *V. cholerae* O1 detection. The antibody-immobilized microcantilever was immersed into 1×10^8 CFU/ml *V. parahemolyticus* with 5-min shaking. It was then washed with PBS buffer solution (pH 7.4) and DI water and dried by nitrogen gas. The resonance frequency of microcantilever was measured before and after immersion in suspension of *V. parahemolyticus*.

Fig. 4 shows the comparison of the resonance frequency shift of antibody-immobilized microcantilever tested with PBS buffer (pH 7.4), 1×10^8 CFU/ml *V. parahemolyticus* suspension and *V. cholerae* O1 with the concentrations between 1×10^3 and 1×10^6 CFU/ml, respectively. The resonance frequency shifts of PBS buffer and 1×10^8 CFU/ml *V. parahemolyticus* were 14.4 and 26.6, respectively while those of *V. cholerae* O1 at concentration of 1×10^3, 1×10^4, 1×10^5 and 1×10^6 CFU/ml were 199.0, 459.4, 717.6 and 1102.4 Hz, respectively. The resonance frequency shift of the antibody-immobilized microcantilever tested with *V. parahemolyticus* suspension is not significant (~24 Hz) compared to those of *V. cholerae* O1. Thus, it can be assumed that the antibody has no cross-reactivity with other strains of bacteria.

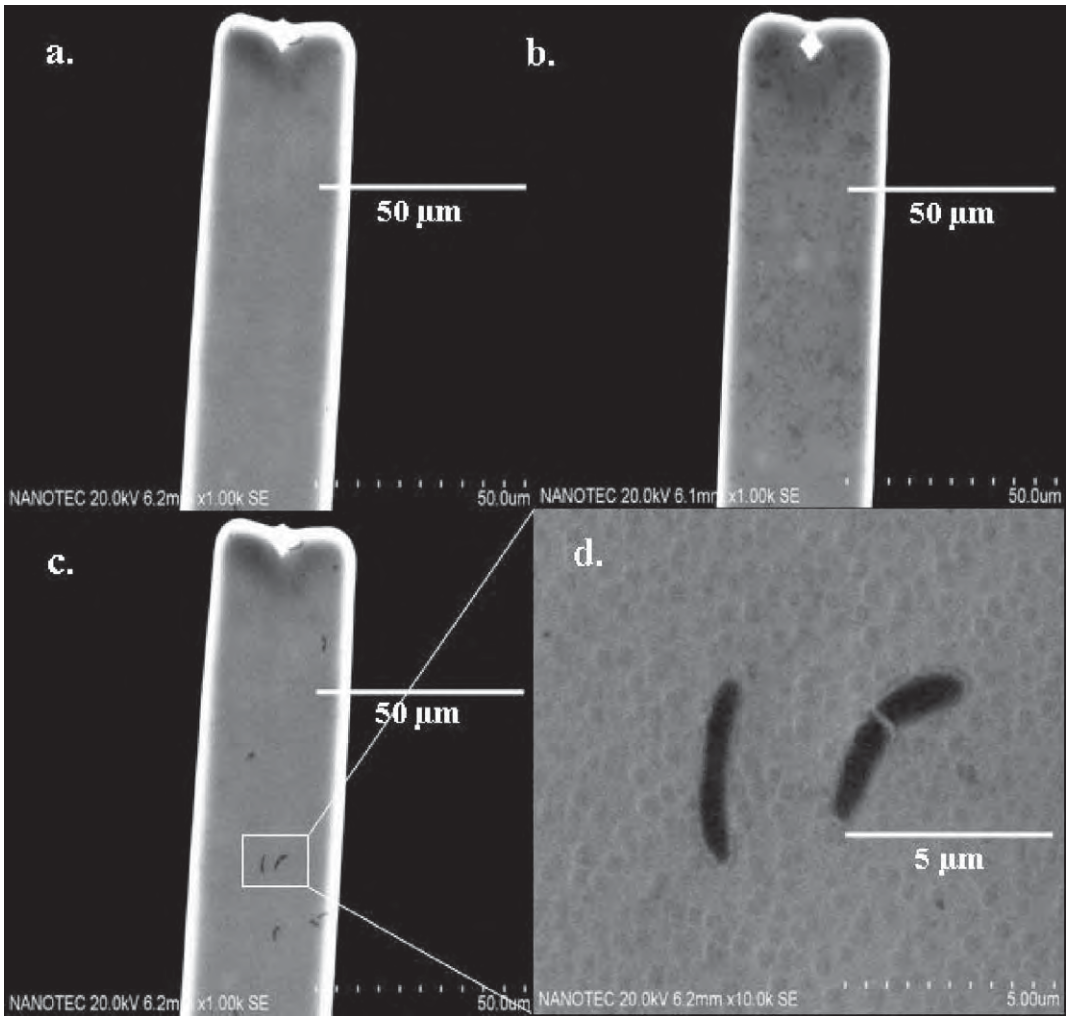

Fig. 5. Scanning electron microscope (SEM) images of antibody-immobilized microcantilever surface (a) before antibody immobilization (b) after antibody immobilization (c) after *V. cholerae* O1 binding at a concentration of 10^3 CFU/ml and (d) high magnification view of *V. cholerae* O1 cells on gold surface.

3.3. Surface characterization

The tested microcantilever was examined by scanning electron microscope (SEM) to characterize *V. cholerae* O1 cells binding on microcantilever surface and to confirm that the resonance frequency shift was generated from the mass of bacteria cells bound on the microcantilever. Fig. 5a and b shows the SEM image of the cantilever beam before and after antibody immobilization, respectively. It can be seen that the cantilever surface before antibody immobilization is very smooth and becomes shaded after the immobilization. However, anti-*V. cholerae* O1 protein molecules immobilized on the gold surface cannot be clearly observed because of its very small size. Fig. 5c demonstrates the SEM micrograph of the microcantilever beam after *V. cholerae* O1 binding at a concentration of 10^3 CFU/ml. It can be observed that thin and long dark cells are now scattered on the cantilever surface and higher magnification view (Fig. 5d) reveals that the cells have curve-rod shaped, which is a typical characteristic of *V. cholerae* bacteria.

It should be noted that the number of *V. cholerae* O1 bacteria may not be precisely counted because of its large size variation and agglomeration. In addition, the cell mass of *V. cholerae* O1 is presently unknown. Thus, it is difficult to correlate the results from surface analysis to the estimated mass change by QCM. Moreover, non-uniform distribution of bacteria would considerably affect the mass change estimation. As a result, the mass change calculated from Eq. (1) may not be accurate. However, it is still useful to estimate the mass change to obtain the order of magnitude of the mass sensitivity.

4. Conclusion

In conclusion, we have developed microcantilever-based biosensor for detection of *V. cholerae* O1, an important food and waterborne pathogen. Commercial gold-coated AFM microcantilevers are immobilized with monoclonal antibody (anti-*V. cholerae* O1) by self-assembled monolayer method. *V. cholerae* O1 detection experiment is performed in concentrations ranging from 1×10^3 to 1×10^7 CFU/ml. The microcantilever sensor has a high sensitivity of ~146.5 pg/Hz and a low detection limit of 1×10^3 CFU/ml, which is at least two orders of magnitude lower than other reported techniques and sufficient for *V. cholerae* detection in food products without pre-enrichment steps. In addition, linear relationship between the resonance frequency and the log of *V. cholerae* O1 concentration is obtained in concentration ranging from 1×10^3 to 1×10^6 CFU/ml. Therefore, the microcantilever-based biosensor is promising for direct detection of *V. cholerae* O1 cells in microbiological laboratories.

Acknowledgements

This work was supported by National Center for Genetic Engineering and Biotechnology (BIOTEC), grant no. BT-B-01-NS-

14-5001. Authors would like to acknowledge Thailand Graduate Institute of Science and Technology (TGIST), Thailand Research Fund (TRF), Prof. Dr. Wanpen Chaicumpa and Dr. Katesara Wataksorn at Mahidol University, Thailand, for their assistance. A.T. would like to acknowledge Thailand Research Fund (TRF) for career developing fund.

References

Baker, R.M., Singleton, F.L., Hood, M.A., 1983. Applied and Environmental Microbiology 46 (4), 930–940.
Bhowmick, T.S., Koley, H., Das, M., Saha, D.R., Sarkar, B.L., 2009. Journal of Antimicrobial Agents 33, 569–573.
Blackstonea, G.M., Nordstroma, J.L., Bowenb, M.D., Meyerb, R.F., Imbroc, P., DePaola, A., 2007. Journal of Microbiological Methods 68 (2), 254–259.
Campbell, G.A., Mutharasan, R., 2005. Analytical Sciences 21, 355–357.
Colwell, R.R., 2000. Journal of Infection and Chemotherapy 6 (2), 121–125.
Davila, A.P., Jang, J., Gupta, A.K., Walter, T., 2007. Biosensors and Bioelectronics 22, 3028–3035.
Detzel, A.J., Campbell, G.A., Mutharasan, R., 2006. Sensors and Actuators B 117, 58–64.
Gubala, A.J., 2006. Journal of Microbiological Methods 65, 278–293.
Gunter, R.L., Delinger, W.G., Manygoats, K., Kooser, A., Porter, T.L., 2003. Sensors and Actuators A 107, 219–224.
Gupta, A., Akin, D., Bashir, R., 2004a. Journal of Vacuum Science and Technology B 22 (6), 2785–2791.
Gupta, A., Akin, D., Bashir, R., 2004b. Applied Physics Letters 84 (11), 1976–1978.
Gupta, A.K., Nair, P.R., Akin, D., Ladisch, M.R., Broyles, S., et al., 2006. Proceedings of the National Academy of Sciences of the United States of America 103, 13362–13367.
Holscher, H., Schwarz, U.D., Wiesendanger, R., 1999. Applied Surface Science 140, 344–351.
Horvath, R., Pedersen, H.C., Skivesen, N., 2003. Optics Letters 28, 1233–1235.
Hwang, K.S., Lee, S.M., Kim, S.K., Lee, J.H., Kim, T.S., 2009. Annual Review in Analytical Chemistry 2, 77–98.
Ilic, B., Czaplewski, D., Craighead, H.G., Neuzil, P., Campagnolo, C., Batt, C., 2000. Applied Physics Letters 77, 450.
Illic, B., Yang, Y., Aubin, K., Reichenbach, R., Krylov, S., Craighead, H., 2005. Nano Letters 5, 925–929.
Jyoung, J.Y., Hong, S., Lee, W., Choi, J.W., 2006. Biosensors and Bioelectronics 21, 2315–2319.
Koch, W.H., Payne, W.L., Wentz, B.A., Cebula, T.A., 1993. Applied and Environmental Microbiology 59 (2), 556–560.
Koubova, V., Brynda, E., Karasova, L., Skvor, J., Homola, J., 2001. Sensors and Actuators B 74, 100–105.
Lang, H.P., Hegner, M., Gerber, C., 2005. Materials Today 8 (4), 30–36.
Lang, H.P., Hegner, M., Meyer, E., Gerber, C., 2002. Nanotechnology 13, R29–R36.
Lee, J.H., Hwang, K.S., Park, J., Yoon, K.H., 2003. Biosensors and Bioelectronics 20, 2157–2162.
Louis, V.R., Estelle, R.C., Choopun, N., Rivera, I.N.G., Gangle, B., Jiang, S.C., Rubin, A., Patz, J.A., Huq, A., Colwell, R.R., 2003. Applied and Environmental Microbiology 69 (5), 2773–2785.
Lyon, W.J., 2001. Applied and Environmental Microbiology 67 (10), 4683–4685.
Mao, X., Yang, L., Su, X.L., Li, Y., 2006. Biosensors and Bioelectronics 21, 1178–1185.
Martinez, G.A., Ambrosio, J., Gutierrez, C.L., Flisser, A., 2001. Clinical and Diagnostic Laboratory Immunology 28 (4), 768–771.
Nugaeva, N., Gfeller, K.Y., Backmann, N., Duggelin, M., Lang, H.P., 2007. Microscopy and Microanalysis 13, 13–17.
Rao, V.K., Sharma, M.K., Goel, A.K., Singh, L., Sekhar, K., 2006. Analytical Sciences 22, 1207–1211.
Rivera, I.N.G., Lipp, E.K., Gil, A., Choopun, N., Huq, A., Colwell, R.R., 2003. Environmental Microbiology 5 (7), 599–606.
Su, M., Li, S., Dravid, V.P., 2003. Applied Physics Letters 82 (20), 3562–3564.
Thundat, T., Wachter, E.A., Sharp, S.L., Warmack, R.J., 1995. Applied Physics Letters 66, 1695–1697.
Wright, A.C., Guo, Y., Johnson, J.A., Nataro, J.P., Morris, J.G., 1992. Journal of Clinical Microbiology 30 (9), 2302–2306.
Yoh, M., Miyagi, K., Matsumoto, Y., Hayashi, K., Takarada, Y., Yamamoto, K., Honda, T., 1993. Journal of Clinical Microbiology 31 (5), 1312–1314.
Zhu, Q., Shin, W.Y., Shin, W.H., 2007. Analyst 22, 3132–3138.

Biosensors and Bioelectronics 26 (2010) 1514–1520

Contents lists available at ScienceDirect

Biosensors and Bioelectronics

journal homepage: www.elsevier.com/locate/bios

Fast cholesterol detection using flow injection microfluidic device with functionalized carbon nanotubes based electrochemical sensor

A. Wisitsoraat*, P. Sritongkham, C. Karuwan, D. Phokharatkul, T. Maturos, A. Tuantranont*

Nanoelectronics and MEMS Laboratory, National Electronics and Computer Technology Center, 112 Pahol Yothin Rd., Pathumthani 12120, Thailand

ARTICLE INFO

Article history:
Received 14 April 2010
Received in revised form 22 July 2010
Accepted 26 July 2010
Available online 3 August 2010

Keywords:
Flow injection
Microfluidic device
Carbon nanotube
Cholesterol
Enzyme based biosensor
In-channel electrochemical detection
Lab-on-a-chip

ABSTRACT

This work reports a new cholesterol detection scheme using functionalized carbon nanotube (CNT) electrode in a polydimethylsiloxane/glass based flow injection microfluidic chip. CNTs working, silver reference and platinum counter electrode layers were fabricated on the chip by sputtering and low temperature chemical vapor deposition methods. Cholesterol oxidase prepared in polyvinyl alcohol solution was immobilized on CNTs by in-channel flow technique. Cholesterol analysis based on flow injection chronoamperometric measurement was performed in 150-μm-wide and 150-μm-deep microchannels. Fast and sensitive real-time detection was achieved with high throughput of more than 60 samples per hour and small sample volume of 15 μl. The cholesterol sensor had a linear detection range between 50 and 400 mg/dl. In addition, low cross-sensitivities toward glucose, ascorbic acid, acetaminophen and uric acid were confirmed. The proposed system is promising for clinical diagnostics of cholesterol with high speed real-time detection capability, very low sample consumption, high sensitivity, low interference and good stability.

1. Introduction

Microfluidic system is a potential platform for biochemical processing and analysis with numerous advantages including low sample/reagent consumption, high sample throughput and total analysis capability (Becker and Locascio, 2002; Rwyes et al., 2002). Recently, plastic/glass based microfluidic platforms have been widely employed in various microfluidic applications. Polymethylmethacrylate (PMMA) (Ford et al., 1998) and polydimethylsiloxane (PDMS) (McDonald et al., 2000) are among the most popular plastic materials for biochemical microsystems due to low cost, ease of fabrication, high chemical/mechanical stability and bio-compatibility (Schoning et al., 2005).

Integration of efficient sensors on microfluidic chips has been one of the most important tasks for the development of micro-total analysis system. Optical detection schemes such as fluorescence, surface plasmon resonance and ultraviolet spectrophotometer have been widely used in biochemical analyses. However, cost and complexity make them impractical for microfluidic platforms. Electrochemical technique is another well-known biochemical detection method, which offers high performance detection as well as compatibility with microsystems (Lin et al., 2008). Recently, electrochemical detection has been embedded in microfluidic systems based on end-channel (Castano-Alvarez et al., 2006; Pozo-Ayuso et al., 2008) and in-channel (Liao et al., 2007; Dossi et al., 2007) detection schemes using different electrode materials, including gold, platinum and carbon paste. Nevertheless, conventional electrochemical electrodes are not fast and sensitive enough for micro-total analysis applications, which involve small analyte volume and short detection time. Therefore, the integration of novel sensing materials in microfluidic platform has been an important research focus for the development of advanced bio/chemical analysis systems.

Cholesterol is an essential lipid with several biological functions in organisms. The determination of cholesterol level in food and blood has been increasingly important for clinical analysis/diagnosis because of reported alarming rise in the rate of clinical disorders due to abnormal levels of blood cholesterol. Thus, there has been continuous effort to develop rapid and sensitive cholesterol sensors and systems (Arya et al., 2008; Li et al., 2010). Electrochemical cholesterol sensors utilizing various matrix and electrode materials with different enzyme immobilization methods have been widely investigated (Vidal et al., 2001; Brahim et al., 2002; Li et al., 2003; Guo et al., 2004; Qiaocui et al., 2005; Yang et al., 2006; Arya et al., 2007; Ansari et al., 2008, 2009; Umar et al., 2009; Solanki et al., 2009; Kaushik et al., 2010).

* Corresponding authors. Tel.: +66 2 564 6900; fax: +66 2 564 6771.
E-mail addresses: anurat.wisitsoraat@nectec.or.th (A. Wisitsoraat), adisorn.tuantranont@nectec.or.th (A. Tuantranont).

0956-5663/$ – see front matter © 2010 Elsevier B.V. All rights reserved.
doi:10.1016/j.bios.2010.07.101

The integration of cholesterol sensor in microfluidic platform will offer instant blood cholesterol determination capability since complete processing from serum extraction to detection can be continuously performed on one chip. Recently, cholesterol sensors based on gold nanowires prepared by electroplating through anodized alumina template were integrated in a microfluidic platform by dielectrophoresis coating (Aravamudhan et al., 2007). However, the reported gold nanowires sensor only provided a factor of two sensitivity improvement relative to a thin gold film electrode because the method produced relatively large-size gold nanowires. In addition, the detection was conducted using square wave voltammetry rather than real-time flow injection analysis due possibly to weak bonding between nanowires and gold contact. Therefore, more efficient nanostructure materials and better integration method should be employed to yield fast and sensitive flow injection based cholesterol detection.

Carbon nanotubes (CNTs) are promising for electrochemical sensing due to huge surface area, high electrical conductivity and excellent electron transfer rate. CNTs have been widely used as sensors in various electroanalysis and bio-sensing applications (Huang et al., 2003; Shahrokhian and Zare-Mehrjardi, 2007; Kirgoz et al., 2007). In addition, CNTs are reported to have excellent cholesterol sensing performance with high sensitivity, low detection potential and fast response (Guo et al., 2004; Li et al., 2005; Roy et al., 2006; Yang et al., 2006; Solanki et al., 2009; Wisitsoraat et al., 2009). Recently, there have been reports on the use of screen printed CNT paste electrodes on microfluidic chips for chemical and biological analyses (Panini et al., 2008; Crevillen et al., 2009; Dossi et al., 2009). Moreover, unmodified CNTs have been directly integrated on glass based microfluidic chip for rapid salbutamol sensing (Karuwan et al., 2009). However, there has been no report on the use of CNTs integrated on a microfluidic chip for real-time cholesterol detection.

In this work, a new cholesterol sensing scheme is developed based on in-channel amperometric flow injection analysis utilizing carbon nanotube (CNT) electrode integrated on a PDMS/glass microfluidic chip. The uniqueness of this approach is the direct growth of CNT electrode on a glass based chip by a low temperature chemical vapor deposition (CVD) process. The on-chip CNTs growth approach offers considerably higher density and better aligned CNT structure with much stronger substrate adhesion than other reported methods including CNT paste printing or dielectrophoresis deposition. It will be an ideal platform for micro-flow injection based biosensors. For cholesterol detection, cholesterol oxidase is immobilized on CNTs by simple but effective in-channel enzyme entrapment using polyvinyl alcohol matrix.

2. Experimental

2.1. Chemicals and reagents

All of chemicals used in this work were analytical grade reagent. Cholesterol (CHO), cholesterol oxidase (ChOx, Pseudomonas fluorescens 25 U/mg), potassium hexacyanoferrate, glucose, acetaminophen, ascorbic acid and Triton X-100 were purchased from Sigma–Aldrich. Phosphate buffer saline (PBS) solution was acquired from Fluka (USA). 98–99% hydrolyzed polyvinyl alcohol (PVA) was obtained from Alfa Aesor (USA). Glass substrates were purchased from Sperior (Germany). PDMS were purchased from Dow Chemical (USA) and photoresist (SU-8 2100) was procured from Micro Chem (USA).

2.2. Apparatus

A potentiostat, μ-autolab Type III (Metrohm, Switzerland) was utilized for all amperometric studies. Spin coater (Laurell technologies Corp, model WS-400A-6NPP) was used for spin coating of photoresist for mold fabrication. MJB4 mask aligner (SUSS microtec, Germany) was the tool for standard UV-lithography process. Oxygen plasma system (Harrick scientific Corp., model PDC-32G) was employed for the treatment of PDMS and glass surfaces. Hitachi S4700 field emission scanning electron microscope (SEM) was used to characterize the morphology of CNT electrodes. Perkin Elmer System—Spectrum Spotlight 300 Fourier transform infrared (FTIR) spectroscopic microscope operated in Specular reflection mode was utilized to identify organic compositions on modified CNT electrodes.

2.3. Fabrication of microfluidic device

The fabrication process consisted of three main tasks. Firstly, PDMS chip containing microchannel was made by micromolding and casting processes. Secondly, three-electrode system was formed on a glass substrate by sputtering and chemical vapor deposition (CVD) processes. Lastly, PDMS and glass chips were bonded using oxygen plasma treatment.

For the fabrication of a PDMS chip, SU8 micromold was fabricated by standard photolithography. SU-8 photoresist was spin-coated on a Si substrate and then soft baked to remove sol-

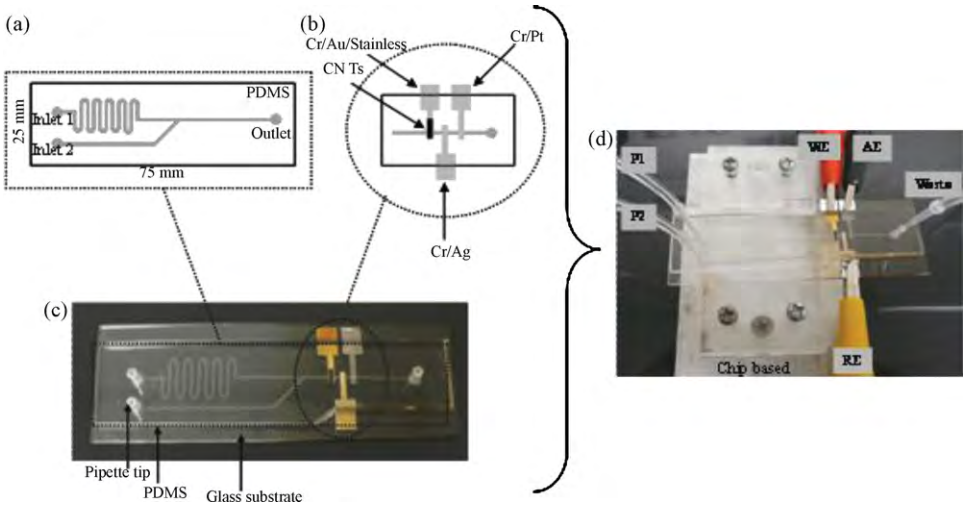

Fig. 1. Diagram and photographs of the microchip with in-channel carbon nanotubes based amperometric detector.

vent in the layer. Next, UV-lithography was performed using MJB4 mask aligner to obtain photoresist patterns on the substrate. The photoresist was then post-baked in order to selectively cross-link the exposed portion of photoresist. Next, the photoresist was developed and cleaned with isopropyl alcohol and deionized water. The microfluidic chip was designed to have two inlets and one outlet as shown in Fig. 1(a). For two inlets, one was used for buffer carrier stream or PVA functionalization and the other was used for injection of analyte or enzyme immobilization. The microchannel was 150 μm deep and 150 μm wide.

In the second part, working (CNTs), auxiliary (Pt) and reference (Ag) electrodes were designed as straight stripes across microchannel and located opposite to the outlet of microchannel as shown in Fig. 1(b). Pt and Ag electrodes were 200 μm wide and 300 nm thick platinum and silver layers each supported by 50 nm Cr adhesive layers while the CNT electrode was formed on a 200 μm wide and 300 nm thick Au contact layer with a 50 nm thick Cr binding layer. For CNT's growth, 10 nm thick aluminum oxide and 5 nm thick stainless steel layers were successively deposited at the end of Au stripe across the microchannel. All layers were deposited and patterned by sputtering through electroplated Ni shadow masks. Ni shadow masks were made by photolithographic patterning and Ni electroplating processes. The aluminum oxide layer was deposited by reactive sputtering at a pressure of 3×10^{-3} mbar of 1:5 Ar/O_2 gas mixtures while other metallic layers were deposited in Ar gas at the same pressure.

CNTs were then grown by a low temperature CVD process (Wisitsoraat et al., 2006). The CVD process was used because of its low cost and ability to produce high quality CNT structure. The prepared glass substrate with electrode and catalyst layers was placed at the gas exit end of a horizontal tube furnace. The furnace was heated up to a center temperature of 700 °C under hydrogen flow of 1500 sccm at atmospheric pressure. It should be noted that high activation center temperature of 700 °C and low substrate temperature of 550 °C were specifically designed to grow CNTs on a glass substrate with melting point of 600 °C. CNTs were grown by acetylene addition with acetylene to hydrogen flow ratio of 1:4 for 1.5 min. In the course of CNT growth, in situ water-assisted etching was employed to remove undesired amorphous carbon formation from random acetylene decomposition (Wisitsoraat et al., 2008). In water etching process, 300 ppm of water vapor was introduced by water bubbling through Ar gas for 3 min while acetylene gas was turned off. CNT's growth and water-assisted etching were repeatedly performed for five cycles.

In the last part, the PDMS and glass chip were treated in 35-W radio-frequency oxygen plasma for 30 s. They were then immediately aligned and attached after oxygen plasma treatment as shown in Fig. 1(c). The inlets and outlet of microchannels were drilled and connected to micro-tubing via pipette tips, which were sealed to PDMS holes by physical attachment as shown in Fig. 1(d). The inlet tubes were connected to syringe pumps and the outlet tube was directed to a reservoir. Finally, the whole apparatus was mounted on an aluminum fixture and electrodes were wired to Potentiostat.

2.4. Enzyme immobilization

Before enzyme immobilization, CNT electrode was functionalized by flow based coating of an aqueous solution of PVA. The polymer solution was prepared by dissolving PVA in deionized water (18.2 MΩ) at a concentration of 0.1% (w/v) and heated to 90 °C for 1 h with constant stirring. The PVA solution was delivered into the channel to CNT electrode using a syringe pump at a flow rate of 10 μl/min for 20 min. Coating with PVA resulted in a highly hydrophilic surface and PVA introduced OH– group on surface, which greatly helped immobilization of various chemical and biological species (Roy et al., 2006).

For enzyme immobilization, cholesterol oxidase solution was prepared by dissolving calculated amount of cholesterol oxidase (25 U/mg) and potassium hexacyanoferrate (redox mediator) in 3 ml PVA solution (0.1% w/v in 0.2 M phosphate buffer, pH 7.0). The cholesterol enzyme concentration was varied between 25 U/ml and 100 U/ml. The enzyme solution was then delivered to CNT electrode using a syringe pump at a flow rate of 10 μl/min for 20 min and PBS buffer stream was flowed to rinse of excess enzyme on CNT electrode. After immobilization, the sensor chip was stored in a refrigerator for 24 h before use.

2.5. Microfluidic flow injection procedure

The 500 mg/dl stock cholesterol solution was prepared by adding required amount of cholesterol to 5 ml of Triton X-100 and then heated up to 90 °C for some time until cholesterol was completely melted. 45 ml of PBS (pH 7.0) solution was then added to Triton X and cholesterol mixture. For interference characterization, the stock solutions of glucose, acetaminophen and ascorbic acid were prepared in deionized water at concentration of 100, 2, 1 and 5 mg/dl, respectively. Before use, all solutions were filtered through 0.2 μm cellulose acetate membrane to prevent clogging in microchannels.

Before flow sensing experiments, microchannels were treated with deionized water for 10 min. PBS running buffer was then continuously delivered into the channel at a flow rate of 40 μl/min. CHO analysis based on flow injection chronoamperometric detection mode was then performed. CHO pulses were injected into the buffer stream and electrochemical current was continuously monitored at a fixed detection potential ranging from +0.3 to +0.6 V vs. Ag reference electrode. Sample injections were performed after stabilization of baseline buffer signal. The current response and throughput were then characterized as a function of injection volume. In addition, the current response was optimized as a function of pH of buffer, enzyme concentration and ambient temperature. The pH of PBS buffer was adjusted by small addition of HCl or NaOH and ambient temperature was controlled by laboratory's air conditioning and heating system. After cholesterol detection, interference responses toward glucose, acetaminophen, uric acid and ascorbic acid were measured at their nominal concentrations.

3. Results and discussion

3.1. On-chip CNT electrode

The surface morphology of on-chip CNT electrode was examined using SEM. Typical top view and cross-sectional view SEM images of CNTs after PVA–enzyme immobilization are shown in Fig. 2(a) and (b), respectively. From Fig. 2(a), it can be seen that CNTs are coated by polymer–enzyme nanoparticles on CNT surface. The size of PVA–enzyme nanoparticles is in the range between 20 and 100 nm. From Fig. 2(b), the nominal diameter of CNTs is ~20 nm and the line density of CNTs is ~40 nanotubes per micron. Thus, the total number of CNTs over 200 μm × 150 μm electrode can be estimated to be $\sim 4.8 \times 10^7$ and approximately 60% of them are coated with PVA–enzyme nanoparticles as seen in Fig. 2(a). The high density CNT integration will be difficult to achieve by other methods including CNT paste printing or dielectrophoresis coating.

The binding of PVA and enzymes on CNT surface was characterized by FTIR spectroscopy. The FTIR spectrum of immobilized CNT electrode is shown in Fig. 3. The observed functional groups indicate successful cholesterol enzyme immobilization. OH band (3200–3570 cm^{-1}), C=O bending peak (~1700 cm^{-1}) and C–O stretching peak (~1110 cm^{-1}) are contributed by PVA (Mansur et

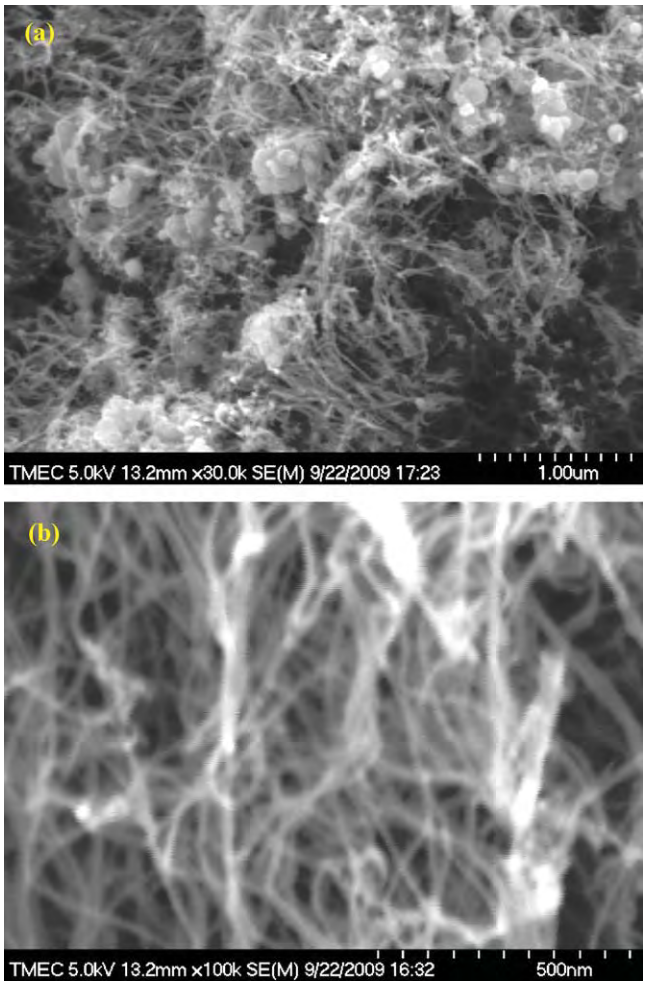

Fig. 2. SEM images of (a) a top view of CNTs on glass substrate with PVA and cholesterol enzyme coating and (b) a cross-sectional view of CNTs at high magnification.

al., 2004) while C–N bending band (740–800 cm^{-1}), COOH peak (1400 cm^{-1}), N–H bending peak (~1570 cm^{-1}: Amide II), C=O stretching peak (~1650 cm^{-1}: Amide I) as well as OH band can be attributed to enzyme molecules (Sulek et al., 2010).

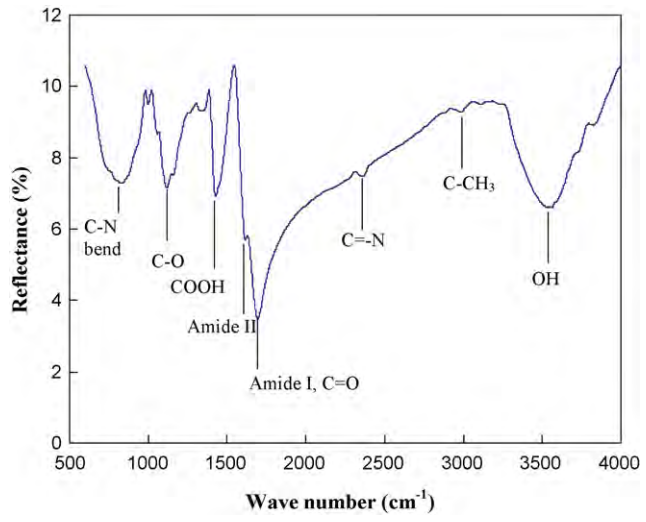

Fig. 3. Typical FTIR spectrum of the CNT electrode after PVA–cholesterol enzyme coating.

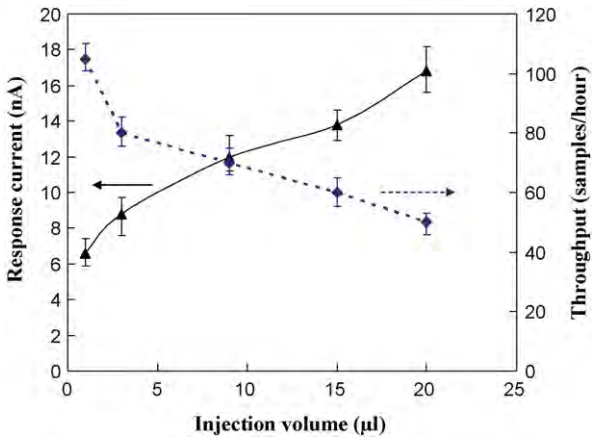

Fig. 4. Effect of injection volume on current response and sample throughput for cholesterol detection at 0.4 V vs. Ag reference electrode and 200 mg/dl cholesterol concentration.

3.2. Optimization of detection parameters

The detection potential affects the sensitivity as well as interference characteristics of current signal for bio-analytes. To obtain suitable detection potential, hydrodynamic voltammetry were studied from injection of 15 μl of 200 mg/dl cholesterol and acetaminophen solutions into the micro-flow system with varying detection potential from 0.3 to 0.7 V. It was found that signal to background (S/B) ratio gradually increased as potential increased from 0.3 to 0.7 V. However, interference from acetaminophen became significant at high detection potentials between 0.5 and 0.7 V. Therefore, 0.4 V bias potential was selected for cholesterol detection in all micro-flow experiments. If not indicated otherwise, sensors were prepared with cholesterol enzyme concentration of 75 U/ml and measurements were performed using PBS buffer with pH of 7 at room temperature (25 °C).

The influence of injection volume on the response of current signal and sample throughput was then characterized to optimize cholesterol detection. Fig. 4 shows current response and throughput vs. injection volume of 200 mg/dl cholesterol solution injected into the buffer stream flowed at a fixed rate at 40 μl/min. The throughput of detection is calculated from the total response time of injection. It can be seen that the current signal increases almost linearly while the throughput monotonically decreases with injection volume. The throughput decreases because the response time increases with injection volume. The injection volume of 15 μl was chosen for compromised sensitivity and throughput (60 samples/h). It should be noted that the *Y*-error bars in this plot (and all subsequent plots) represented the reproducibility from three sensors prepared in the same batch and measurement error over three repeated measurements. It can be seen that CNT sensors has good repeatability and reproducibility with relative standard deviations of less than 15%.

The effect of buffer pH on the sensor response was considered in the range between 6 and 8.5 using PBS buffer solutions. Fig. 5 shows the current response to 200 mg/dl cholesterol solution vs. buffer pH at a fixed buffer flow rate of 40 μl/min and a fixed sample injection volume of 15 μl. It is evident that the optimum pH is in the range between 7.0 and 7.5 and the response rapidly degrades under acidic and basic conditions. This is in accordance with other reports (Solanki et al., 2009; Umar et al., 2009) and the recommended pH for cholesterol oxidase (Noma and Nakayama, 1976). pH of 7 was selected to maximize the enzyme's life time.

The effect of enzyme concentration on the sensor response was studied in the range from 25 U/ml to 100 U/ml. Fig. 6 illustrates the current response to 200 mg/dl cholesterol solution as a func-

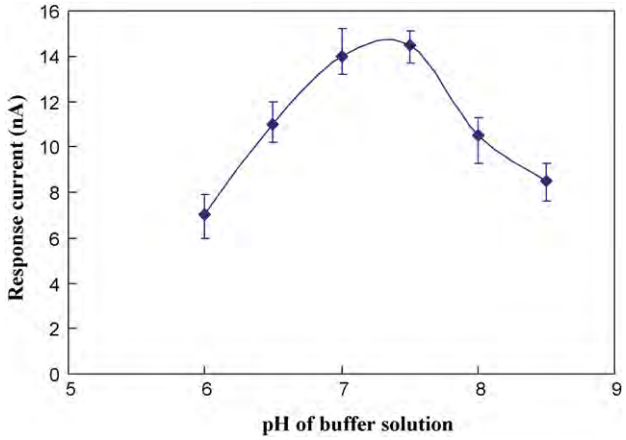

Fig. 5. Effect of buffer pH on current response to 200 mg/dl cholesterol at 0.4 V vs. Ag reference electrode.

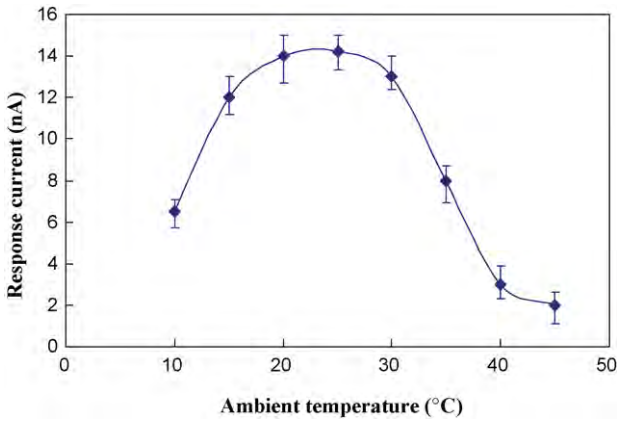

Fig. 7. Effect of ambient temperature on to 200 mg/dl cholesterol at 0.4 V vs. Ag reference electrode.

tion of enzyme concentration tested at a fixed buffer flow rate of 40 μl/min and a sample injection volume of 15 μl. It can be seen that the response initially increases as the enzyme concentration increases and then saturates when the concentration reaches 50 U/ml. Thus, the maximum enzyme entrapment was obtained at the enzyme concentration of 50 U/ml. However, enzyme concentration of 75 U/ml was used to ensure adequate enzyme loading for the remaining experiments.

The current response dependence on environmental temperature was investigated from 10 °C to 45 °C. Fig. 7 shows the current response to 200 mg/dl cholesterol solution vs. ambient temperature tested using a fixed buffer flow rate of 40 μl/min and a sample injection volume of 15 μl. It is evident that the current response is optimized in the temperature ranging from 20 to 30 °C. The response rapidly decreases when the ambient temperature exceeds 30 °C and it also reduces as temperature goes below 20 °C. The results can be explained from the fact that cholesterol enzyme quickly degrades at high temperature and electrochemical mobility and solubility of cholesterol in the solution reduce at low temperature. Thus, room temperature (25 °C) is suitable for cholesterol detection.

3.3. Amperometric detection of cholesterol

Amperometric cholesterol detection was then performed using the optimized detection potential, injection volume, pH of buffer, enzyme concentration and ambient temperature obtained from above studies. Fig. 8 shows amperometric cholesterol sensing in the concentration ranging from 50 to 250 mg/dl with three replicate injections for each concentration. From the plot, the rise time and decay time are estimated to be 3–5 and 40–45 s, respectively. Thus, fast detection with a high throughput of ~60 samples/h has been achieved.

The calibration curve, Fig. 9, is obtained from the peak amplitude of current response pulses over a range of concentration from 0 to 450 mg/dl. It can be seen that linear concentration dependence is obtained in the concentration range between 50 and 400 mg/dl (~1.25 to ~10 mM). The regression equation is given by $y = 0.0512x + 3.69$ ($r^2 = 0.9959$), where y and x are the height of peak current (nA) and cholesterol concentration (mg/dl), respectively. The slope of the equation is corresponding to the linear sensitivity of 0.0512 nA/(mg/dl). In addition, it is seen that the current response begins to level off at concentration higher than 400 mg/dl while it increases with a higher slope at concentration lower than 50 mg/dl. The detection limit (3S/N) is estimated from Fig. 9 to be ~10 mg/dl (~0.25 mM). Thus, the operating range of present system is suitable for clinical diagnostics of cholesterol in blood whose cholesterol concentration for most people lies within the range between 50 and 350 mg/dl.

The linear detection range is comparable to other electrochemical cholesterol sensors based on CNT nanocomposite or SnO_2/ZnO nanostructures (Li et al., 2005; Roy et al., 2006; Yang et al., 2006; Ansari et al., 2009; Solanki et al., 2009; Umar et al., 2009),

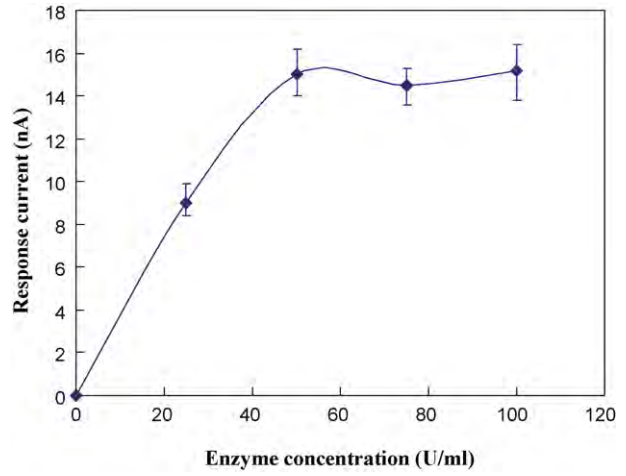

Fig. 6. Effect of cholesterol enzyme concentration on current response to 200 mg/dl cholesterol at 0.4 V vs. Ag reference electrode.

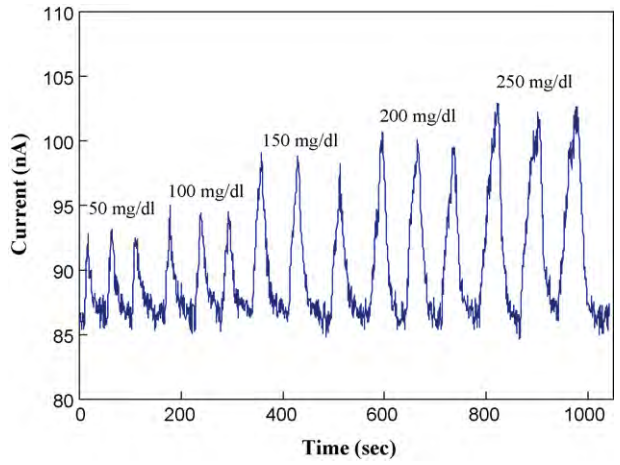

Fig. 8. Flow injection chronoamperometric detection of cholesterol with different cholesterol concentrations at 0.4 V vs. Ag reference electrode.

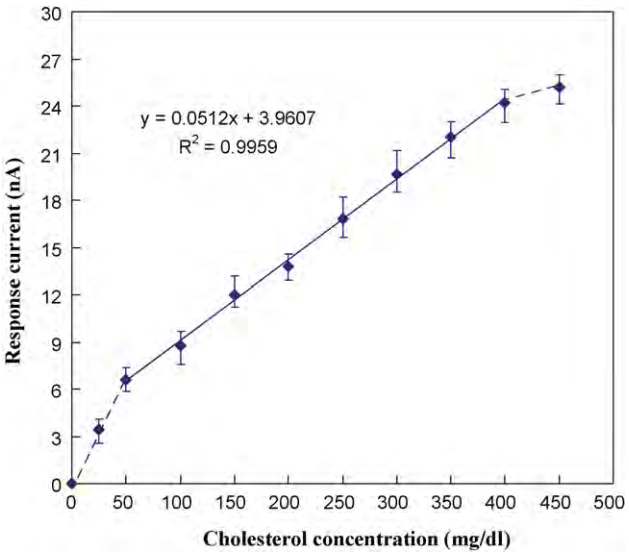

Fig. 9. Calibration curve as a function of cholesterol concentration.

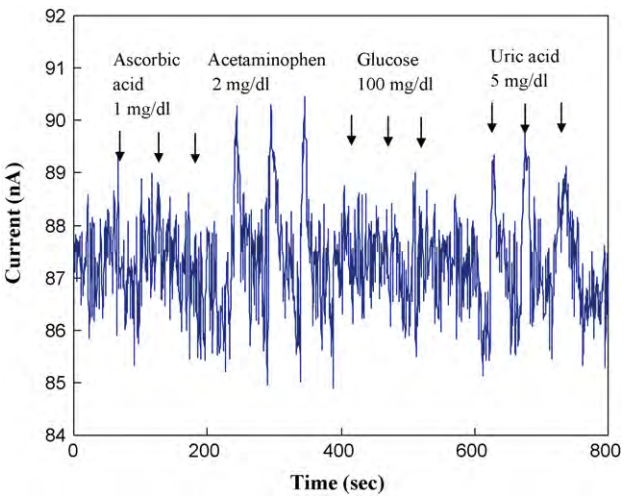

Fig. 10. Interference responses toward ascorbic acid (1 mg/dl), glucose (100 mg/dl), acetaminophen (2 mg/dl) and uric acid (5 mg/dl) at 0.4 V vs. Ag reference electrode.

whose linear regions are varied with high limits in the range of 300–500 mg/dl or 7.5–12.5 mM and with low limits in the range of 5–50 mg/dl or 0.1–1 mM. However, the detection limit is not as low as those in some reports, which are in the range of 0.05–5 mg/dl or 0.001–0.1 mM. The possible causes of relatively poor detection limit include less active enzymes used, less effective enzyme immobilization method and normally lower current sensitivity of micro-flow injection measurement.

It should be noted that this work utilizes dynamic micro-flow injection chronoamperometric detection scheme while other reports employ static/semi-static voltammetric detection methods including conventional chronoamperometry, cyclic voltammetry, square wave voltammetry and differential pulse voltammetry. In the micro-flow injection detection mode, sensors have very limited reaction time with very small sample volume and hence the response can be considerably less compared to other detection methods. Hence, the detection limit (10 mg/dl) and sensitivity (0.0512 nA/mg/dl) of the on-chip CNT sensor can be considered satisfactory and they may be comparable to other reported sensors if detection is made by the same method.

Despite its relatively lower current sensitivity, the proposed cholesterol detection scheme is considered better than several other reported cholesterol systems because of higher speed detection and much lower sample consumption. Real-time cholesterol detection has been achieved with very fast response time (3–5 s), high sample throughput (60 samples/h), very low sample consumption (15 μl) and satisfactory dynamic range (50–400 mg/dl). The resulting performance is attributed to fast, sensitive and stable CNT electrode directly grown on microfluidic chip and effective cholesterol enzyme immobilization using entrapment in PVA matrix. The use of this platform for other bio-sensing can be further optimized for each application by the use of suitable enzymes and immobilization methods to yield desired detection limit and dynamic range.

3.4. Interference and stability study

Specificity is one of the most critical issues for biosensors to be used in real environment. To evaluate specificity of the sensors, interferences by four common electroactive species including ascorbic acid, glucose, acetaminophen and uric acid were tested near their normal concentration level in serum. Fig. 10 demonstrates interference responses of ascorbic acid (1 mg/dl), glucose (100 mg/dl), acetaminophen (2 mg/dl) and uric acid (5 mg/dl). It can be seen that ascorbic acid and glucose give negligible interference signals, while acetaminophen and uric acid produce relatively small interference signal. The interferences from these analytes are satisfactorily low because the working electrode potential was set at a suitably low value of 0.4 V so that specific oxidative reaction by cholesterol oxidase is dominant.

Lastly, long-term stability of the sensor was assessed. The sensors were stored dry at 4 °C and tested every day. It was found that the sensitivity was dropped by 20% after one month due to natural enzyme degradation and loss during operation. No significant CNT removal was observed over the period of study. Thus, the on-chip CNT sensors had a satisfactory life time. The long-term stability of CNT electrode is attributed to the direct growth approach. The directly grown CNTs were robust to erosion under continuous flow of buffer and analyte for several days. Such stability may not be attained from CNTs prepared by paste printing or dielectrophoresis coating methods. Therefore, the present system is promising for clinical diagnostics of cholesterol with high speed real-time detection capability, very low sample consumption, high sensitivity, low interference and good stability.

4. Conclusions

In conclusion, a new cholesterol detection scheme utilizing functionalized CNT electrode on glass based microfluidic ship has successfully been developed by direct growth of CNTs on a glass chip. Fast cholesterol detection with a high throughput of more than 60 samples/h has been achieved. The CNTs based cholesterol sensor has a linear detection range between 50 and 400 mg/dl. In addition, low cross-sensitivity toward glucose, ascorbic acid, acetaminophen and uric acid have been verified. Moreover, the functionalized CNT electrode exhibits a good stability and good reproducibility in a micro-flow injection microfluidic system. The presented system is thus promising for clinical diagnostics of cholesterol with high speed real-time detection capability, very low sample consumption, high sensitivity, low interference and good stability.

Acknowledgements

This work was supported by National Electronics and Computer Technology Center (NECTEC), project no. ME5101, and Thailand

Research Fund (TRF). A.T. would like to acknowledge TRF for career developing fund.

References

Ansari, A.A., Kaushik, A., Solanki, P.R., Malhotra, B.D., 2009. Electroanalysis 21, 965–972.
Ansari, A.A., Kaushik, A., Solanki, P.R., Malhotra, B.D., 2008. Electrochem. Commun. 10, 1246–1249.
Aravamudhan, S., Kumar, A., Mohapatra, S., Bhansali, S., 2007. Biosens. Bioelectron. 23, 2289–2294.
Arya, S.K., Pandey, P., Singh, S.P., Datta, M., Malhotra, B.D., 2007. Analyst 132, 1005–1009.
Arya, S.K., Datta, M., Malhotra, B.D., 2008. Biosens. Bioelectron. 23, 1083–1100.
Becker, H., Locascio, L.E., 2002. Talanta 56, 267–287.
Brahim, S., Narinesingh, D., Elie, A.G., 2002. Biosens. Bioelectron. 17, 973–981.
Castano-Alvarez, M., Fernansez-Abedul, M.T., Costa-Garcia, A., 2006. J. Chromatogr. A 1109, 291–299.
Crevillen, A.G., Pumera, M., Gonzalez, C.M., Escarpa, A., 2009. Lab Chip 9, 346–353.
Dossi, N., Susmel, S., Toniolo, R., Pizzariello, A., Bontempelli, G., 2009. Electrophoresis 30, 3465–3471.
Dossi, N., Toniolo, R., Pizzariwllo, A., Susmel, S., Perennes, F., Bontempelli, G.J., 2007. Electroanal. Chem. 601, 1–7.
Ford, S.M., Kar, B., McWhorter, S., Davies, J., Soper, S.A., Klopf, M., Calderon, G., Saile, V.J., 1998. Microcolumn 10, 413–422.
Guo, M., Chen, J., Li, J., Nie, L., Yao, S., 2004. Electroanalysis 16, 1992–1998.
Huang, J.-E., Hong, X., Li, H.-L., 2003. Carbon 41, 2731–2736.
Karuwan, C., Wisitsoraat, A., Maturos, T., Phokharatkul, D., Sappat, A., Jaruwongrungsee, K., Lomas, T., Tuantranont, A., 2009. Talanta 79, 995–1000.
Kaushik, A., Solanki, P.R., Kaneto, K., Kim, C.G., Ahmad, S., Malhotra, B.D., 2010. Electroanalysis 22, 1045–1055.
Kirgoz, U.A., Timur, S., Odaci, D., Pérez, B., Alegret, S., Merkoçi, A., 2007. Electroanalysis 19, 893–899.
Li, J., Peng, T., Peng, Y., 2003. Electroanalysis 15, 1031–1037.
Li, G., Liao, J.M., Hu, G.Q., Ma, N.Z., Wu, P.J., 2005. Biosens. Bioelectron. 20, 2140–2144.
Li, Y., Bai, H., Liu, Q., Bao, J., Han, M., Dai, Z., 2010. Biosens. Bioelectron. 25, 2356–2360.
Liao, K.-T., Chen, C.-M., Huang, H.-J., Lina, C.-H., 2007. J. Chromatogr. A 1165, 213–218.
Lin, K.-W., Huang, Y.-K., Su, H.-L., Hsieh, Y.-Z., 2008. Anal. Chim. Acta 619, 115–121.
Mansur, H.S., Orefice, R.L., Mansur, A.A.P., 2004. Polymer 45, 7193–7202.
McDonald, J.C., Duffy, D.C., Anderson, J.R., Chiu, D.T., Wu, H., Schueller, O.J.A., Whitesides, G.M., 2000. Electrophoresis 21, 27–40.
Noma, A., Nakayama, K., 1976. Clin. Chem. 22, 336.
Panini, N.V., Messina, G.A., Salinas, E., Fernandez, H., Raba, J., 2008. Biosens. Bioelectron. 20, 2140–2144.
Pozo-Ayuso, D.F., Castano-Alvarez, M., Fernansez-la-Villa, A., Garcia-Granda, M., Fernandez-Abedul, M.T., Costa-Garcia, A., Rodriguez-Garcia, J., 2008. J. Chromatogr. A 1180, 193–202.
Qiaocui, S., Tuzhi, P., Yunu, Z., Yang, C.F., 2005. Electroanalysis 17, 857–861.
Roy, S., Vedala, H., Choi, W., 2006. Nanotechnology 17, S14–S18.
Rwyes, D.R., Iossifidis, D., Auroux, P.A., Manz, A., 2002. Anal. Chem. 74, 2623–2636.
Schoning, M.J., Jacobs, M., Muck, A., Knobbe, D.-T., Wang, J., Chatrathi, M., Spillmamm, S., 2005. Sens. Actuators B 108, 688–694.
Shahrokhian, S., Zare-Mehrjardi, H.R., 2007. Electrochim. Acta 52, 6310–6317.
Solanki, P.R., Kaushik, A., Ansari, A.A., Tiwari, A., Malhotra, B.D., 2009. Sens. Actuators B 137, 727–735.
Sulek, F., Knez, Z., Habulin, M., 2010. Appl. Surf. Sci. 256, 4596–4600.
Umar, A., Rahman, M.M., Al-Hajry, A., Hahn, Y.-B., 2009. Talanta 78, 284–289.
Vidal, J.C., Ruiz, E.G., Castillo, J.R., 2001. Electroanalysis 13, 229–235.
Wisitsoraat, A., Tuantranont, A., Thanachayanont, C., Patthanasettakul, V., Singjai, P., 2006. J. Electroceram. 17, 45–49.
Wisitsoraat, A., Patthanasettakul, V., Tuantranont, A., Mongpraneet, S., 2008. J. Vac. Sci. Technol. B 26, 1757–1760.
Wisitsoraat, A., Karuwan, C., Wong-ek, K., Phokharatkul, D., Phokharatkul, P., Tuantranont, A., 2009. Sensors 9, 8658–8668.
Yang, M., Yang, Y., Qu, F., Lu, Y., Shen, G., Yu, R., 2006. Anal. Chim. Acta 571, 211–217.

View Online / Journal Homepage / Table of Contents for this issue
Dynamic Article Links

Lab on a Chip

Cite this: *Lab Chip*, 2012, **12**, 133

www.rsc.org/loc

PAPER

Enhancement of DNA hybridization under acoustic streaming with three-piezoelectric-transducer system

Thitima Maturos,[a] Tawee Pogfay,[a] Kiattimant Rodaree,[a] Sastra Chaotheing,[b] Apichai Jomphoak,[a] Anurat Wisitsoraat,[a] Nattida Suwanakitti,[b] Chayapat Wongsombat,[b] Kata Jaruwongrungsee,[a] Philip Shaw,[b] Sumalee Kamchonwongpaisan[b] and Adisorn Tuantranont*[a]

Received 4th August 2011, Accepted 30th September 2011
DOI: 10.1039/c1lc20720b

Recently, we have demonstrated that DNA hybridization using acoustic streaming induced by two piezoelectric transducers provides higher DNA hybridization efficiency than the conventional method. In this work, we refine acoustic streaming system for DNA hybridization by inserting an additional piezoelectric transducer and redesigning the locations of the transducers. The Comsol® Multiphysics was used to design and simulate the velocity field generated by the piezoelectric agitation. The simulated velocity vector followed a spiral vortex flow field with an average direction outward from the center of the transducers. These vortices caused the lower signal intensity in the middle of the microarray for the two-piezoelectric disk design. On the contrary, the problem almost disappeared in the three-piezoelectric-disk system. The optimum condition for controlling the piezoelectric was obtained from the dye experiments with different activation settings for the transducers. The best setting was to activate the side disks and middle disk alternatively with 1 second activating time and 3 second non-activating time for both sets of transducers. DNA hybridization using microarrays for the malaria parasite *Plasmodium falciparum* from the optimized process yielded a three-fold enhancement of the signal compared to the conventional method. Moreover, a greater number of spots passed quality control in the optimized device, which could greatly improve biological interpretation of DNA hybridization data.

Introduction

The DNA microarray is one of the most important analysis techniques in molecular biology. This technology is used to measure changes in gene expression levels and to identify patterns of genetic variation *i.e.* single nucleotide polymorphisms (SNPs).[1] In a standard microarray experiment, the sample solution is confined in a microarray hybridization chamber by a cover slip. Inside the chamber, the target DNA diffuses all around the hybridization chamber to hybridize with complementary DNA probes fixed on a solid surface. Without active agitation, the diffusion of macromolecules such as DNA is an extremely slow process owing to the low diffusion constant (D) of DNA, which in water is typically 10^{-6} to 10^{-7} cm^2 s^{-1}, depending on DNA size, concentration and hybridization conditions.[2,3] According to the equation of diffusion length (L): $L = (Dt)^{0.5}$, the diffusion time (t) for DNA to travel over a distance of a few mm is more than 24 h.[4] Practically, diffusion-limited DNA hybridization takes 6–24 h to achieve sufficient hybridization signals and uniformity of signals across an array.[5]

Accordingly, a large number of researchers have been seeking alternative methods to enhance the hybridization, for example surface acoustic wave (SAW) based microagitation,[6] cavitational microstreaming,[7] fluid circulation and mixing,[1,2,8] rotating the hybridization chamber[9,10] and other forms of electrical enhancement.[11,12] All of these methods are based on the use of mechanical or electrical force to increase the transportation rate of the DNA molecules. Some of these methods require complicated fabrication processes, expensive devices, or modification of the DNA microarray. Acoustic streaming is another effective mixing technique applicable to microarrays. In this technique, an ultrasound wave passes through a liquid medium and transfers the momentum to the test fluid, generating a steady circular flow occurring in a high-intensity non-linear acoustic field.[13] The spatial attenuation of a wave in free space and the friction between a medium and a vibrating object are the two key mechanisms for acoustic streaming induction.[14] Another non-linear phenomenon always considered along with acoustic streaming, is the acoustic radiation force. Acoustic radiation

[a]*Nanoelectronics and MEMS laboratory, National Electronics and Computer Technology Center (NECTEC), 112 Paholyothin Rd., Klong 1, Klong Luang, Pathumthani, 12120, Thailand. E-mail: adisorn.tuantranont@nectec.or.th; Fax: +66-2-564-6756; Tel: +66-2-564-6900 ext. 2111*
[b]*National Center for Genetic Engineering and Biotechnology (BIOTEC), 113 Paholyothin Rd., Klong 1, Klong Luang, Pathumthani, 12120, Thailand; Fax: +66-2-564-6707; Tel: +66-2-564-6700*

force moves a suspending particle toward or away from acoustic pressure nodes while acoustic streaming induces the flow of the entire fluid.[13] The extent to which a particle is affected by acoustic radiation force or acoustic streaming depends on the size of the particle. Larger particles will experience a higher degree of acoustic radiation force and a lower level of acoustic streaming, respectively.[15] Acoustic streaming has been used in many applications, for example clinical analysis,[16] enhancement of heat and mass transfer[17] and fluid mixing.[3,18] It is one of the most practical fluid mixing techniques for DNA hybridization since there is no need for an external pumping unit or complicated mechanical parts for moving the microarray slide and coverslip. However, fabrication and integration of the acoustic streaming source for microarrays typically requires modification to the microarrays and coverslip,[19–21] which is impractical since DNA microarrays are typically obtained from commercial sources available in standard formats only.

Recently, we proposed a simple and low cost device for DNA hybridization based on acoustic streaming induced by two piezoelectric transducers with a coupling fluid.[22] Each piezoelectric disk, placed directly beneath each hybridization chamber, generates acoustic waves that are effectively transferred to microarrays *via* a coupling fluid. The DNA targets were observed to move in both vertical and horizontal directions under the influence of acoustic streaming facilitating hybridization with their complementary DNA probes. This scheme requires no modification of the microarray or coverslip and provides better DNA hybridization efficiency and speed compared to the conventional method of static hybridization. However, the efficiency of DNA hybridization over the whole array area is still sub-optimal. In this work, we refine the acoustic streaming system for DNA hybridization by inserting an additional piezoelectric transducer (PZT) and redesigning the locations of the transducers. The Comsol® Multiphysics software is used to design and simulate the velocity field generated by the piezoelectric agitation. DNA microarray hybridization experiments were performed using *Plasmodium falciparum* microarrays to verify the performance of the new device.

Experimental section

Design and fabrication

The schematic of the DNA hybridization device is shown in Fig.1. The device consists of three PZTs attached in aluminium chambers. Another aluminium plate, which could be screwed to the chamber, was used as a lid. An o-ring was used to provide a tight seal between chambers and the cover plate. PZTs with a diameter of 1.75 mm were activated at a resonant frequency of 1.67 MHz and operating voltage of 24 V_{rms}. The 0.8 mm deep circular wells located on top of the PZTs and two rectangular wells at both ends of the chamber were used for holding a coupling fluid and a humidity control solution, respectively. 3xSSC solution was used as a coupling fluid as well as a humidity control solution. The reasons for choosing 3xSSC solution as a coupling fluid were that it is closely matched in acoustic impedance (z) with the silica glass, it is low in heat transfer and it is non-contaminant to the hybridization process.[22] The 3-PZT design was proposed in order to improve the non-uniformity

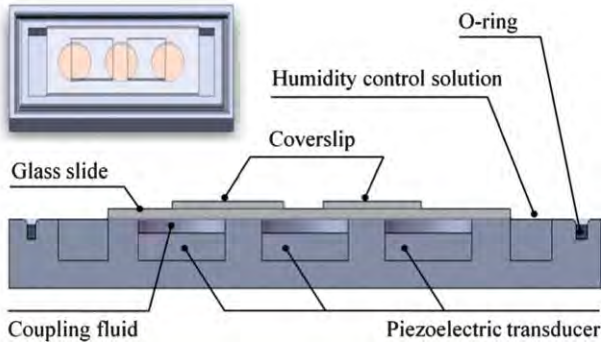

Fig. 1 Schematic showing a side view and top view of dynamic hybridization device in which DNA microarrays are placed inside the hybridization chamber above the piezoelectric ultra sonic transducers and coupling liquid. An O-ring rubber is used to provide a tight seal.

problem found from our previous design, in which microarrays were placed on top of two PZTs. It was found that signal intensity in the middle of the hybridization chamber tended to be low compared with other regions, which may have been a result of an outward flow of acoustic wave from the center of the microarray. The new device was designed to have PZTs interposed between microarrays to provide alternate agitations between both sides of the hybridization chamber and thus significantly enhance the movement of target DNA. Moreover, the new design would allow us to operate with different microarray shapes *i.e.*, the short microarray (17.5 × 19.5 mm^2) and a long microarray (17.5 × 45 mm^2). The optimum signal for each microarray could be obtained by controlling each PZT independently. It should also be noted that no more than three-piezoelectric-transducers can be used in this system because of physical constraints including the sizes of the piezoelectric disk, microarray, glass slide and chamber.

Finite element simulation

The microagitation system was designed and simulated using Comsol® Multiphysics (COMSOL Inc., Burlington, MA), a finite element method (FEM) simulation software. The 3D model for numerical simulations was constructed according to the real device dimensions. The finite elements of the structure were then built using a tetragonal mesh with ultra fine precision. The generation and propagation of acoustic waves in the structure were simulated using piezoelectric and pressure acoustic modules in Comsol® Multiphysics. The first set of governing equations used in the piezoelectric module are electromechanical equations of motion with stress-induced piezoelectric effect[23]:

$$\begin{bmatrix} \mathbf{M} & \mathbf{0} \\ \mathbf{0} & \mathbf{0} \end{bmatrix} \begin{bmatrix} \ddot{\mathbf{u}} \\ \ddot{\mathbf{v}} \end{bmatrix} + \begin{bmatrix} \mathbf{C}_m & \mathbf{0} \\ \mathbf{0} & \mathbf{0} \end{bmatrix} \begin{bmatrix} \dot{\mathbf{u}} \\ \dot{\mathbf{v}} \end{bmatrix} + \begin{bmatrix} \mathbf{K}_m & \mathbf{K}_{me} \\ \mathbf{K}_{me}^T & \mathbf{K}_e \end{bmatrix} \begin{bmatrix} \mathbf{u} \\ \mathbf{v} \end{bmatrix} = \begin{bmatrix} \mathbf{F} \\ \mathbf{L} \end{bmatrix} \quad (1)$$

$$\mathbf{T} = \mathbf{c}_E\mathbf{S} - \mathbf{e}^T\mathbf{E} \quad (2)$$

$$\mathbf{D} = \mathbf{e}\mathbf{S} + \boldsymbol{\varepsilon}_s\mathbf{E} \quad (3)$$

where $\mathbf{M}$, $\mathbf{C}_m$, $\mathbf{K}_m$, $\mathbf{K}_{me}$, $\mathbf{K}_e$, $\mathbf{u}$, $\mathbf{v}$, $\mathbf{F}$ and $\mathbf{L}$ were mass matrix, damping matrix, dielectric conductively matrix, piezoelectric

coupling matrix, stiffness matrix, spatial displacement vector, electric displacement vector, structural force vector and nodal charge vector, respectively. In eqn (2) and (3) **T**, **S** and **E** are stress, strain and electric field vectors respectively, while **e**, $\mathbf{c}_E$ and $\boldsymbol{\varepsilon}_s$ are anisotropic elastic modulus, piezoelectric constant and dielectric constant matrices, respectively. The electric potential boundary conditions applied between piezoelectric electrodes are 1.67 MHz 130 V_{rms} sinusoidal waves. The Comsol® program solves the equations in three dimensions and produces the solution of acoustic wave from displacement fields, which is coupled to the pressure acoustic modules where the propagation of acoustic wave is determined by solving Helmholtz's acoustic wave equation[15,24]:

$$\nabla\cdot(-(1/\rho_0)(\nabla p - q)) - (\omega^2/c_s^2 + \lambda^2)p/\rho_0 = Q,\ \lambda = -ik_N \qquad (4)$$

where p, ρ_0, ω, c_s, Q, q, λ and k_N are acoustic pressure wave, density of acoustic medium, angular frequency, acoustic velocity, monopole source, dipole source, eigenfrequency and normal wave number, respectively. Monopole and dipole source are absent in this case. The mechanical boundary conditions are that all surface of the device are free boundary while the side and top walls of coupling fluid chambers are hard-sound boundary where normal velocity component vanished. The COMSOL eigenvalue solver is used to determine the acoustic frequency response and acoustic wave velocity field. The acoustic simulation of the device with three-PZT agitation was made and compared to that from the previous design that contained only two PZTs.

Optimization of controlling signal

Since dramatic heat flux was generated and could denature DNA during PZT activation, transducers could not operate continuously. Thus, PZTs must be controlled to minimize heat as well as bubble generation, but maximize overall fluidic movement. For the control experiment, the transducers were turned on and off using a square wave signal and tested in three different modes. First, the side disks and the middle disk were activated alternately. Secondly, all disks were activated simultaneously and lastly each disk was activated alternately. Fluidic dye was added into hybridization chambers to observe lateral fluidic movement as a result of agitation. The on and off times for activating the disks were also varied to find an optimum condition. The optimum controlling signal that allowed the fluidic dye to flow all over the hybridization chamber rapidly, homogeneously and coldly are used in the hybridization experiment.

DNA hybridization experiment

The hybridization experiments were then performed using two- and three-piezo hybridization devices and compared with the conventional static method. The DNA microarrays were fabricated on polylysine-coated glass slides using a new generation ultrafast, linear servo driven DeRisi microarrayer, controlled by ArrayMaker software (http://derisilab.ucsf.edu/microarray/software.html). The DNA microarray was printed on a glass substrate with a total area of 17.5 × 19.5 mm^2. The microarray contained 8088 features with a printed long oligonucleotide probe (70 bases in length). The probes covered the malaria parasite *Plasmodium falciparum* genome. The target DNAs were cDNAs, which were transcribed from total RNA.

There were two different cDNA samples, one labeled with Cy3 dye and the other labeled with Cy5 dye (Amersham Biosciences) as described previously.[25] The experiments were conducted with the same cDNA quantity (5 pmol) and hybridized for 16 h at 42 °C. After hybridization, the arrays were washed, dried and stored in a cool dark place before analysis. All scanning was done on the same day and all scans were done using the same laser power and PMT gain settings (100%, Cy5 PMT = 560 V, and Cy3 PMT = 490 V respectively). Microarray scanning and image analysis was done on a GenePix400B scanner and spot intensities were quantified using GenePix Pro 6.0 Software (Axon Instrument, Inc). Filtering to distinguish good/effective spots was done using the signal-to-noise ratio (SNR) ≥ 3 reported by GenePixPro, which follows the recommendation made by Yatskou *et al.*[26] for DNA microarray data. Kernel density plots and subarray boxplots were carried out using the R interpreter software.

Results and discussion

Flow field in hybridization chamber

The velocity vector fields from acoustic simulation of the device with 2-PZT and 3-PZT agitation systems are illustrated in Fig. 2. The results of the 2-PZT agitation system are demonstrated when only the left PZT is activated while the results of the 3-PZT agitation system are demonstrated in the mode in which two side PZTs are activated and the center PZT is off. These settings represent typical conditions used in experiments. Comparing the top view of the velocity vector field of 2-PZT and 3-PZT systems (Fig. 2A–B), it is evident that the velocity vector field on the square hybridization area of the 2-PZT system is considerably weaker than that of the 3-PZT system. Thus, agitation by the 3-PZT system is much more effective. From the enlarged 3D view of the velocity vector field of the 2-PZT and 3-PZT systems (Fig. 2C–D), a spiraling vortex 3D streaming flow with a source located approximately in the middle of the PZT is formed in both cases. The spiral flow is in the direction outward from the center of the PZT. For the 2-PZT case, each PZT is concentric with the microarray. Thus, DNA particles will move very slowly (almost stationary) around the center of microarray, however there is much more movement toward the edges. The results can explain our previous experimental observation that the hybridization intensity on the edge of microarrays was often observed to be much greater than on the central region. In the 3-PZT design, each microarray is interposed between two PZTs. Hence, each edge of a microarray can receive the outward spiral flow with strong velocity field from the PZT on each side as shown in Fig. 2D. However, it should be noted that if the spiral fields from PZTs on both sides appear simultaneously, undesirable standing wave will occur from the simulation of two opposing waves. Thus, PZTs on either side should not be activated concurrently. Therefore, the 3-PZT design with alternate PZT activation should be able to circumvent the problem of low hybridization intensity at the microarray center in 2-PZT design.

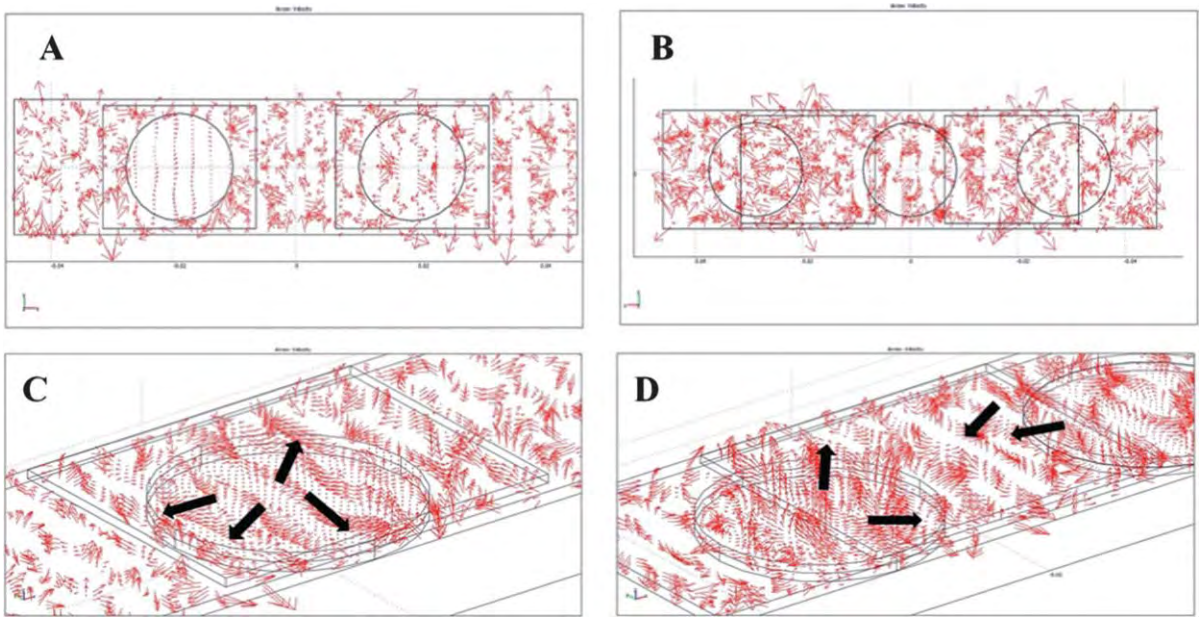

Fig. 2 Top view of velocity vector field of (A) the 2-PZT system when the left PZT is activated and (B) the 3-PZT system when two side PZTs are activated. The corresponding 3D views of the velocity vector field of the (C) 2-PZT and (D) 3-PZT systems.

Operating signal optimization

From the control experiments, three PZTs were initially tested in three different modes without non-activating time between consecutive transducer activations. It was found that the fluidic dye could cover the entire hybridization chamber within 5 min when the side disks and the middle disk were alternately activated. However, similar coverage would take 10 min and 14 min when operating all three PZTs simultaneously and activating each PZT alternately, respectively. Thus, the results agree with the prediction from the simulation that a standing wave would occur and deter fluid mixing when operating all PZTs simultaneously. Therefore, the best activation mode is confirmed to be operating the middle and side PZTs alternately. However, it was found that excessive heat was generated due to the lack of non-activating time between consecutive transducer activations. Thus, non-activating time was added and on-off activating signals were varied to optimize fluidic movement, total operating time and heat generation. Lower heat generation could be observed with less bubble generation in the fluid after adding non-activating time. The optimum activating and non-activating times were found to be 1 and 3 s, respectively. The condition was proven to be suitable in terms of heat reduction and overall fluid movement. The optimum agitation by 3-PZT system allowed the fluidic dye to fill the entire chamber as illustrated in Fig. 3B within 15 min, while it took more than 30 min for the dye to cover half of the chamber as shown in Fig. 3A for the static case (all PZTs off).

Enhancement of microarray hybridization efficiency

The hybridization efficiency of our device was compared with the conventional static hybridization method. The hybridization experiments were performed on a microarray with corresponding biological cDNA samples. The fluorescent scanned images of microarrays hybridized with or without piezoelectric agitation, are shown in Fig. 4. The signals are consistent across both arrays, although the signal overall for the piezoelectric hybridization appears stronger relative to conventional hybridization. For microarray data analysis, spot quality control is a crucial part to

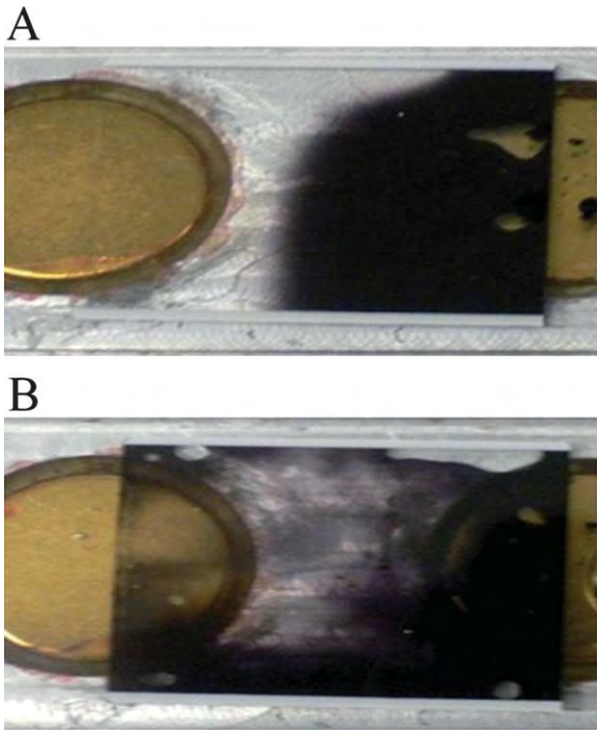

Fig. 3 Photographs of dye solution mixing in the hybridization microchamber (A) without acoustic streaming (PZT off) and (B) with the PZT agitation at 1.67 MHz and 24 Vrms.

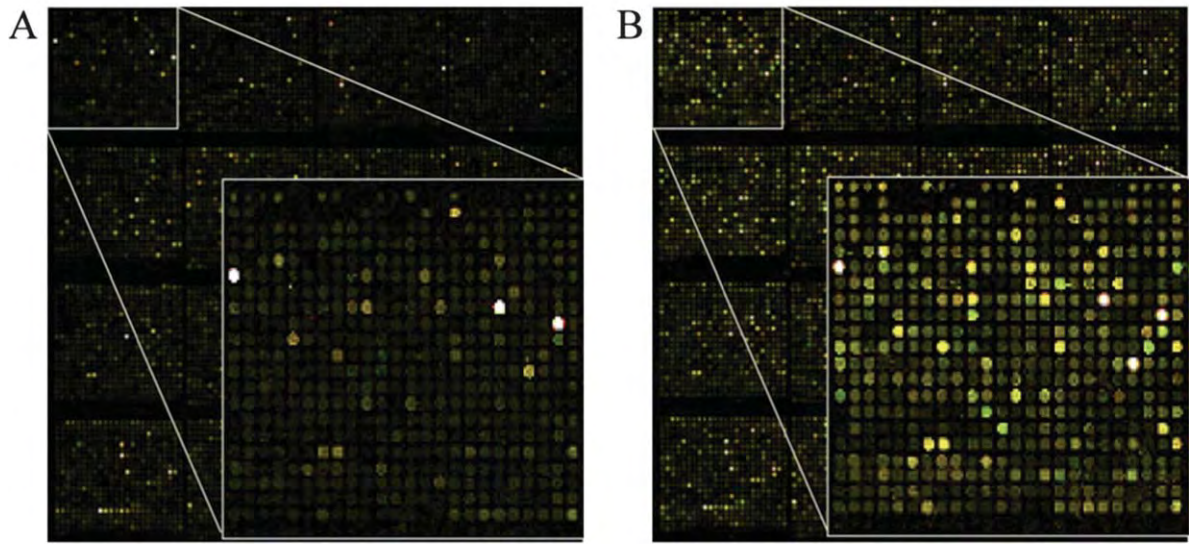

Fig. 4 Microarray scan pictures of *P. falciparum* DNA microarrays with (A) 16 h static hybridization, and (B) 16 h 3-PZT dynamic hybridization.

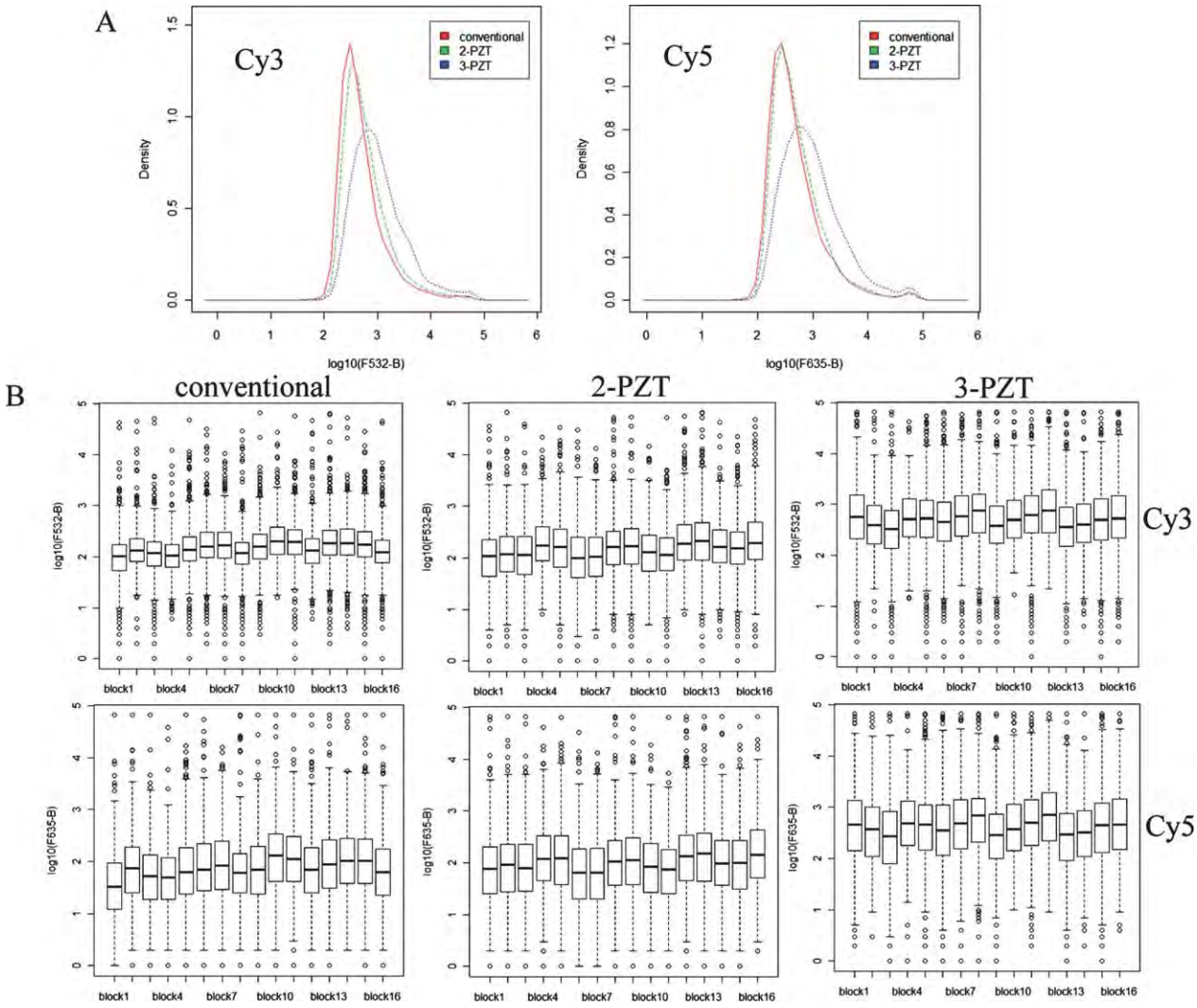

Fig. 5 (A) Kernel density plots (normalized density *vs.* background-corrected fluorescence intensity (log scale) for the spots in Cy3 (532 nm) and Cy5 (635 nm) channels) obtained from hybridization experiments using conventional, 2-PZT and 3-PZT systems and (B) corresponding subarray box plots (background-corrected fluorescence intensity (log scale) distribution for 16 subarrays). Thick line in each box represents median intensity.

distinguish between good/effective spots from bad ones that may represent biologically irrelevant noise. We found that more spots pass filtering for agitated 2-PZT and 3-PZT relative to conventional hybridization (2720, 5560, and 2414 spots respectively). Thus, our 3-PZT system can significantly increase the number of effective spots over the previous 2-PZT system and static hybridization. As a result, our new agitation system could increase the detection sensitivity for DNA targets that may have produced low hybridization signals (due to their low expression level) but were biologically relevant. The power of discovering more effective spots would be extremely beneficial in many kinds of transcriptomic profiling studies because it would produce better microarray interpretation. The greater number of good spots for agitated hybridization cover a broader range of signal intensities, especially for the 3-PZT hybridization, as shown by the kernel density distribution plots for the Cy3 and Cy5 channels (Fig. 5A).

In order to demonstrate that the hydridization efficiency of the 3-PZT is consistent across the array, the fluorescent signals within each of the 16 subarrays were compared. The boxplots of fluorescent intensity shown in Fig. 5B indicate that the ranges of intensities within each subarray are comparable, with no noticeable bias in different regions of the array. A rigorous statistical analysis was not performed though, since the subarrays contain different probes corresponding to genes expressed at different levels. Moreover, the printing of probes on the array is not random *e.g.* the bottom row of each subarray is mostly empty. Consistent hybridization across the array also requires careful application of the labeled DNA solution and coverslip, which can be a major source of operator error. To overcome this problem, semi-automated delivery systems could be incorporated into the 3-PZT device, such as used in the MAUI commercial system (BioMicro systems USA).

Conclusions

In conclusion, we have developed a new three-PZT design for a low-cost dynamic acoustic streaming-based DNA hybridization system. The new acoustic streaming design is modified from the previously developed 2-PZT system by inserting an additional piezoelectric transducer and redesigning the locations of the transducers. The design is assisted by acoustic simulations using Comsol® Multiphysics. Our static *versus* dynamic hybridization comparison under 'real' microarray experimental parameters demonstrated that the newly designed dynamic hybridization system provides significantly higher average fluorescent signal intensities in both Cy3 and Cy5 channels than the conventional static hybridization and the previous 2-PZT design. This allows more effective spots to be included in the subsequent microarray data analysis, and potentially greater power to detect biologically significant signals, especially those in the lower range.

Acknowledgements

We would like to thank Drs Joseph Derisi and Jennifer Shock at the University of San Francisco for providing the oligo-set, training and facilities for the production of DNA microarray slides, through generous support from the Howard Hughes Medical Institute (HHMI, USA). S.K. is an international research scholar of HHMI, USA. A.T. expresses his great gratitude to the Thailand Research Fund (RSA5380005) for a research career development grant.

Notes and references

1 H. H. Lee, J. Smoot, Z. McMurray, D. A. Stahl and P. Yager, *Lab Chip*, 2006, **6**, 1163–1170.
2 M. K. McQuain, K. Seale, J. Peek, T. S. Fisher, S. Levy, M. A. Stremler and F. R. Haselton, *Anal. Biochem.*, 2004, **325**, 215–226.
3 R. H. Liu, J. Yang, M. Z. Pindera, M. Athavale and P. Grodzinski, *Lab Chip*, 2002, **2**, 151–157.
4 J.-M. Hertzsch, R. Sturman and S. Wiggins, *Small*, 2007, **3**, 202–218.
5 M. Schena, *Microarray Biochip Technology*, Eaton Publishing Company, California, 2000.
6 A. Toegl, R. Kirchner, C. Gauer and A. Wixforth, *J Biomol Tech.*, 2003, **14**, 197–204.
7 R. H. Liu, R. Lenigk, R. L. Druyor-Sanchez, J. Yang and P. Grodzinski, *Anal. Chem.*, 2003, **75**, 1911–1917.
8 P. K. Yuen, G. Li, Y. Bao and U. R. Muller, *Lab Chip*, 2003, **3**, 46–50.
9 J. Vanderhoeven, K. Pappaert, B. Dutta, P. Van Hummelen and G. Desmet, *Anal. Chem.*, 2005, **77**, 4474–4480.
10 M. A. Bynum and G. B. Gordon, *Anal. Chem.*, 2004, **76**, 7039–7044.
11 C. Gurtner, E. Tu, N. Jamshidi, R. W. Haigis, T. J. Onofrey, C. F. Edman, R. Sosnowski, B. Wallace and M. J. Heller, *Electrophoresis*, 2002, **23**, 1543–1550.
12 C. Chii-Chang, K. Wei-Chu, C. Sung-Kay and T. Chi-Meng, *Enhancement of DNA hybridization efficiency using photovoltaic effect*, 2003.
13 T. Uchida, T. Suzuki and S. Shiokawa, *Investigation of acoustic streaming excited by surface acoustic waves*, 1995.
14 C. P. Lee and T. G. Wang, *Outer acoustic streaming*, ASA, 1990.
15 S. M. Hagsater, T. G. Jensen, H. Bruus and J. P. Kutter, *Lab Chip*, 2007, **7**, 1336–1344.
16 X. Shi, R. W. Martin, S. Vaezy and L. A. Crum, *J. Acoust. Soc. Am.*, 2002, **111**, 1110–1121.
17 E. H. Trinh and J. L. Robey, *Experimental study of streaming flows associated with ultrasonic levitators*, AIP, 1994.
18 C. Suri, K. Takenaka, H. Yanagida, Y. Kojima and K. Koyama, *Ultrasonics*, 2002, **40**, 393–396.
19 Z. Guttenberg, H. Muller, H. Habermuller, A. Geisbauer, J. Pipper, J. Felbel, M. Kielpinski, J. Scriba and A. Wixforth, *Lab Chip*, 2005, **5**, 308–317.
20 A. Wixforth, C. Strobl, C. Gauer, A. Toegl, J. Scriba and Z. v. Guttenberg, *Anal. Bioanal. Chem.*, 2004, **379**, 982–991.
21 Z. Pan, Y. Li, D. Zhou, J. Tang, M. Zhang, P. Xiao and Z. Lu, *Anal. Biochem.*, 2008, **376**, 280–282.
22 K. Rodaree, T. Maturos, S. Chaotheing, T. Pogfay, N. Suwanakitti, C. Wongsombat, K. Jaruwongrungsee, A. Wisitsoraat, S. Kamchonwongpaisan, T. Lomas and A. Tuantranont, *Lab Chip*, 2011, **11**, 1059–1064.
23 F. Lu, H. P. Lee, P. Lu and S. P. Lim, *Sens. Actuators, A*, 2005, **119**, 90–99.
24 S. Mohamady, R. K. Raja Ahmad, A. Montazeri, R. Zahari and N. A. Abdul Jalil, *Advances in Acoustics and Vibration*, 2009, **2009**, 1–10.
25 Z. Bozdech, J. Zhu, M. Joachimiak, F. Cohen, B. Pulliam and J. DeRisi, *GenomeBiology*, 2003, **4**, R9.
26 M. Yatskou, E. Novikov, G. Vetter, A. Muller, E. Barillot, L. Vallar and E. Friederich, *BMC Res. Notes*, 2008, **1**, 80.

Analytica Chimica Acta 687 (2011) 114–128

Contents lists available at ScienceDirect

Analytica Chimica Acta

journal homepage: www.elsevier.com/locate/aca

Review

A review of monolithic multichannel quartz crystal microbalance: A review

Adisorn Tuantranont*, Anurat Wisitsora-at, Pornpimol Sritongkham, Kata Jaruwongrungsee

Nanoelectronics and MEMS Laboratory, National Electronics and Computer Technology Center, Pathumthani, Thailand

ARTICLE INFO

Article history:
Received 8 October 2010
Received in revised form
13 December 2010
Accepted 14 December 2010
Available online 21 December 2010

Keywords:
Monolithic multichannel quartz crystal microbalance
QCM array
Sensor array

ABSTRACT

Monolithic multichannel quartz crystal microbalance (MQCM) is an emerging technology for advanced sensing and measurement applications. In this report, a comprehensive review of MQCM technology is presented. Firstly, basic MQCM's design, simulation and characterization with emphasis on acoustic interference are described. Next, various MQCM schemes to minimize interference and enhance sensitivity of conventional MQCM devices based on modification of quartz substrate structure are digested. These include mesa, convex and *x*-axis inversion structures. Three important MQCM sensing platforms and their application areas are then discussed. These comprise MQCM as a static multichannel detector, series MQCM as a multichannel detector for the flow injection analysis and multi-frequency QCM for multi-sensitivity/multi-dynamic range detection. Finally, potential MQCM applications including electronic noses, bio-sensor arrays, and photocatatalytic measurement are illustrated and prospective MQCM applications including electronic tongues and electrochemical measurement are suggested.

Adisorn Tuantranont received the B.S. degree in electrical engineering from King Mongkut's Institute of Technology Ladkrabang, Thailand, in 1995, and the M.S. and Ph.D. degrees in electrical engineering from the University of Colorado at Boulder in 2001. Since 2001, he has been the director of the Nanoelectronics and MEMS Laboratory, National Electronic and Computer Technology Center (NECTEC), Pathumthani, Thailand. His research interests are in the area of micro electro-mechanical systems (MEMS), nanoelectronics, lab-on-a-chip technology and printed electronics. He has authored more than 50 refereed journals, 150 proceedings, and holds five patents. He also received the Young Technologist Award in 2004 from the Foundation for the Promotion of Science and Technology under the patronage of H. M. the King, Thailand.

Anurat Wisitsora-at received his Ph.D., M.S. degrees from Vanderbilt University, TN, U.S.A., and B. Eng. degree in electrical engineering from Chulalongkorn University, Bangkok, Thailand in 2002, 1997, and 1993, respectively. His research interests include microelectronic fabrication, semiconductor devices, electronic and optical thin film coating, sensors, and micro electromechanical systems (MEMS).

Pornpimol Sritongkham received her Ph.D. in electroanalytical chemistry from Cranfield University (United Kingdom) in 2002. Her current research is focused on the surface modification of QCM- and electrochemical biosensors and on the development of development of novel diagnostic devices.

Kata Jaruwongrungsee received the B. Eng. and M. Eng. degree in electronics engineering from King Mongkut's Institute of Technology Ladkrabang (KMITL), Thailand, in 2003 and 2005 respectively. Since 2006, he has been with the Nanoelectronics and MEMS Laboratory, National Electronics and Computer Technology Center (NECTEC), Thailand, as an assistant researcher. Presently, he is also doing his Ph.D. on electronics engineering at KMITL. His research is mainly focused on QCM based gas sensors and biosensors.

1. Introduction

Quartz crystal microbalance (QCM) is a thickness-shear mode bulk acoustic wave transducer that has been widely employed for physical, chemical and biological sensing applications [1–6]. QCM

* Corresponding author. Tel.: +662 564 6900x2111; fax: +662 564 6756.
E-mail address: adisorn.tuantranont@nectec.or.th (A. Tuantranont).

0003-2670/$ – see front matter © 2010 Elsevier B.V. All rights reserved.
doi:10.1016/j.aca.2010.12.022

devices derive from piezoelectric quartz crystal resonators that resonate electromechanically in a thickness-shear mode (TSM). Owing to piezoelectric effects, the resonant properties of crystal can be influenced by external physical loading, which may be classified into two main types, gravimetric and viscoelastic loading. In the first case, gravimetric force due to mass rigidly deposited on the crystal surface is balanced by a force originating from the shear gradient inside the crystal, leading to the resonance frequency shift (Δf_g), which is governed by Sauerbrey's equation [7,8]:

$$\Delta f_g = -\frac{2f_0^2}{\sqrt{\rho_q \mu_q}} \frac{\Delta M}{A} \quad (1)$$

$$f_0 = \frac{v}{2t_q} = \frac{\sqrt{(\mu_q/\rho_q)}}{2t_q} \quad (2)$$

where f_0 is the fundamental resonance frequency, ΔM is the mass deposited on QCM surface, A is the active electrode area, v is the acoustic wave velocity, ρ_q is the density of crystal (2.648 g cm^{-3} for quartz), μ_q is the shear modulus of the cut face (2.947×10^{11} g cm^{-1} s^2 for AT-cut quartz) and t_q is the crystal thickness. With this loading effect, QCM has been routinely used for thickness monitoring in physical vapor deposition processes.

For the viscoelastic loading, resonance frequency is changed due to acoustic-fluid damping interaction when QCM operates in viscoelastic medium such as liquid [9]. Unlike gravimetric loading, there are large changes of dissipation factor and resonant resistance due to energy losses of shear wave that travels through non-rigidly adsorbed layers [10–13]. The viscoselastic resonance frequency shift (Δf_v), dissipation factor change (ΔD) and resonant resistance change (ΔR) are given by:

$$\Delta f_v = -f_0^{3/2} \sqrt{\frac{\eta_L \rho_L}{\pi \mu_q \rho_q}} \quad (3)$$

$$\Delta D = 2f_0^{1/2} \sqrt{\frac{\eta_L \rho_L}{\pi \mu_q \rho_q}} \quad (4)$$

$$\Delta R = \frac{(2\pi \eta_L \rho_L f_0)^{1/2} A}{k^2} \quad (5)$$

where η_L, ρ_L and k are viscosity, density and electromechanical coupling factor of the liquid medium, respectively. Both dissipation factor and resonant resistance can be directly measured experimentally. The combined measurements of frequency shift and changes in the dissipation factor and resonant resistance have been termed, *QCM-D* and *QCM-R*, respectively [14]. With the combined mass and viscosity–density effects, QCM can be applied for bio/chemical sensing by coating with a chemically or biologically sensitive film to sense very small amount of adsorbed gases such as volatile organic compounds (VOCs) [15,16] and environmental pollutants [17–19] and liquid phase biochemicals. QCM/QCM-D evolves a solution measurement capability in analytical chemistry and electrochemistry applications due to wide detection range capability and very broad measurement applicability. Moreover, *electrochemical quartz crystal microbalance* (*EQCM*) variant, in which QCM is employed as a working electrochemical electrode, allows advanced electrochemical studies. Great amount of work relating to QCM/QCM-D/EQCM has been summarized in a number of review articles, which go over the utilization of QCM in analytical electrochemistry [20–22], QCM application areas in biosensors [23–29], drug discovery [6,30] and complex biopolymeric/biomimetic/biomolecular systems [1,4].

The main advantages of QCM in sensing fields include high sensitivity, high stability, fast response and low cost. In addition, it provides label-free detection capability for bio-sensing applications. However, QCM faces a major technical disadvantage of substantial characteristic dependence on environmental parameters particularly temperature. The problem can be partially alleviated by using AT-cut QCM surface (35.25° with respect to z-axis) because it has relatively low temperature coefficient compared to other well-characterized quartz crystal cuts [31]. Nevertheless, its performance is still not satisfactory for many sensing applications with largely varied environmental conditions. The environmental effects can be more effectively minimized by a dual QCM scheme [32–35], in which reference and sensing QCMs are employed. Both QCMs should have almost identical characteristic and present in the same environmental condition but reference QCM is prevented from sensing target species by the absence of sensing layer. The influence of environmental factors can be nullified out by taking the difference between them. In general, this scheme may be implemented in two ways. The first mean is to use a simple combination of two independent QCMs [32–35]. This method is found not to be very successful because QCMs made on different substrates can hardly be identical due to variation of crystal production. The QCM mismatch problem can be effectively eliminated by employing dual-QCM resonators on a single quartz substrate since two QCMs can be made highly identical [35]. However, the approach gives rise serious interference problems because acoustic wave induced by one QCM can interfere with the wave generated from the nearby QCM [36]. In addition, mass or stress loading on one QCM will induce spurious frequency shift on the other. The problems become particularly serious for two closely spaced identical QCMs [37].

Multiple QCM array system has been developed following the dual QCM scheme for advanced physical, chemical and biological sensing with environmental compensation [38]. In this system, one QCM is used as a reference and other QCMs are coated with different sensing layers. Multiple QCM array systems implemented by a simple combination of several independent QCMs are considered not suitable for general applications not only due to QCM mismatch problem but also bulkiness. Multiple microbalances on a single quartz substrate, commonly referred to as *monolithic multichannel quartz crystal microbalance* (*MQCM*), are thus considered highly promising. Moreover, the development of MQCMs leads to miniaturization of QCM devices because the size and spacing between QCMs are necessarily small as the array size increases. QCM miniaturization leads to additional benefits including lower cost, less sample/reagent consumption, faster sensing response and shorter diagnostic time [39]. Furthermore, QCMs in an array can be designed to have varying sensitivity, selectivity and dynamic range. Therefore, MQCM will be a versatile sensor platform with high performance and wide functionality. However, MQCM technology faces challenging strong acoustic interference problems that cannot easily be solved. It not only affects MQCM performance but also constrains the miniaturization.

In this report, a comprehensive review of MQCM technology is presented. Firstly, basic MQCM's design, simulation and characterization with emphasis on acoustic interference are described. Next, various MQCM schemes to solve the problems of conventional MQCM devices based on modification of quartz substrate structure are digested. These include mesa, convex and x-axis inversion structures. Three important MQCM sensing platforms and their application areas are then discussed. These cover MQCM as a static multichannel detector, series MQCM as a multichannel detector for the flow injection analysis, and multifrequency MQCM for multi-sensitivity/multi-dynamic range detection. Finally, potential and prospective applications for MQCM are illustrated.

2. Conventional MQCM

A conventional MQCM utilizes a few hundreds micron thick AT-cut quartz crystal plate with an array of electrode pairs deposited

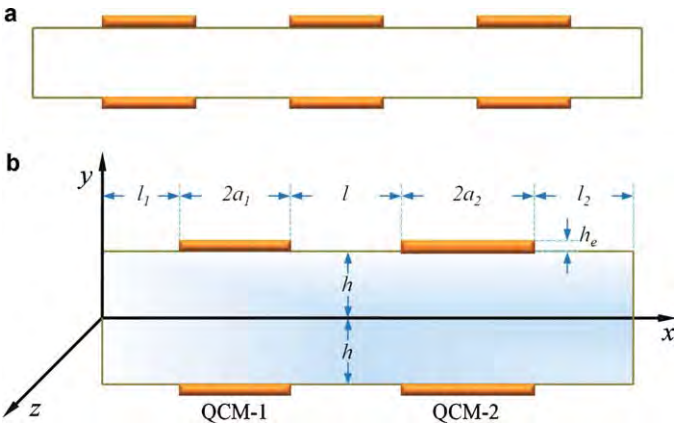

Fig. 1. Conventional MQCM (a) structure and (b) 2D model with generalized pair of QCMs [37].

on both sides as illustrated in Fig. 1(a). The size of electrode pairs and the spacing between them depend on the number and density of QCM in the array. In a MQCM system, acoustic wave induced by one QCM will propagate laterally through the substrate over a specific distance and if another QCM is located within vicinity of the acoustic field, acoustic interference will occur [40]. For a small MQCM array, spacing between adjacent QCMs may be sufficiently large and conventional MQCM structure can function properly since interference is negligible. For a large MQCM array, distance between adjacent QCMs must be small due to space limitation and hence strong acoustic interference is inevitable. The interference generally causes fundamental resonance frequency changes to all acoustically coupled QCMs and spurious frequency shifts due to mass or stress loading on neighboring QCMs. The problem becomes particularly serious when all QCMs are identical and operate at the same resonance frequency [37].

Acoustic interference in MQCM is highly complicated due to convolution of the simultaneous vibration motions from several resonators on one quartz plate. Additionally, it depends on several parameters of MQCM device including spacing between adjacent electrodes, geometry, dimensions and thickness of each electrode, mechanical and piezoelectric properties of quartz substrate and mechanical properties of electrode materials. Consequently, analysis of MQCM and its interference characteristics are mainly experimentally studied. Typically, interference between two adjacent QCMs is examined experimentally by impedance measurement of the two QCMs under exchanged external load and an electrical equivalent circuit is used to model and describes the response [36]. Electrical equivalent circuits including Butterworth–Van-Dyke (BVD) model [41] and transmission line representation [42] have been effectively used for QCM measurement analysis. Interference is introduced in a BVD circuit model by a complex coupling resistance between two BVD branches. In an equivalent circuit model, MQCM configuration is simplified into one-dimensional structure and the vibration profile is assumed to be uniform throughout the electrode surface. The results evaluated from these models are mainly valid in the region near the resonance frequency, which is calculated by applying Kirchhoff's law. Electrical circuit modeling can provide good estimation and prediction for experimental observation. However, it cannot give physical understanding and correlation between interference behaviors and physical parameters because it neglects some mechanical important features including modes coupling and energy trapping of electrode layer [40].

Theoretical modeling can provide insight understanding of interference mechanisms as well as relationship between interference behaviors and physical parameters. In general, theoretical analyses are performed on simplified models of complex real world problems so that analytical or semi-analytical solutions can be obtained. Recently, the theoretical analysis on interference of MQCM has been conducted using a simplified MQCM model with two generalized QCMs on a monolithic quartz crystal plate as illustrated in Fig. 1(b) [37]. This simple model is chosen to represent two nearest-neighbor QCMs in a monolithic MQCM array. Two quartz crystal microbalances, QCM-1 and QCM-2, are formed on an infinitely wide quartz plate ($l_1 = l_2 = \infty$) with a thickness of $2h$ and electrode widths of $2a_1$ and $2a_2$, respectively. The thickness of the electrode and separation between two QCMs are h_e and l, respectively. The analysis is based on one-dimensional modified Mindlin's theory with piezoelectric effect, which comprises a set of partial differential equations [43]. The effects of electrode sizes, spacing between two QCMs and QCM position on interference characteristics are extracted from the theoretical solutions.

The interference has been quantitatively characterized in terms of frequency interference (FI) and mass induce shift (MIS). FI is defined as the normalized frequency change $(\Delta\omega/\omega)_f$ of one QCM due to a mass loading on another while MIS $(\Delta\omega/\omega)_m$ is the normalized change in resonance frequency due to the adsorption of mass on its own electrode. MIS can be significantly modified due to the presence of neighboring devices in MQCM. FI and MIS are mathematically the same but they arise from different physical mechanisms. From the theoretical analysis, two parameters including relative width between two QCMs (a_2/a_1) and separation relative to QCM thickness (l/h) at a fixed QCM width relative to QCM thickness (a_1/h) are the most important factors that affect the FI and MSI.

FI is calculated from the resonance frequency shift of QCM-1 when the mass is placed on QCM-2. It is found from the simulation that FI has several peaks at different a_2/a_1 values. The largest FI for all a_1/h values occurs near $a_2/a_1 = 1$ where the two electrodes have the same width. This corresponds to the strongest fundamental acoustic coupling of QCMs operating at the same resonance frequency. At higher values of a_2/a_1, FI peaks for various QCM widths (a_1/h) appear at different c/a values. These peaks is attributed to anharmonic overtones excited from QCM-2 and coupled into QCM-1. The overtone coupling peaks $(a_2/a_1 > 1)$ periodically occurs at a_2/a_1 periods of ~1.7, 1.34 and 1.14 for $a_1/h = 10$, 20, and 40, respectively. Thus, strong interference occurs over a broader range of a_2/a_1 for smaller electrodes. On the other hand, anharmonic interference amplitudes of smaller electrodes are slightly lower than larger ones. Consideration of MIS offers an alternative perspective of interference. MIS is calculated from the resonance frequency shift of QCM-1 when the mass is placed on QCM-1 itself. It is seen from simulation that MIS decreases loaded frequency shifts by a factor of ~0.5 for both fundamental and anharmonic interference peaks. Thus, the mass sensitivity of QCM-1 is considerably reduced due to acoustic interference from QCM-2. In addition, MIS is found to slowly increase as electrode width (a_1/h) increases.

For the effect of separation, it is found that FI is high for small separations and then decreases rapidly with increasing separation as expected. In addition, FI for smaller electrodes is considerably higher than that for larger one and thus smaller electrodes require larger relative spacing. In contrary, MIS decreases slightly for small separations $(l/h < 5)$ and it is not strongly dependant on the separation for $a_2/a_1 = 0.5$. More recently, similar theoretical analysis on a more general MQCM model with an arbitrary number of QCMs on a monolithic quartz crystal plate is reported [44]. However, the analysis is limited to a special condition that all QCMs have the same electrode width and inter-electrode spacing and only the influences of the width and spacing on interference are evaluated. Some conclusions can be drawn from the theoretical analyses. Firstly, the microbalance channels of the devices may be designed to have different electrode sizes to avoid strong frequency interference.

Secondly, a large electrode size is helpful for acoustic energy trapping. However, the large size of electrode may also bring higher order modes and introduce higher order frequency interference. In applications, the size of electrode may be restricted by the number of channels mounted on quartz plate. Lastly, the separations need to be large to avoid strong frequency interference when all channels have the same size and same resonance frequency.

The theoretical calculation can provide insightful understanding of interference effects for MQCM and can be used to guide MQCM design. However, it cannot provide accurate prediction for real world 3D MQCM structures as 3D geometries such as edge effects of electrode layers and crystallographic orientation of electrode relative to quartz substrate cannot be directly included in the analysis. 3D simulation is thus required for more accurate design and analysis of MQCM devices. Recently, 3D simulation of a MQCM model with two symmetric QCMs on a monolithic quartz crystal plate has been reported [40]. The simulation is conducted using finite element analysis (FEA) method with the commercial software package, ANSYS. The ANSYS package provides electromechanical coupled field element, which includes piezoelectric effect. The full piezoelectric tensor formulation included in the package can account for anisotropic behaviors of piezoelectric crystals. 3D FEA simulation can thus provide considerably more quantitative information than 1D theoretical modeling. In addition to frequency interference, self-mass sensitivity and mutual-mass sensitivity, vibration mode shape and crystallographic orientation of an electrode pair can be obtained from 3D simulation results.

For example, 3D simulation reveals the phenomenon of resonance splitting into parallel and anti-parallel mode for a QCM pair when two identical QCMs operate at almost the same resonance frequency. In the 3D simulation model, the thickness of both gold electrodes and spacing between them are 6 mm, 100 nm and 3 mm, respectively. The parallel resonance (with f_1 = 4954960.1 Hz) results in the shear displacement overlapping of two QCMs, while antiparallel resonance (with f_2 = 49571192.6 Hz) causes the two QCMs to have opposite displacements. The displacement overlap in parallel resonance mode significantly induces acoustic coupling between two channels. With mass deposited on one QCM surface, both parallel and anti-parallel resonance frequencies decrease. Moreover, it is found that the parallel resonance frequency shift is linearly proportional to the mass absorbed while the anti-parallel resonance frequency shift non-linearly decreases and the sensitivity of the frequency shift for anti-parallel resonance decreases as the mass absorption per unit area increases. This results from the fact that the mass absorbed on one QCM results in asymmetrical detuning the two resonators and hence the splitting between the parallel and anti-parallel resonance frequencies increases.

Moreover, 3D simulation can provide the effect of anisotropic piezoelectric property of AT-cut quartz plate in x–z plane on interference. The coupling between a QCM pair is not the same for different angle θ to the x-direction as schematically shown in Fig. 2 because acoustic waves propagate with different velocities in different directions within the crystal plate. In this analysis, the interference is evaluated in term of mass–frequency influence coupling factor, which is defined by:

$$\alpha_{\mathrm{i}} = \frac{\psi_{\mathrm{i-j}}}{\psi_{\mathrm{i-i}}} \tag{5}$$

$$\psi_{\mathrm{i-j}} = \frac{\Delta f_{\mathrm{i}}}{\Delta m_{\mathrm{j}}} \tag{6}$$

where i and j are the labels of two QCMs, Δm_{j} is the mass per unit area added on the surface of QCM-j and Δf_{i} is the frequency shift of QCM-i. It is found from the analysis that the coupling strength is lowest when QCM pair (pair C_1–C_2 in Fig. 3) located in z-direction (θ = 90°) and the dependency on θ has two fold symmetry around x

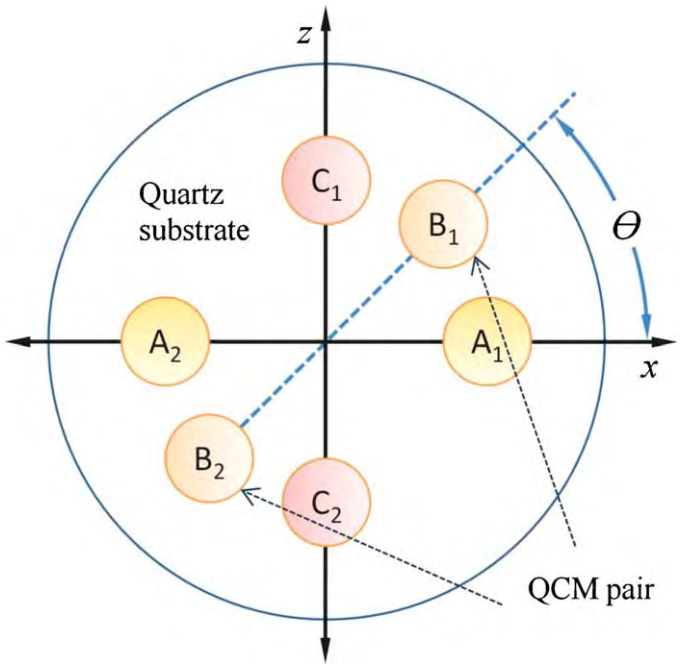

Fig. 2. Typical arrangements of QCM pairs in crystallographic z–x plane [40].

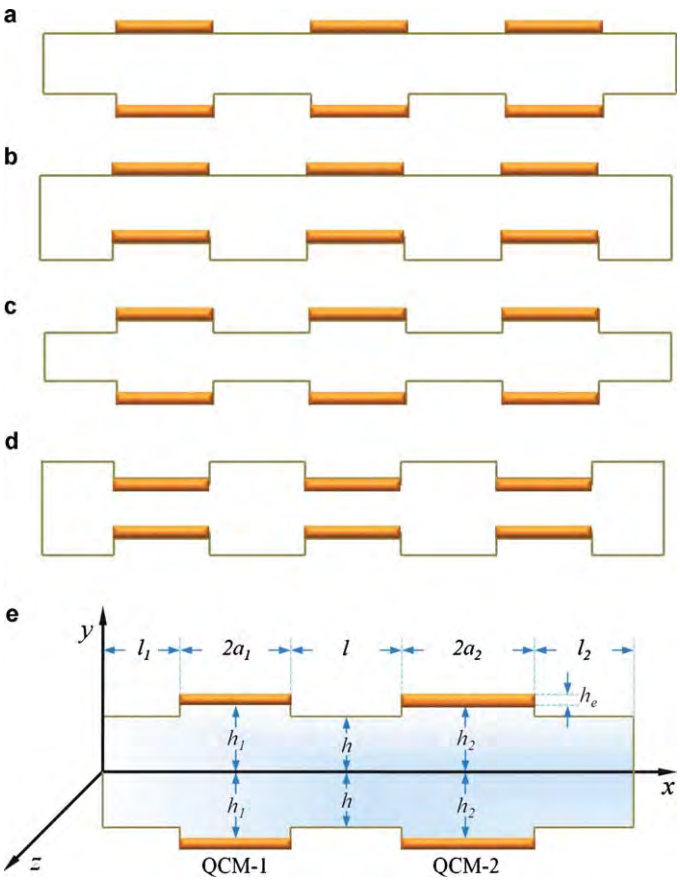

Fig. 3. Various mesa-shaped MQCM structures: (a) plano-mesa (b) plano-inverted-mesa (c) bi-mesa and (d) bi-inverted-mesa (e) 2D model with generalized pair of bi-mesa shaped QCMs [57].

and z axes. In addition, it is found that the frequency split between parallel and anti-parallel of QCM pair decreases as θ increases from 0° to 90°. The results indicate that the thickness shearing deformation transferred in x-direction of quartz crystal is more than that in z-direction. Therefore, QCM pair will be matched when their locations in x–z plane are at the same angle or 180° apart. This consideration should be taken into account in MQCM design. Interference among QCMs in conventional MQCM may be alternatively avoided by mean of successive oscillation or multiplexing. In this case, only one or a few QCMs can resonate at a time so that interference can completely be eliminated. This scheme is limited to applications, which do not require real-time or high speed measurement.

In addition to acoustic interference, other problems of conventional MQCM include spurious vibration, limited sensitivity and limited size of QCM electrodes. Spurious vibration occurs due to coupling between thickness shear (TS) and other modes including thickness flexural (TF), face shear (FS), thickness twist (TT) and higher order modes. The coupling between TS and TF occurs due to crystal edge effect and it is strong because both modes have a similar displacement field [45]. The coupling between TS and FS or TS and TT is relatively weak. In addition, the shear rotation about the z-axis is more than an order of magnitude less than the shear rotation about the x-axis or deflection in the y-direction [46].

Other important problems of MQCM are the limitation of sensitivity and electrode size. The mass sensitivity and diameter of MQCM electrode are both limited by the thickness of the crystal. The sensitivity is proportional to the square of resonance frequency, which is inversely proportional to quartz thickness. The thickness of quartz crystal is limited to around 100 μm because thinner quartz plates are too fragile and cannot be practically processed. The thickness constraint also limits diameter of electrode because small-diameter electrode QCM does not resonate or resonates with a very low Q factor if the diameter of the electrode to thickness of the crystal ratio is below 5 [47]. This limits miniaturization of conventional MQCM devices.

3. MQCM based on modified quartz substrate structure

Several methods have been developed to eliminate or minimize interference and other problems of conventional MQCM. Modification of quartz substrate structure is found to be the most effective approach to solve the problems. In this section, various MQCM schemes based on modification of quartz substrate structure will be described.

3.1. MQCMs with mesa shape designs

The most basic concept for minimizing the coupling of acoustic energy between adjacent QCMs is to increase the difference of the resonance frequencies between the electrodes and inter-electrode portions of the quartz plate. A direct way to increase the resonance frequency difference is to vary the quartz thickness between the electrode and inter-electrode regions. This can practically be done by means of standard micromachining process. The structure with varying quartz thickness in steps are commonly termed, *Mesa*, which can be subdivided into plano-mesa [48,49], plano-inverted-mesa [50,51], bi-mesa [48,49,52] and bi-inverted-mesa [53] as defined in Fig. 3. For plano-mesa structure (Fig. 3(a)), square cavity with reduced quartz thickness is formed in the inter-electrode regions while the other side is still planar. On the other hand, square trenches are created in the electrode regions for plano-inverted-mesa structure (Fig. 3(b)). For bi-mesa and bi-inverted-mesa structures (Fig. 3(c–d)), square cavities are made symmetrically on both sides.

The interference and acoustic energy trapping behaviors of the quartz mesa structure of different designs have been experimentally demonstrated [49,54]. It has been shown that the acoustic energy of the thickness shear mode of mesa-shaped MQCMs is considerably better confined within electrode regions than that of conventional MQCM and the separation between two adjacent resonators can substantially be reduced using mesa-type MQCM. With inverted-type-mesa designs, QCM resonators can operate at higher resonance frequency than those of non-inverted designs because the quartz plate thickness in the electrode area is decreased [51,53,55,56]. This scheme can thus solve the limitation of mass sensitivity of conventional MQCMs. Comparing between bi-mesa and plano-mesa schemes, QCMs with bi-mesa designs exhibit better resonance characteristics with lower spurious vibration mode and higher Q-factor than plano-mesa configuration because of the symmetric structure [48]. However, plano-mesa scheme are more practical than bi-mesa structure because fabrication process is considerably simpler and its top planar surface is more suitable for most applications than step-profile surface [38]. Therefore, plano-inverted-mesa structure has become more commonly used in MQCM devices.

Recently, bi-mesa MQCM has been theoretically analyzed [57,58] based on two-dimensional modified Mindlin's theory, which has also been used for analysis of conventional MQCMs. Two generalized mesa-shaped QCMs on a monolithic quartz crystal plate as illustrated in Fig. 3(e) are used as model to represent two adjacent QCMs in MQCM structures. Two quartz crystal microbalances, QCM-1 and QCM-2, are formed on surfaces of two mesas with quartz thickness of $2h_1$ and $2h_2$, mesa widths of $2a_1$ and $2a_2$, and distances to edges of l_1 and l_2, respectively. The thickness of the electrode, quartz thickness outside electrode regions and separation between mesas are h_e, $2h$ and l, respectively. In this analysis, the Mindlin's equations for the coupled vibrations of TS and TF modes are used and piezoelectric effect is neglected. The kinetic and potential energies per cycle in the different portions of the mesa structure are computed. The kinetic energy consists of deflective and rotational kinetic energies while the potential energy contains rotational and extensional potential energies.

The interference behaviors of mesa shaped MQCM are evaluated in terms of frequency interference (FI) described in the previous section and normalized energy-trapped of QCM-1, which is defined as the ratio of energy trapped within QCM-1 section to the total energy in the quartz plate. The effects of mesa height, electrode sizes, spacing between two QCMs and QCM position on interference behaviors are acquired from the theoretical calculation. The heights of the two mesas, h_1 and h_2, are both equal to h_m. It is shown that FI decreases monotonically with increasing mesa height for the infinite plate case. When the plate has a finite length, FI graph still follows the same curve but periodical spikes occur. These spiking peaks correspond the coupling of TF and TS modes due to the existence of boundaries. It is found that a small relative mesa height ($h_m/h > 1.03$) can effectively reduce frequency interference between two adjacent QCMs. Thus, only small etching depth is needed to form mesa structure with low interference and this can considerably simplify mesa-MQCM fabrication process. However, strong coupling regions due to the presence of a boundary still exist for mesa structure with specific relative heights and thus they must be avoided in the mesa-MQCM design.

In this analysis, the energy trapped in QCM structure has been considered with different MQCM parameters. The energy trapped in QCM-1 is determined when only QCM-1 is under excitation. For mesa-MQCM with above parameters, energy trapped in QCM-1 is found to increase as relative mesa height increases and negative peaks, where the trapped energy decreases markedly, also appear at the same relative mesa height as those of FI. At these peaks, nearly half of the energy is found to escape to other parts of the plate in

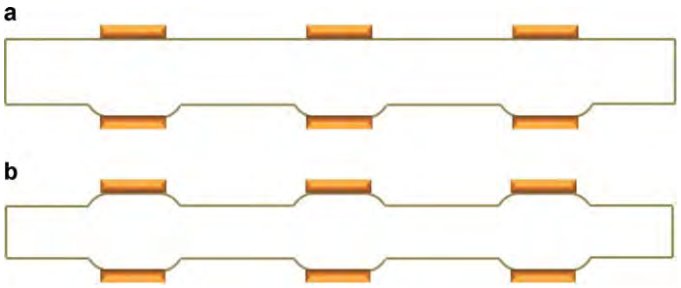

Fig. 4. Various convex-shaped MQCM structures: (a) plano-convex and (b) bi-convex.

the form of a flexural wave [58]. The effect of the relative electrode width (a_2/a_1) on energy trapped in QCM-1 for mesa and no mesa structures is also analyzed. It is shown that only small relative mesa height of 1.02 can considerably increase energy trapped in QCM-1 except the regions near the peaks of fundamental ($a_2/a_1 = 1$) and anharmonic coupling ($a_2/a_1 > 1$). At the peaks of coupling regions, the maximum loss from QCM-1 can be half of the total acoustic energy and most of the escaping energy is trapped in QCM-2. The main benefits of the mesa structure are to narrow the range of strong coupling region and reduce interference outside these regions. These give considerable flexibility for the design of MQCM devices.

3.2. MQCMs with convex shape designs

Mesa design can offer considerable improved MQCM performance in terms of interference reduction and sensitivity enhancement. However, the straight edge mesa structure cannot effectively correct mode coupling problems between the fundamental TS and spurious modes [54]. As discussed in the previous section, the coupling between TS and TF modes remains quite substantial in mesa-shaped MQCM. The coupling is undesirable because energy is taken from the usable frequency vibration, resulting in damping and lower *Q*-factor. High *Q*-factor is important for ultra sensitive detection in liquid mode. Several structures including dual-step mesa [54], multi-step mesa [59] and spherical convex [47,60–62] have been developed to reduce mode coupling problems so that oscillation energy is better trapped at the center and very little dissipation occurs at edges. Among these, the spherical convex-shape structure can theoretically separate vibrating modes most effectively. Spherical convex-shaped MQCMs, which include plano-convex [60] and bi-convex [47,61] designs as illustrated in Fig. 4, have been reported.

Some sophisticated processes have been developed to realize convex-shaped 3D QCM structures. Firstly, planoconvex quartz-crystal unit is fabricated based on a laborious mechanical polishing method [60]. Recently, the miniaturized beveled bi-convex QCM has been developed by photoresist thermal melting [61] and photoresist reflow with solvent vapor process [47]. The later process is particularly promising because diameter, curvature and height of spherical convex shape can be well controlled with moderate cost and reproducibility. In this process, spherical shaped photoresist on quartz substrate is formed after photolithographic patterning and reflow in a suitable organic solvent. Reactive ion etching in SF_6/Xe gas mixture [61] is then used to transfer spherical structure into quartz-crystal substrate. Spherical bi-convex MQCM structures with diameter ranging from 100 μm to 2 mm and height from 1 to 7 μm have been realized and the resonant characteristics have been studied.

It has been demonstrated that the spherical bi-convex QCM exhibits very sharp resonant peak with negligible spurious vibrating modes while the planar QCM resonates with numerous spurious vibration [47]. The spherical convex-shape can effectively decouple the vibrating modes in QCM. An optimum *Q*-factor of ~80000, which is twice higher than that of the 100 μm-thick planar QCM, is obtained from the spherical convex shape with diameter and height of 2 mm and 1.7 μm, respectively. The spherical bi-convex and planar QCM are also studied in viscoelastic liquid using glycerol/water mixtures contacted on one side of QCM. It is shown that the effective loading range of the spherical bi-convex QCM is considerably larger than that of the planar QCM. The effective loading range in liquid is defined as the range in which the resonance frequency shift is linearly proportional to $(\rho\eta)^{1/2}$ where ρ and η are liquid density and viscosity, respectively. In addition, the maximum viscosity in the effective region for the spherical biconvex QCM is found to be approximately five times greater than that for the planar QCM.

3.3. MQCMs with x-axis inversion

x-Axis inversion [63–65] is a useful method that can increase the difference of the resonance frequencies between the electrode and inter-electrode portions of the quartz plate. An advantage of this technique is that it does not require physical removal of quartz material from the plate. It is the phenomenon that *x* crystallographic axis of quartz crystal is locally rotated by 180° under a specific thermal treatment as illustrated in Fig. 5(a). In the treatment process, an AT-cut plate is coated with a thin Cr or NiCr film on a desired pattern and then heated at 520–560 °C in a vacuum. *x*-Axis inversion would occur only in the area under the metal film because of mechanical stress induced by thermal expansion difference between the quartz plate and the film. In the inversion area, the *y*-axis is also inverted and the cut angle changes from $+\theta$ to $-\theta$ AT-cut. Alternatively, *x*-axis inversion can be formed by applying heating current to the metal film [63]. In this case, heat is more concentrated on the patterned metal film and *x*-inversion can occur at a relatively low temperature of 480–500 °C with DC current density of 13.3–16.7 mA mm^{-2}. This method is advantageous due to relatively low process temperature but it requires additional electrical connection, which can be cumbersome for complex patterns. Lastly, laser has been applied to selectively induce *x*-axis inversion in the metal film [65]. The advantages of this method are that it requires lower substrate temperature of 400–480 °C and *x*-axis inversion area can be defined with higher lateral resolution, allowing narrower *x*-axis inversion region and hence higher MQCM density.

x-Axis inverted area exhibits different dispersion characteristics of the elastic wave propagation from non-inverted one. It is found that the cut-off frequency of the *x*-axis inverted area is higher than that of the non-inverted area by a factor of 1.47. As a result, plate wave excited at the electrode area is highly attenuated as it propagates into the *x*-axis inverted area. The attenuation of the wave in the *x*-axis inversion area is proportional to the ratio of *W* and *H*, where *W* is the width of the *x*-axis inversion area and *H* is the plate thickness. From theoretical calculation, attenuation is estimated to be more than 70 dB for $W/H = 3$. Thus, adjacent resonators can be effectively mechanically isolated by an interposed x-axis inverted region and *x*-axis inversion is promising for acoustic decoupling in MQCM device.

MQCM structure with *x*-axis inversion has been proposed as illustrated in Fig. 5(b) [63]. In the structure, *x*-axis inversion areas are formed in the space between adjacent QCM electrodes. *x*-Axis inversion area is created by Cr film deposition and the thermal treatment. Quartz surface is then lightly etched by buffered oxide etching solution and Cr film is etched away, leaving the pattern of *x*-axis inverted regions on substrate. Finally, QCM electrode film is deposited by sputtering or evaporation and pattern of electrode array is aligned to the *x*-axis inverted pattern by standard photolithography. The acoustic decoupling between two adjacent

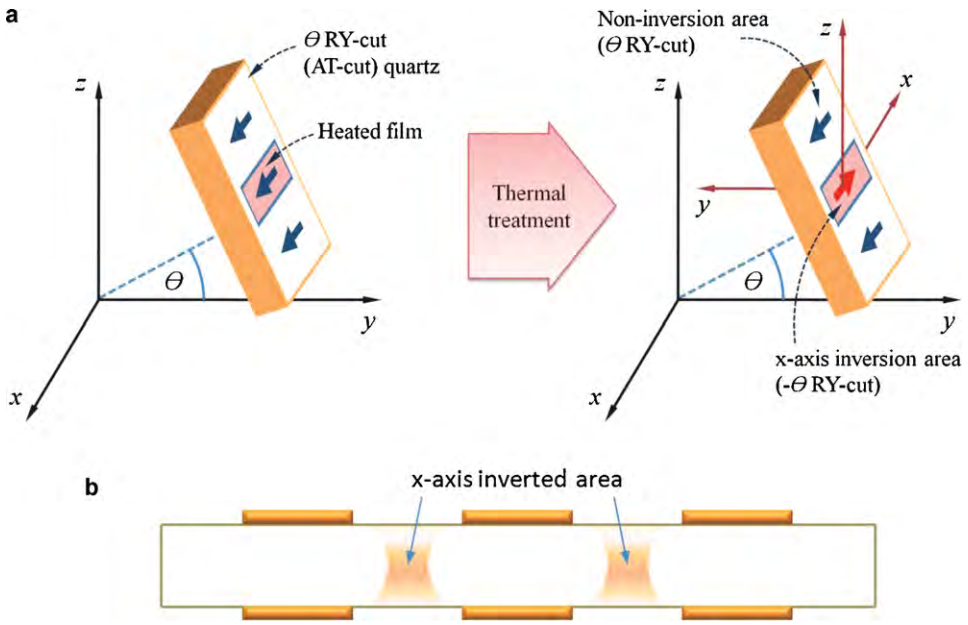

Fig. 5. *x*-Axis inversion: (a) schematic of inversion process [63] and (b) *x*-axis inverted MQCM structure [35].

QCMs separated by *x*-axis inversion region has been experimentally demonstrated by mean of two-port network measurement. In the measurement, ac input is applied to the first QCM at port 1 while both electrodes of the second QCM at port 2 are either open or short and impedance–frequency response of the first QCM is measured. For a conventional MQCM, one resonant peak occurs when port 2 is open while two resonant peaks appear at different frequencies when port 2 is short. This indicates the mechanical coupling between two resonators under the short circuit condition. On the other hand, the frequency response of the first QCM is not affected by the termination of the second QCM of MQCM with *x*-axis inversion, demonstrating that both resonators are effectively isolated by the *x*-axis inversion area.

Table 1 summarizes advantages, disadvantages and available reported references and parameters [7,36,38,39,47,62,65–82] of all MQCM structures discussed in the preceding sections. It is evident that the common advantage of all MQCM structures with modified quartz substrate is low interference that allows large array size and high array density. In addition, inverted-mesa structures offer specific advantages of higher resonance frequency and mass sensitivity because of reduced thickness of active quartz layer while convex and bi structures can reduce TS–TF and TS–extension mode couplings, respectively. However, MQCM structures with modified quartz substrate are still not widely employed because they involve difficult fabrication processes including deep etching, thermal treatment and aligned electrode patterning. In particular, all bi structures have rarely been reported because of very intricate two-side processing and incompatibility with flow injection system. Among MQCM with modified quartz substrate, plano-inverted-mesa has been the most frequently reported structure because it simultaneously offers low interference, high resonance frequency, high mass sensitivity and compatibility with flow injection system while its fabrication is not more difficult than those of others in its category and its frequency mode coupling can be minimized by employing suitable design.

4. MQCM sensing platforms

An array of QCMs may be formed differently into a variety of MQCM sensing platforms for various types of sensing or measurement applications. In this section, potential MQCM sensing platforms will be explained [38].

4.1. MQCM as a static multichannel detector

In this platform, identical QCMs in an array are coated with different sensing layers or receptors and MQCM is set in a simple sample cell as illustrated in Fig. 6. Additionally, one channel of MQCM should be used as a reference, which has no receptor, to compensate for the influences of the temperature, viscosity, and density of medium. In these cases, simple measurements with one drop of an electrolyte solution without an electrolytic cell are also possible [38]. Different receptors will accept additional mass from target species by means of binding, adsorption or deposition causing resonance frequencies of underlying QCMs to change accordingly.

The main class of applications for this platform is multi-component analysis, which is used to identify a multi-component mixture and/or its ingredients with respective concentrations. There are three main schemes for multi-component analysis. Firstly, QCMs are bound with different receptors, which are selective to individual component in the target mixture. The resonance frequency shift of QCM coated with each receptor can be used to directly identify the presence of each component and determine its concentration. The scheme can work only when receptors with very high specificity to target species are available. Existing receptors with such a specific property include complementary DNAs and antigen/antibody [5,27,83]. Thus, this technique can only be applied to some specific biosensing while it cannot generally be implemented for chemical and gas sensing.

The second scheme employs a group of different receptors on QCMs that have low selectivity towards a set of components in the mixture. When receptors are exposed to target components, they respond differently according their selectivity, producing resonance frequency shifts to related QCMs. The presence and concentrations of all target components are then determined from recognized relationships of selectivity parameters of all components. The number of different receptors should be the same as the number of components to obtain unique deter-

Table 1
Summary of advantages, disadvantage and available reported parameters (up to September 2010) of MQCM structures.

MQCM structure		Advantages	Disadvantages	Available reported parameters (up to November 2010)		
				References	f_0 (MHz)	Array size
Conventional		Very simple and low cost fabrication process	Highly susceptible to interference	Interference characteristic of two channel MQCM [36]	5	2
			Limited resonance frequency, array size and density, mass sensitivity	MQCM for ammonia and humidity sensing [66]	10	6
			Strong frequency mode couplings	MQCM coated with silica hybrid films for gas sensing application [67]	5,6	4
				Comparative study between QCM and MQCM in humidity sensing application [68]	10	4
				MQCM with multiplexed oscillator for VOC sensing [69]	10	4
				Analysis of MQCM with circular flow chamber [70]	5	4
				MQCM coated with ionic liquids films and conductive polymer for VOCs detection [71]	10	4
				MQCM coated with MIP for detection of yeast cells in liquid [72]	10	4
				ACR type MQCM for immunoglobin detection [73]	17	2
				MQCM for sensing terpenes in fresh and dried herbs [74]	10	6 (3 × 2)
Mesa	Plano-mesa	Low interference	Required difficult deep etching process	n/a	n/a	n/a
		Large array size and density	Limited resonance frequency, mass sensitivity, electrode size			
			Some remaining frequency mode coupling particularly TS–TF and TS–extension			
	Plano-inverted-mesa	Low interference	Required difficult deep etching process	Multi-frequency MQCM for toluene detection [7]	20–50	16
		High resonance frequency, array density, mass sensitivity	Some remaining frequency mode coupling particularly TS–TF and TS–extension	MQCM possibility to 2D mass mapping [38]	10	4
				Multi-frequency MQCM for VOC sensing [75]	20	6
				MQCM coated with SW-CNT for gas detection [76]	n/a	9
				MQCM coated with SAM for HAS detection [77]	27	9
				MQCM functionalized for avidine and BSA detection [79]	62	9
	Bi-mesa	Low interference	Required difficult two-side deep etching and intricate two-side processing	n/a	n/a	n/a
		Low TS-Extension coupling	Unsuitable for some platforms including flow injection system			
		Large array size and density	Some remaining frequency mode coupling particularly TS-TF			
	Bi-inverted-mesa	Low interference	Required difficult two-side deep etching and intricate two-side processing	High frequency inverted mesa MQCM structure [39,80]	20–94	n/a
		Low TS–extension coupling	Unsuitable for some platforms including flow injection system			
		High resonance frequency, array size and density, mass sensitivity	Some remaining frequency mode coupling particularly TS–TF			

Table 1 (*Continued*)

MQCM structure		Advantages	Disadvantages	Available reported parameters (up to November 2010)		
				References	f_0 (MHz)	Array size
Convex	Plano-convex	Low interference	Required sophisticated patterning and difficult deep etching process	ACR type MQCM for photocatalytic measurement [81]	17	2
		Very Low mode couplings except TS–extension	Limited resonance frequency, mass sensitivity and electrode size			
		Large array size and density	Remaining TS- extension mode coupling			
	Bi-convex	Low interference	Required sophisticated patterning, difficult deep etching process and intricate two-side processing	Fabrication of high Q biconvex MQCM [47]	16	2
		Very Low mode couplings	Unsuitable for some platforms including flow injection system			
		Large array size and density	Limited resonance frequency, mass sensitivity and electrode size			
x-Axis inversion		Low interference	Limited resonance frequency, mass sensitivity and electrode size	Fabrication of *x*-axis inversion by laser process [65]	5	2–6
		Large array size and density No mechanical etching process	Required sophisticated thermal treatment process	LFE type MQCM with *x*-axis inversion [82]	5	2

mination. Examples of receptors in this system are ligands for metal ions [84,85]. For instance, a QCM system with four different ligands having different affinity towards four metal ions can be used to determine the concentrations of the four metal ions [38].

Lastly, an array of different receptors having wide sensitivities towards various components is used to recognize the whole mixture. In this case, components in the mixture and their individual concentrations are not resolved. Most receptors found in nature fall within this category. These include gas-sensitive polymeric and organic materials, electrochemical electrode materials and biochemical enzymes. The QCM array with these receptors gives a pattern of resonance frequency shifts resulting from different receptors' sensitivities towards various ingredients in the composite, which can be analyzed based on pattern recognition methods. Commonly used pattern recognition methodologies are principal component analysis (PCA) [86–92], linear discriminant analysis (LDA) [87,93,94] and neural network [90–92,95]. The main applications for this scheme are odor sensor or electronic nose and taste sensor or electronic tongue.

4.2. Series MQCM as a multichannel detector in the flow injection analysis

A series of identical QCMs with different receptors can alternatively be applied to flow injection analysis for real-time detections as illustrated in Fig. 7. There are some important considerations when MQCM is operated in a flow injection system. Firstly, the structure of MQCM surface in contact with fluid flow should be planar and smooth so that the solution flow will not be disturbed. Thus, MQCM structures with non-smooth surfaces including bi-mesa, bi-inverted-mesa and bi-convex may not be suitable for flow injection analysis [38].

Secondly, analyte should be uniformly dispersed throughout the flow chamber so that all QCMs see the same sample concentration. The effect of flow chamber geometry and flow parameters on sample dispersion in flow injection system with integrated MQCM device has recently been studied by fluid dynamic simulations and flow injection experiments [70]. It has been demonstrated by simulation that MQCM with circular chamber design suffers from non-uniform sample distribution due to turbulent effect while such problem does not occur to MQCM chamber with rectangular design [96]. The results agree to experimental observation that there is a significant variation in resonance frequency shift responses of identical QCMs located in the circular chamber.

A flow injection system containing inverted-mesa MQCM in 20 mm × 20 mm × 0.7 mm square chamber has been demonstrated [7]. The influence of flow rate on uniformity of analyte distribution and the resonant characteristics of QCM is also studied. It is found that the flow rate considerably affects the resonant behaviors of QCM. In addition, spurious oscillation modes are found under low and high flow rate conditions and undesired oscillation can be minimized at an optimum flow rate of 500 $\mu L\,s^{-1}$. Thus, flow rate is another important parameter that must be optimized when MQCM operates in a flow injection system.

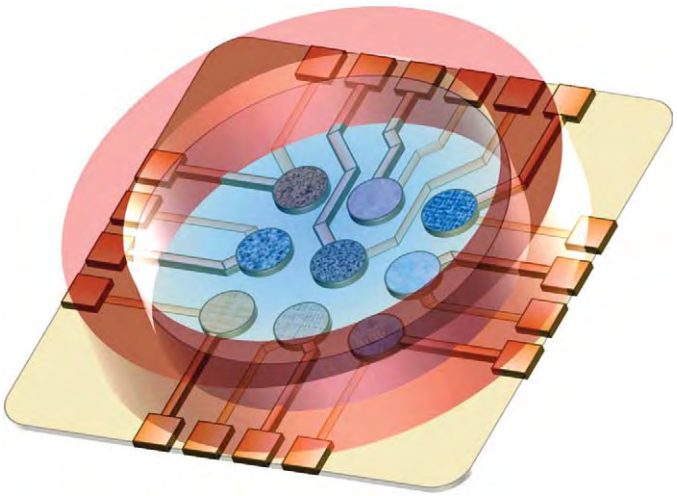

Fig. 6. MQCM platform: a static multichannel detector [38].

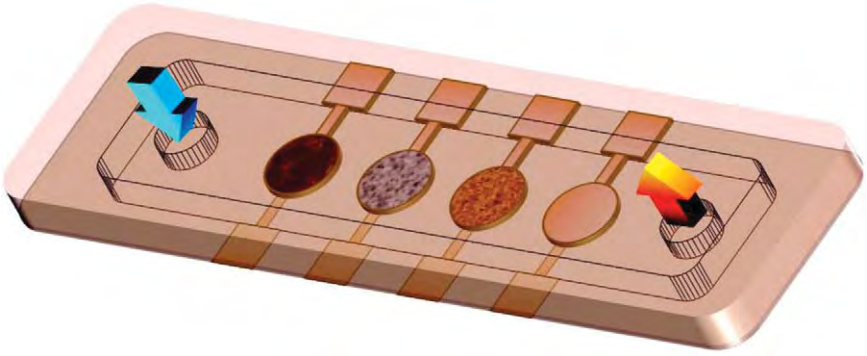

Fig. 7. MQCM platform: a series multichannel detector in flow injection analysis [38].

4.3. Multifrequency QCM as a multi-sensitivity and multi-dynamic range detector

Various QCMs in MQCM can be designed to operate at different resonance frequencies. This platform is termed *multi-frequency QCM* (*MF-QCM*). MF-QCM is typically based on inverted-mesa structures with different mesa thicknesses as illustrated in Fig. 8(a). This structure can be formed by standard mesa micromachining process with additional patterning and etching steps. By this scheme, resonance frequency, mass sensitivity and dynamic range of QCMs can be varied over a wide range of magnitude. A MF-QCM containing an array of 2 mm circular QCM diaphragms with different quartz thicknesses ranging from 77 to 81 μm and corresponding resonance frequencies ranging from 21.7 to 20.75 MHz has been demonstrated [75]. With decreasing quartz thickness, the resonance frequency and mass sensitivity simultaneously increases while the dynamic range decreases. Thus, MF-QCM can provide multi-sensitivity and multi-dynamic-range functionalities [7,38], which is highly valuable for general applications whose sample concentration and detection range are unknown. For multisensitivity and multidynamic range purpose, all QCMs may be modified by only one kind of receptor and the analyte can be detected with high sensitivity and wide dynamic range in one experiment if MF-QCM is properly designed. The multisensitivity and multidynamic range QCM is useful for a wide variety of applications including chemical sensing, bio-sensing and monitoring of surface processes including electrochemical reactions. Moreover, QCMs in an array may be modified with different receptors for multi-component analysis with multi-sensitivity and/or multi-dynamic range capability.

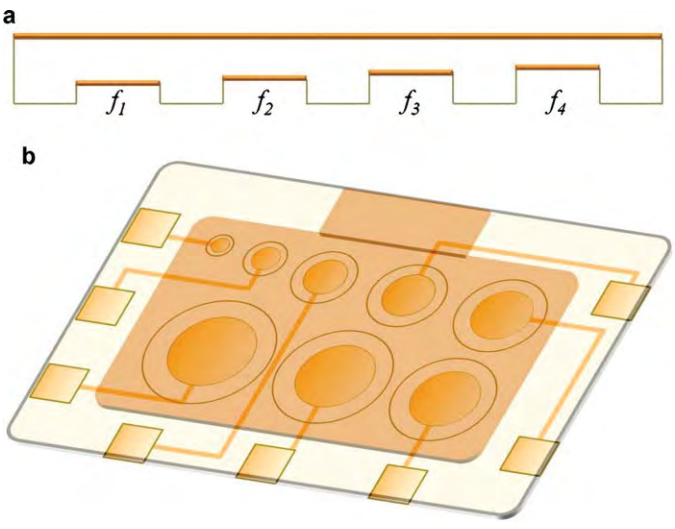

Fig. 8. MQCM platform: a multi sensitivity and dynamic range detector based on (a) varying quartz thickness and (b) varying electrode area [38].

In addition, MF-QCMs may be designed with different electrode sizes as shown in Fig. 8 (b) to further vary mass-sensitivity of QCM array. From Sauerbrey equation (Eq. (1)), the mass sensitivity ($\Delta F/\Delta M$) is inversely proportional to the electrode area (A) and hence mass sensitivity can be significantly increased by decreasing electrode area. Moreover, electrode size also causes small changes to resonance frequency and dynamic range, which cannot be seen from 1D theory. The dependence of resonance frequency on electrode size has been theoretically predicted from 3D finite element simulation [40]. From the simulation, it has been shown that the resonance frequency of QCM decreases as electrode size increases. In addition, the resonance frequency becomes less dependent on diameter for very large diameter values and it will eventually reach the frequency value of 1D theory given in Eq. (2), in which the electrode width is assumed to be infinite. Thus, the variation of electrode size can change the mass-sensitivity with small effects on other design parameters.

5. Potential and prospective applications for MQCM

The advancement of MQCM technology has enabled useful expansion of numerous sensing and measurement techniques based on QCM. Main advantages of MQCM in sensing fields include real-time multi-analyte label-free detection, multi-sensitivity-range sensing and environmental compensation capabilities. In addition, it is potential for real world applications because it can easily made portable. Nevertheless, its applications are still hindered by system/response complexity as well as high cost due to fabrication difficulty. This section presents potential and emerging MQCM applications, which comprise MQCM based gas sensor array as odor sensor or electronic nose, MQCM based chemical sensor array as electronic tongue, MQCM based biosensor array and other miscellaneous applications.

5.1. Odor sensor or electronic nose

Odor sensor or electronic nose is a device that can recognize several odors or gas mixtures. It typically consists of an array of gas sensors having different selectivities and the responses are analyzed by a suitable pattern recognition algorithm. When QCM is employed, gas sensor considerably differs from chemical and biosensors due to great differences of viscoelastic properties of sensing film and analyte. The characteristics of QCM based gas sensor are mainly determined by viscoelastic properties of sensing film while gas phase analyte only modifies the mass per unit area. Thus, QCM based gas sensor can easily be analyzed and developed. MQCM based odor sensor represents the first and the most